

Structural Alignment of Pseudocapacitive Materials Over Carbon Morphologies to Achieve Improved Capacitive Performance

Thesis Submitted to AcSIR
For the Award of the Degree of

DOCTOR OF PHILOSOPHY
IN
CHEMICAL SCIENCES



By
Mr. Roby Soni
Registration Number: 10CC14J26009

Under the guidance of
Dr. Sreekumar Kurungot

CSIR-National Chemical Laboratory, Pune-411008,
India

May 2018



सीएसआईआर - राष्ट्रीय रासायनिक प्रयोगशाला

(वैज्ञानिक तथा औद्योगिक अनुसंधान परिषद)

डॉ. होमी भाभा मार्ग, पुणे - 411 008, भारत

CSIR - NATIONAL CHEMICAL LABORATORY

(Council of Scientific & Industrial Research)

Dr. Homi Bhabha Road, Pune - 411 008, India



CERTIFICATE

24-5-2018

This is to certify that the work incorporated in the thesis entitled “**STRUCTURAL ALIGNMENT OF PSEUDOCAPACITIVE MATERIALS OVER CARBON MORPHOLOGIES TO ACHIEVE IMPROVED CAPACITIVE PERFORMANCE**” submitted by **Mr. Roby Soni** to the Academy of Scientific and Innovative Research (AcSIR) in fulfilment of the requirement for the award of the degree of *Doctor of Philosophy*, embodies the original research work carried out by him under my supervision at the Physical and Materials Chemistry Division, CSIR-National Chemical Laboratory, Pune-411008, India. I further certify that this work has not been submitted in part or full for the award of any degree or diploma. Research material obtained from other sources has been duly acknowledged in the thesis. Any text, illustration, table, etc. used in the thesis from other sources have been duly cited and acknowledged.


Roby Soni


(Student)



Dr. Sreekumar Kurungot

(Supervisor)

Communication Channels


NCL Level DID : 2590
NCL Board No. : +91-20-25902000
EPABX : +91-20-25893300
: +91-20-25893400

FAX

Director's Office : +91-20-25902601
COA's Office : +91-20-25902660
SPO's Office : +91-20-25902664

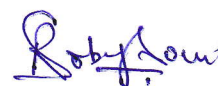
WEBSITE

www.ncl-india.org

DECLARATION

I, hereby declare that all the experiments in this thesis entitled “**STRUCTURAL ALIGNMENT OF PSEUDOCAPACITIVE MATERIALS OVER CARBON MORPHOLOGIES TO ACHIEVE IMPROVED CAPACITIVE PERFORMANCE**” submitted for the degree of Doctor of Philosophy in Chemical Sciences to the AcSIR-National Chemical Laboratory have been carried out by me at the Physical and Materials Chemistry Division, CSIR-National Chemical Laboratory, Pune-411008, India, under the supervision of Dr. Sreekumar Kurungot. The work is original and has not been submitted in part or full by me for any degree or diploma to this or any other University.

Date: 24-05-2018


Mr. Roby Soni

Physical and Materials Chemistry Division

CSIR-National Chemical Laboratory

Pune-411008, India

*Dedicated to
My Family*

&

*To Those Who Inspired this
Work*

Acknowledgement

At this juncture of my doctorate, I want to express my sincere gratitude to all the people involved directly or indirectly in the completion of my Ph.D. I shall try to put an honest effort to genuinely transform my feelings and thoughts into words about the people important to me. However, no word can suffice for the sincere gratitude that I feel for everyone mentioned in this document.

The foremost persons come to my mind while writing this acknowledgment are my parents. The energy and motivation that has led to all my achievements flow to me through my parents. There are no words that can explain how grateful I am to maa and papa for their hardships and toil which they have suffered to educate me. I owe everything to them. Maa and Papa, thank you very much for always supporting me and always standing by my side. Also, I want to thank my siblings Isha, Aman, Anamika and Raj for being such wondrous and encouraging brothers and sisters.

I express my deep and sincere gratitude to my thesis advisor, Dr. Sreekumar Kurungot; this thesis would not have been possible without his valuable guidance and inputs. I remember how, in the regular meetings for discussing Ph.D. discourse, he incessantly encouraged and motivated me to meet the timelines of projects. His positive criticism has immensely helped me to improve myself in the professional sphere. I thank him for providing all the essential research facilities which were necessary for my doctoral work.

I want to express my sincere gratitude to the former director of NCL, Dr. Sourav Pal, and current director, Professor Ashwini Kumar Nangia for providing the infrastructure and for resolving the fellowship related issues. I also want to thank Head of the Physical and Materials Chemistry Division, Dr. P. A. Joy, for the allowing me to avail the facilities of the department.

My Doctoral Advisory Committee members, Dr. Sayam Sengupta, Dr. Nandini Devi, Dr. Paresh Dhepe and Dr. Mahesh Kulkarni had extended their help and support through their valuable advice, suggestions, and criticism of my doctoral work. I thank and appreciate their effort and time devoted to the meetings and my thesis evaluation.

My senior, Dr. Bihag Anothumakkool needs a special mention. His mentorship at the beginning of my doctorate has indeed helped a great deal to complete my thesis. He was the person who taught me electrochemical characterization, device fabrication, and data analysis. I cherish our casual discussions about science, life, religion, etc. over a cup of coffee in the cafeteria and our weekend parties where we had a lot of fun and enjoyment. I thank Dr. Bihag for all of it.

I believe this is the appropriate occasion to show my gratefulness to my teachers, Dr. Ashok Kumar, Dr. Susan Vergheese, Dr. Hemant Kulshreshta, Dr. R.P. Singh, Dr. P.E. Joseph, Dr. Raju V. John, Dr. Anita A.K. Anand, Dr. Shalini Nelson and Dr. Anis of the School of Chemical Sciences, St. John's College Agra. I still remember them with awe for their continuous motivation, support, and encouragement during my graduate and post-graduate studies.

I thank and appreciate my seniors Dr. Sreekuttan Unni, Dr. Vishal Dhavale, Dr. Palaniselvam and Dr. Harshitha Barike for the supportive and friendly environment in the lab. My colleagues Pandiaraj, Varchaswal Kashyap, Siddheshwar N. Bhange, Rajith I.V., Vidyanad V., Pranav K.G., Nadeema Ayesha, Meena Ghosh, Narugopal Manna, Sachin Kumar, Dr. Gourav Singla, Dr. Raji V. and Dr. Debashree Das for their advice and support during my stay at NCL. Dr. Santosh Kumar, my colleague, and senior, needs a special mention; he was my roommate for first two years of my stay at NCL. He happily gave his help whenever I asked, both at the personal level and professional level. I appreciate the friendly and jovial environment extended to me by my dear lab mates. I especially want to extend my gratitude to Sidheshwar N. Bhange for his help and support; I remember us working together on my first doctoral assignment and coincidentally on the last project too. I shall cherish my relationship and friendship with all the above-mentioned people all my life. I would also like to mention Alka Raveendran, Athira, and Rashmi Chetry who carried out their internship under my guidance for their help in completing few of my projects. I also want to thank Apoorva for her help with many critical analyses. I also thank Sandeep Sharma and Dr. Asha for the collaboration.

During my stay at NCL, I, fortunately, met a few wonderful, cheerful and mirthfull people who also became my good friends. I thank Kuyil, Arun, Indrapal, Korra, Veer, Pravin, Poonam, Divya, Mukta, Umesh, Pankaj, Babasaheb, Ashwini, Chaitanya, Mohan and Sameer; all of them, extended their help and support whenever I was in difficulty. I especially want to thank Kuyil

for being such a wonderful and supportive friend, I shall always treasure our friendship. I appreciate their patronage. I especially want to thank Rahul, who was my roommate and we became very good friends in later years. I remember the fun we had during countless movies, trips and weekend parties. He is a profoundly humble and generous man. I feel fortunate to have a friend like him. I thank my friend Amarnath Singam and Surendra Verma (IIT-Bombay) for helping me out with a critical analysis.

I am grateful to Dr. C. P Vinod and Dr. Vaidhyanathan Ramanathan (IISER Pune) for giving their valuable time to evaluate my work during fellowship up gradations.

I am profoundly thankful to the Student Academic Office Staff; SAC chairman Dr. Mysore Shashidhar, former AcSIR chairman Dr. Chetan Gadgil, AcSIR chairman Dr. Mahesh J. Kulkarni, Ms. Purnima Kohle, Mr. P.V, Iyer, Ms. Komal, Ms. Vaishali and Ms. Harshita for the prompt processing of documents.

Though many are not mentioned, none is forgotten.

Roby Soni

List of Abbreviations

Abbreviation	Expansion
1D	One dimension
BET	Brunauer–Emmett–Teller
BP	Buckypaper
C_{dl}	Double layer Capacitance
CNH	Carbon Nanohorn
CNT	Carbon Nanotube
CP	Conducting Polymers
CV	Cyclic Voltammetry
DWCNT	Double Walled Carbon Nanotube
EDL	Electrical Double Layer
EDLC	Electrical Double Layer Capacitance
EDOT	3,4-Ethylene dioxythiophene
EIS	Electrochemical Impedance spectroscopy
ESR	Equivalent Series Resistance
FESEM	Field Emission Electron Microscope
fTP	Functionalized Toray-PANI
GCD	Galvanostatic Charge-Discharge
HOMO	Highest Occupied Molecular Orbital
IHP	Inner Helmholtz Plane
IPCC	Intergovernmental Panel on Climate Change
LSV	Linear Sweep Voltammetry

LUMO	Lowest Unoccupied Molecular Orbital
MWCNT	Multi-walled Carbon Nanotubes
OHP	Outer Helmholtz Plane
PAN	Poly acrylonitrile
PANI	Polyaniline
PEDOT	Poly(3,4-ethylene dioxythiophene)
pTP	Pristine Toray-PANI
PTFE	Polytetraflouroethylene
PVA	Polyvinyl alcohol
SEM	Scanning Electron Microscopy
SG	Scotch-Tape Grafoil Substrate
SSA	Specific Surface Area
SWCNT	Single-walled Carbon Nanotube
SWCNH	Single-walled Carbon Nanohorn
TEM	Transmission Electron Microscope
TGA	Thermogravimetric Analysis
TMO	Transition Metal Oxides
UPD	Under Potential Deposition
VGCF	Vapour Grown carbon Fiber
VGCNF	Vapour grown Carbon Nanofiber
XRD	X-ray Diffraction
XG	Xanthan Gum
Z_{Im}	Imaginary Impedance
Z_{Real}	Real Impedance

Table of Contents

Preface	1-4
Chapter 1	
Fundamentals of Electrochemical Capacitors and Importance of Structural Alignment of Pseudocapacitive Materials for High-Performance	5-44
1.1 Introduction	6
1.2 Fundamentals of Electrochemical Capacitors	8
1.2.1 Electrochemical Double Layer (EDL)	8
1.2.2 Different Models for Electrochemical Double Layer	9
1.2.2.1 Helmholtz Double Layer Model	9
1.2.2.2 Gouy-Chapman Model	9
1.2.2.3 Stern Model (Compact Diffuse-layer Model)	10
1.2.2.4 Triple-Layer Model (Esin and Markov, Grahame, and Devanathan Model)	12
1.2.2.5 Water dipole model (Bockris-Devanathan-Muller model)	13
1.2.3 Classification of Electrochemical Capacitors	14
1.2.3.1 Electrochemical Double Layer Capacitors	14
1.2.3.1.1 Mechanism of Charge Storage in EDLC	15
1.2.3.1.2 Materials Exhibiting Double Layer Capacitance	16
1.2.3.1.2.a Porous or Activated Carbon	16
1.2.3.1.2.b Carbon Nanotubes (CNTs)	17
1.2.3.1.2.c Graphene	19
1.2.3.1.2.d Carbon Nanofibers	20
1.2.3.1.2.e Carbon Nanohorns	21
1.2.3.2 Pseudocapacitors	22
1.2.3.2.1 Types of Pseudocapacitance	23
1.2.3.2.1.a Origin of Adsorption Pseudocapacitance	23
1.2.3.2.1.b Origin of redox and intercalation pseudocapacitance	24
1.2.3.2.2 Pseudocapacitive Materials	25
1.2.3.2.2.a Transition Metal Oxides (TMOs)	25
1.2.3.2.2.b Conducting Polymers	27
1.2.3.2.2.b.i Poly (3,4-ethylene dioxythiophene) (PEDOT)	28
1.2.3.2.2.b.ii Polyaniline (PANI)	29

1.2.3.2.3 Doping in Conducting Polymers	30
1.2.3.2.4 Issues of Low Capacitance and High Equivalent Series Resistance in Pseudocapacitive Materials	31
1.3 Composites of Pseudocapacitive Materials and Carbon Morphologies	33
1.4 Electrochemical Characterization Techniques and Calculations for Supercapacitors	34
1.4.1 Cyclic Voltammetry	34
1.4.2 Galvanostatic Charge-Discharge	35
1.4.3 Electrochemical Impedance Spectroscopy	36
1.4.4 Calculations	37
1.4.4.1 Weight of Material Deposited through Electrodeposition	37
1.4.4.2 Specific Capacitance	37
1.4.4.3 Volumetric Capacitance	38
1.4.4.4 Areal Capacitance	38
1.4.4.5 Volumetric Energy Density	38
1.4.4.6 Volumetric Power Density	38
1.4.4.7 Maximum Volumetric Power Density	37
1.4.4.8 Specific Energy Density	38
1.4.4.9 Specific Power Density	39
1.5 Scope and Objectives of the Current Thesis	39
1.6 References	41

Chapter 2

1D Alignment of PEDOT on CNTs through Interfacial Polymerization towards High Conductivity and Low Equivalent Series Resistance **45-62**

2.1 Introduction	46
2.2 Experimental Section	46
2.2.1 Materials	47
2.2.2 Functionalization of Carbon Nanotube (CNT)	47
2.2.3 Preparation of Buckypaper (BP)	47
2.2.4 Preparation of PEDOT Modified Buckypaper (PEDOT-BP)	48
2.2.5 Characterization	48

2.3 Result and Discussion	49
2.3.1 Interfacial Polymerization	49
2.3.2 SEM and TEM analysis	49
2.3.3 X-ray Diffraction Analysis	51
2.3.4 Surface Area Analysis	51
2.3.5 Elemental Mapping Analysis	52
2.3.6 Sheet Resistance and Flexibility Test	53
2.3.7 Electrochemical Characterization	55
2.3.7.1 Cyclic Voltammetry	55
2.3.7.2 Electrochemical Impedance Spectroscopy	56
2.3.7.3 Galvanostatic Charge-discharge	58
2.3.7.4 Performance Comparison of Interfacial and Non-interfacial Polymerized PEDOT	60
2.4 Conclusion	61
2.5 References	62

Chapter 3

Oxidant-Free Hydrothermal Synthesis of Ultrathin PEDOT over CNTs and Introduction of Xanthan Gum-Based Shear Thinning Gel electrolyte	63-82
3.1 Introduction	64
3.2 Experimental Section	65
3.2.1 Materials	65
3.2.2 Functionalization of Carbon Nanotubes	65
3.2.3 Synthesis of PEDOT of PEDOT-CNT Composite	65
3.2.4 Free-Standing Electrode Fabrication	66
3.2.5 Preparation of Xanthan Gum-H ₂ SO ₄ (XG-SA) Gel Electrolyte	66
3.2.6 Preparation of PVA-H ₂ SO ₄ Gel Electrolyte	66
3.2.7 Solid Supercapacitor Prototype fabrication	67
3.3 Result and Discussion	67
3.3.1 Infrared Spectroscopy	67
3.3.2 X-ray Diffraction Analysis	68
3.3.3 Thermogravimetric Analysis and Determination of PEDOT Loading	69
3.3.4 X-ray Photoelectron Spectroscopy	70

3.3.5 Electron Microscopy Analysis	71
3.3.6 Energy Dispersive X-ray Spectroscopy (EDS)	73
3.3.7 BET Analysis	73
3.4 Study of XG-H ₂ SO ₄ Gel Electrolyte	74
3.5 Electrochemical Characterization	75
3.5.1 Solid Supercapacitor Prototype Study	75
3.5.1.1 Impedance Study of XG-H ₂ SO ₄ Gel as the Electrolyte in Solid Supercapacitor	75
3.5.1.2 Cyclic Voltammetry	77
3.5.1.3 Electrochemical Impedance Spectroscopy	78
3.5.1.4 Galvanostatic Charge-discharge	79
3.5.1.5 Durability Test	80
3.6 Conclusion	81
3.7 References	81

Chapter 4

Enhancing the Electrochemical Surface Area through Induction of Superhydrophilicity and Structural Alignment in Polyaniline to Achieve High Capacitance **83-105**

4.1 Introduction	84
4.2 Experimental Section	85
4.2.1 Materials	85
4.2.2 Electrochemical Functionalization of Toray Carbon Paper	85
4.2.3 Electrodeposition of Polyaniline	85
4.2.4. Determination of Electrochemical Active Surface Area (ESA)	86
4.2.4.1 ESA Determination of pT and fT	86
4.2.4.2 Double Layer Capacitance (C _{dl}) Determination of pTP and fTP	87
4.2.5. Fabrication of Solid Supercapacitor Prototype	88
4.2.6 Characterization	88
4.3 Result and Discussion	89
4.3.1 Characterization of Functional Groups Incorporated after Anodization of Toray Carbon Paper	89
4.3.1.1 IR spectroscopy	89

4.3.1.2 XPS Spectroscopy	89
4.3.2 Contact Angle Measurement and Wettability Analysis	90
4.3.2.1 Pristine Toray Carbon Paper and Functionalized Toray Carbon Paper	90
4.3.2.2 pTP and fTP	91
4.3.3 Electron Microscopy Analysis	92
4.3.4 Brunauer-Emmett-Teller (BET) Analysis	95
4.3.5 X-ray Photoelectron Spectroscopy	96
4.3.6 Electrochemical Characterization	98
4.3.6.1 Electrodeposition of Polyaniline	98
4.3.6.2 Cyclic Voltammetry	99
4.3.6.3 Electrochemical Impedance Spectroscopy	100
4.3.6.4 Galvanostatic Charge-Discharge	101
4.3.6.5 Rate Capability and Cycling Stability	102
4.4 Conclusion	103
4.5 References	104

Chapter 5

Organization of MnO₂ into Grass-like Nanofibril Structure on Electrochemically Modified Carbon Sheets for Flexible Supercapacitor

106-124

5.1 Introduction	107
5.2 Experimental Section	108
5.2.1 Material	108
5.2.2 Preparation of SG (Grafoil-Scotch tape flexible substrate)	108
5.2.3 Electrochemical Anodization	108
5.2.4 Electrodeposition of MnO ₂ Nano-grass	108
5.2.4 Solid-State Flexible Device Fabrication	108
5.2.5 Characterization	109
5.3 Result and Discussion	109
5.3.1 Properties of SG	109
5.3.1.1 Thickness Measurement	109
5.3.1.2 Electron Microscopy Analysis	110

5.3.1.3 Raman Analysis	111
5.3.1.4 X-ray Diffraction	112
5.3.1.5 Conductivity Measurement	112
5.3.1.6 Cyclic Voltammetry Study of Anodized SG	112
5.3.1.7 Flexibility Test	113
5.3.2 Physical Characterization of MnO ₂	113
5.3.2.1 Electronic Microscopy Analysis	113
5.3.2.2 BET Analysis	116
5.3.2.3 X-ray Diffraction	117
5.3.2.4 X-ray Photoelectron Spectroscopy	118
5.3.3 Electrochemical Characterization	119
5.3.3.1 Cyclic Voltammetry	119
5.3.3.2 Electrochemical Impedance Spectroscopy	120
5.3.3.3 Galvanostatic Charge-Discharge	121
5.3.3.4 Durability Test	122
5.4 Conclusion	123
5.5 References	123

Chapter 6

Summary	125
Future Scope and Prospects	130
List of Patents and Publications	131
Erratum	133

Preface

The advent of industrial revolution at the beginning of 19th century spurred a massive production of goods and services which required an enormous amount of fuel to energize the machinery. Fossil fuels, mainly coal and petroleum, were the major fuels used during industrial revolution; still, they occupy a large chunk of the pie of the sources of energy generation. Fossil fuel burning for various uses like electricity generation, transportation, and household application, etc. have released a huge amount of toxic pollutants like sulphur dioxide, nitrogen oxides, carbon dioxide, particulate matter, etc. These effluents and gases have caused serious environmental pollution leading to acid rains, smog, deterioration in air quality and global warming. Global warming caused by enhanced greenhouse effect due to the increased levels of greenhouse gases particularly carbon dioxide has put the survival of life on the plane in jeopardy.

To control the environmental degradation and global warming, the scientific community has put major thrust on the renewable resources of energy such as solar, wind, water, geothermal, etc. Various countries are investing huge sums for the development of alternative renewable resources of energy and, the policies have seen a shift to the sustainable development which demands the cleaner energy sources and optimum and minimal use of available resources. The renewable resources of energy have great prospects as future power sources, however, such resources are available only during a particular period or condition, for instance, sun is not available at night, and wind energy can be harnessed only when the wind speed is high. Thus, the intermittent nature of the non-conventional energy sources is a major challenge towards their widespread application and success. To tackle the issue of intermittency, charge storage device such as batteries and electrochemical capacitors are employed for energy storage during peak operation of non-conventional resources which can be used at a time of requirement.

Among the charge storage devices, electrochemical capacitors have emerged as a highly important technology due to their fascinating properties like simple construction, high power density (3-10 kW kg⁻¹), significant energy density (5-7 Wh kg⁻¹), long cycle life (more than a million cycles), and they are comparatively safer than batteries. However, the low energy density and low practical capacitance of the capacitive materials are the ensuing issues which still need resolution. The pseudocapacitive materials like conducting polymers and metal oxides can exhibit a high capacitance, and energy density due to the involvement of individual

molecules in the redox reaction, *i.e.*, one or more than one e⁻ can be stored per molecule. The theoretical capacitance of the pseudocapacitive materials varies from 200-3000 F g⁻¹, but, the capacitance obtained from these materials is far below at 50-700 F g⁻¹. Such low practical capacitance is attributed to the low electrode-electrolyte interface which depends on the wettability and morphology of the material. At the same time, high resistance due to the high density of grain boundaries compromises the power capability of the material.

Strategies that can enhance the electrochemically active surface area of the pseudocapacitive materials with simultaneous reduction of the grain boundaries can help achieve high energy density with minimal compromise on the power density front. Towards this goal in this thesis, structural alignment of pseudocapacitive materials over carbon morphology has been studied. Different synthesis strategies have been devised to achieve homogenous growth of the active material in one dimension for minimizing grain boundaries. In this strategy, various carbon morphologies like carbon nanotubes, carbon nanofibers, and graphene are used as a current collector as well as the scaffold on the surface of which a thin layer homogenous and uniform layer of pseudocapacitive material is synthesized. This configuration ensures high surface utilization because only the surface which is exposed to the electrolyte is involved in the charge storage, while the inside carbon morphology assures efficient charge collection and transfers to the outer circuit. Also, reduced grain boundaries affected by the directional growth secure high power density and rate capability.

Chapter 1 introduces fundamental concepts of the construction and mechanism of charge-storage in electrochemical capacitors. In the beginning, the importance of charge-storage device in the current scenario and its future prospects are discussed. In the next section, different theoretical models devised for electrochemical double layer structure are explained in detail. An understanding of the charge storage principals and mechanism at the electrode-electrolyte interface is developed through different EDLC models. Afterwards, classification of charge-storage materials is talked about. In this section, properties and importance of each material is described to create an impression of their utility, drawbacks, and improvements that are necessary for far-flung applications. A good deal of importance is given to understanding the underlying theory and mathematical treatment of the origin of pseudocapacitive charge-storage. This chapter then illuminates on types of the redox reactions which give rise to pseudocapacitive charge-storage. Subsequently, properties and application of different metal oxides and conducting polymers which are prepared in this treatise are discussed. The discourse of this chapter then moves towards the importance of structural

alignment of pseudocapacitive materials on the surface of different carbon morphologies which act as conducting cores and a brief discussion on the reported strategies and performance of reported carbon-metal oxide/conducting polymer composites. Also, electrochemical characterization techniques and calculations involved in supercapacitor studies are given. Finally, this chapter ends with a discussion on the scope and objectives of this dissertation.

Chapter 2 discusses on the work strategy adopted to achieve a highly conducting phase of polyethylene dioxythiophene (PEDOT) over the surface of carbon nanotubes (CNTs) in the buckypaper through interfacial polymerization, where the polymerization was confined at the interface of two immiscible liquids. Here, the hydrophilic interaction between the functionalized CNTs and the oxidizing agent (iron perchlorate, $\text{Fe}(\text{ClO}_4)_3$) present in the aqueous phase along with the restricted interaction of the oxidizing agent with the monomer (ethylene dioxythiophene, EDOT) in the organic layer at the immiscible interface is playing a vital role to establish a uniform and aggregate-free growth pattern of PEDOT on CNT. By carefully optimizing the amount of the polymer in the paper, an electrode with a sheet resistance of $3.4 \Omega \square^{-1}$ and equivalent series resistance of 0.95Ω could be prepared. The power density and energy density of the electrode are 9.94 W cm^{-3} and 8.85 mWh cm^{-3} , respectively. The device also delivered a high volumetric capacitance of 18 F cm^{-3} and areal capacitance of 354 mF cm^{-2} .

In **Chapter 3**, a hydrothermal method is proposed where oxygen functional groups incorporated on the surface of CNTs are utilized to polymerize EDOT. PEDOT forms an ultrathin well-aligned coating on the surface of CNTs. This arrangement keeps the number of grain boundaries to the minimum and also increases the electrochemically active surface area. Also, a shear-thinning Xanthan gum- H_2SO_4 gel electrolyte is introduced to overcome the low impregnation of conventional polyvinyl-based electrolyte due to the hydrophobicity of CNT-PEDOT composite. This gel electrolyte on the application of stress lowers its viscosity which helps in the deeper impregnation of electrolyte on the entire available surface. The device showed a very low ESR of 0.31Ω which leads to a high power density of 74 W cm^{-3} .

Chapter 4 describes a strategy wherein the high ESA of PANI has been achieved by the induction of superhydrophilicity together with the alignment of PANI exclusively on the surface of carbon fibers as a thin layer to form a hybrid assembly. Superhydrophilicity is induced by electrochemical functionalization of the Toray carbon paper, which further

induces superhydrophilicity to the electrodeposited PANI layer on the paper, thereby ensuring a high electrode-electrolyte interface. The Toray paper is electrochemically functionalized by the anodization method, which generates a highly active electrochemical surface as well as greater wettability (superhydrophilic) of the carbon fibers. Because of the strong interaction of anilinium chloride with the hydrophilic carbon surface, PANI is polymerized exclusively over the surface of the fibers without any appreciable aggregation or agglomeration of the polymer. The PANI-Toray paper assembly in the solid-state prototype supercapacitor can provide a high gravimetric capacitance of 1335 F g^{-1} as well as a high areal capacitance of 1.3 F cm^{-2} at a current density of 10 A g^{-1} .

The work illustrated in **Chapter 5** deals with how highly thin nanofibers of MnO_2 can be electrodeposited on electrochemically modified carbon sheets. Also, a highly flexible, conducting, and cheap substrate is prepared by simple stick and peel-off method involving Scotch tape and Grafoil. A Grafoil-Scotch tape derived flexible substrate exhibits a sheet resistance of $7 \text{ } \Omega \square^{-1}$ along with a high degree of flexibility and durability. Moreover, its properties are further enhanced by the anodization in order to increase the hydrophilicity and surface area. The substrate is highly thin with a thickness of just $74 \text{ } \mu\text{m}$. The nanofibrous MnO_2 assembly possesses ample porosity allowing for the deeper penetration and facile movement of the electrolyte ions. Very thin MnO_2 fibers result in high electrochemically active surface area which results in high specific capacitance. The fabricated device exhibits high capacitance retention under bent (99%) and twisted (98%) conditions along with a low ESR of $7 \text{ } \Omega$.

Finally, **Chapter 6** summarizes the significant observations and outcomes of each working chapter of the thesis. In the beginning, a brief and concise introduction is given about the need and importance of the structurally aligned growth of the pseudocapacitive materials for obtaining maximum performance in supercapacitors. Afterward, a brief overview of the strategies and primary findings of each chapter are summed up in separate sections. The last part is dedicated to the future scope of the ideas and approach propounded in this treatise in other electrochemical systems like batteries and electrocatalysis.

Chapter-1

Fundamentals of Electrochemical Capacitors and Importance of Structural Alignment of Pseudocapacitive Materials for High-Performance

This chapter introduces fundamental concepts of the construction and mechanism of charge-storage in electrochemical capacitors. In the beginning, the importance of charge-storage devices in the current scenario and its prospects are discussed. In the next section, different theoretical models devised for electrochemical double layer structure are explained in detail.

An understanding of charge storage principals and

mechanism at the electrode-electrolyte interface

developed through different EDLC models.

Afterward, classification of charge-

storage materials is talked about; in this

section properties and importance of

each material is described to create an

impression of its utility, drawbacks,

and improvements that are necessary

for far-flung applications of

electrochemical capacitors. A great deal of

importance is given to understanding the

underlying theory and mathematical treatment of

origin of pseudocapacitive charge-storage. This chapter then

types of redox reactions which give rise to pseudocapacitive charge-storage. Subsequently,

properties and application of different metal oxides and conducting polymers which are

prepared in this treatise are discussed. The discourse of this chapter then moves towards the

importance of structural alignment of pseudocapacitive materials on the surface of different

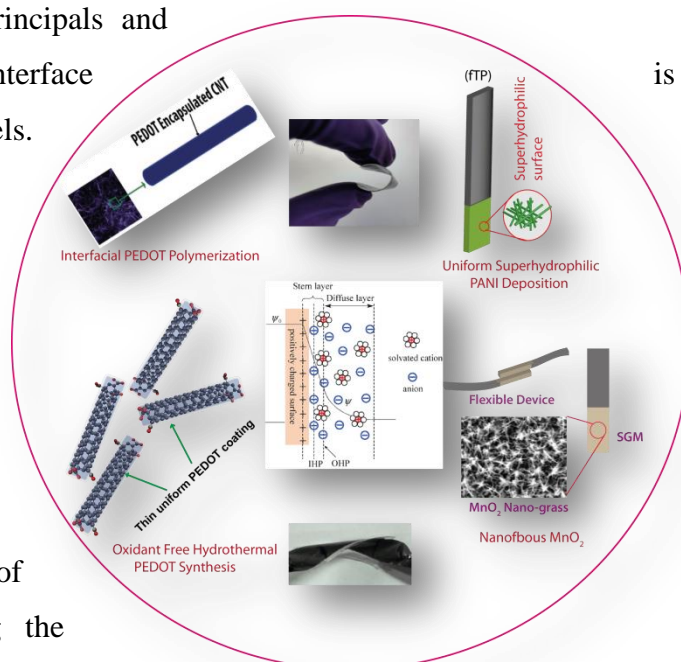
carbon morphologies which act as a conducting core and a brief discussion on the reported

strategies and performance of reported carbon-metal oxide/conducting polymer composites.

Also, electrochemical characterization techniques and calculations involved in supercapacitor

studies are given. Finally, this chapter ends with a discussion on the scope and objectives of

this dissertation.



is

the

illuminates on

1.1 Introduction

The advent of industrial revolution at the beginning of 19th century spurred a large production of goods and services which required an enormous amount of fuel to energize the machinery. Fossil fuels, mainly coal and petroleum, were the major fuels used during the industrial revolution; still, they occupy a large chunk of the pie of the sources of energy generation. Fossil fuel burning for various uses like electricity generation, transportation, and household applications, etc. have released a huge amount of toxic pollutants like sulphur dioxide, nitrogen oxides, carbon dioxide, particulate matter, etc. These effluents and gases have caused severe environmental pollution leading to acid rains, smog, deterioration in air quality and global warming. Global warming caused by enhanced greenhouse effect due to the increased levels of greenhouse gases, particularly carbon dioxide, has put the survival of life on the plane in jeopardy. According to the Inter-governmental Panel on Climate Change (IPCC), under high emission scenario, the temperature of the earth is projected to increase by 2.6-4.8 °C.¹ The increase in temperature is causing melting of polar ice and glacier due to which sea level is projected to rise by 0.3-2.5 m according to National Oceanic and Atmospheric Administration.

To control the environmental degradation and global warming, the scientific community has put major thrust on the renewable resources of energy such as solar, wind, water, geothermal, etc. Various countries are investing huge sums for the development of alternative renewable resources of energy and, the policies have seen a shift to the sustainable development which demands the cleaner energy sources and optimum and minimal use of available resources. The renewable resources of energy have great prospects as future power sources; however, such resources are available only during a particular period or condition. For instance, sun is not available at night; wind energy can be harnessed only when the wind speed is high. Thus, the intermittent nature of the non-conventional energy sources is a major challenge towards their widespread application and success. To tackle the issue of intermittency, charge storage device such as batteries and electrochemical capacitors are employed for energy storage during peak operation of non-conventional resources which can be used at a time of requirement.

Among the charge storage devices, electrochemical capacitors have emerged as a highly significant technology due to their beguiling properties like simple construction, high power density (3-10 kW kg⁻¹), significant energy density (5-7 Wh kg⁻¹), long cycle life (more than a

million cycles), and are comparatively safer than batteries. However, the low energy density and low practical capacitance of capacitive materials are the ensuing issues which still need resolution. Capacitive materials can be broadly classified into electrochemical double layer capacitive (EDLC) materials where the charge is stored only at the electrode-electrolyte interface without any charge transfer and pseudocapacitive materials which perform charge storage through charge transfer and phase change at the electrode-electrolyte interface. EDLC materials suffer from low energy density which is caused by the low charge storage capacity of carbon (0.18 e⁻ are stored per carbon atom)². Moreover, the quantum capacitance³ of the materials with the low density of states like graphene and low electrochemically active surface area of the pseudocapacitive materials are responsible for low capacitance. The charge storage in the electrochemical capacitor is the surface phenomenon in which only the surface accessible to the electrolyte is active for storing charge. The capacitance of the carbon materials cannot increase beyond 22 $\mu\text{F cm}^{-2}$ due to the quantum capacitance phenomenon;⁴ thus, its charge storage has theoretical limitations. However, the pseudocapacitive materials like conducting polymers and metal oxides can exhibit a high capacitance, and energy density due to the participation of individual molecules in the redox reaction, *i.e.*, one or more than one e⁻ can be stored per molecule. The theoretical capacitance of pseudocapacitive materials varies from 200-3000 F g^{-1} but, the capacitance obtained from these materials is far below at 50-700 F g^{-1} . Such low practical capacitance is attributed to the low electrode-electrolyte interface which depends on the wettability and morphology of the material. At the same time, high resistance due to the high density of grain boundaries compromises the power capability of the material.

Strategies that can enhance the electrochemically active surface area of pseudocapacitive material with simultaneous reduction of grain boundaries can help achieve high energy density with minimal compromise on the power density front. Towards this goal in this thesis, structural alignment of pseudocapacitive materials over the various carbon morphologies has been studied. Different synthesis strategies have been devised to achieve homogenous growth of the active material in one dimension for containing grain boundaries. In this strategy, various carbon morphologies like carbon nanotubes (CNTs), carbon nanofibers (CNFs), and graphene are used as the current collectors as well as the scaffolds on the surface of which a thin, homogeneous, and uniform layer of pseudocapacitive material is synthesized. This configuration ensures high surface utilization as only the surface which is exposed to the electrolyte is involved in the charge storage, while the inner carbon core assures efficient

charge collection and transfer to the outer circuit. Also, reduced grain boundaries affected by the directional growth secure high power density and rate capability.

1.2 Fundamentals of Electrochemical Capacitors

1.2.1 Electrochemical Double Layer (EDL)

An electrochemical double layer is the heart of all the electrochemical devices and is fundamental to the interfaces where a surface is in contact with a liquid or solid electrolyte phase. An electrochemical double layer is formed when a conducting surface with an excess or deficiency of surface charges (either positive or negative) are satisfied by the ions of opposite charges from the electrolyte. In the electrochemical double layer capacitors when a potential difference is applied at two electrodes, electrons flow from the conduction band of positive electrode which occupies the valence band on the negative electrode. This movement of charges caused electron deficiency at positive electrode while an excess of electrons is created at the negative electrode. This excess or deficiency of charge is balanced by the ions of opposite charges present in the electrolyte, thus, forming an electrochemical double layer without actual transfer of electron at the electrode-electrolyte interface. Various models have been proposed to explain the structure of EDL which are briefly discussed below.

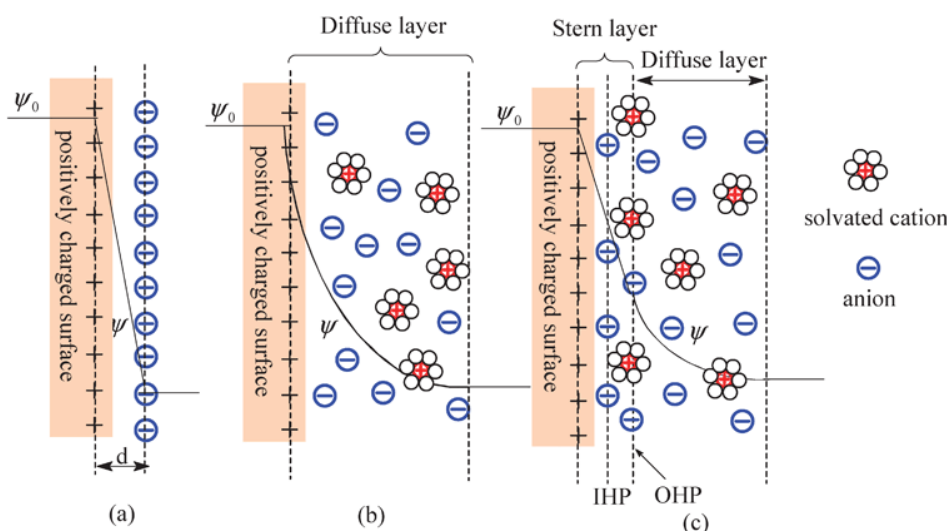


Figure 1. Models of the electrical double layer at a positively charged surface: (a) the Helmholtz model, (b) the Gouy–Chapman model, and (c) the Stern model, showing the inner Helmholtz plane (IHP) and outer Helmholtz plane (OHP). The IHP refers to the distance of closest approach of specifically adsorbed ions (generally anions), and OHP refers to that of the non-specifically adsorbed ions. The OHP is also the plane where the diffuse layer begins. d is the double layer distance described by the Helmholtz model. j_0 and j are the potentials at the electrode surface and the electrode/electrolyte

interface, respectively. (Reproduced by permission from Royal Society of Chemistry, DOI: 10.1039/b813846j; License no. 4331771016501).

1.2.2 Different Models for Electrochemical Double Layer

1.2.2.1 Helmholtz Double Layer Model- The earliest model to describe the structure of double layer was proposed by Hermann von Helmholtz.^{5, 6} He was the first to recognize that the charged electrodes attract the ions of opposite charge and repel the ions of the similar charge. This model is analogous to the parallel plate capacitor. The structure described by Helmholtz is compact where ions are closely bound to the electrode surface. In this model, the stored charge varies linearly with the applied voltage. The capacitance of the double layer is given by

$$C = A\varepsilon/d \text{ ...eq. (1)}$$

where 'C' is the capacitance, 'A' is the area of the electrode, 'ε' represents permittivity of the medium, and 'd' is the thickness of the electrochemical double layer.

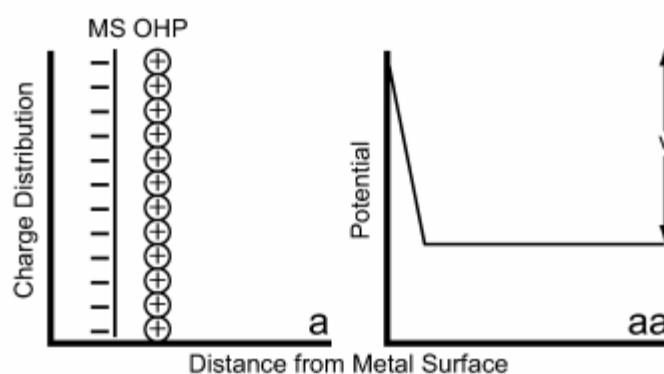


Figure 2. Pictorial representation of the Helmholtz double layer model and the potential variation with distance from the electrode surface. (Reproduced by permission from Springer Nature e-book Fuel cells From Fundamentals to Applications; License no. 4331731210411).

This model gives a good description of an electrochemical interface, but it does not take into account the diffusion or mixing of electrolyte ions, adsorption onto the surface, thermal fluctuations and interaction of solvent dipole moment with an electrode.

1.2.2.2 Gouy-Chapman Model – Louis Goerges Gouy⁷ (1910) and David Leonard Chapman⁸ (1913) observed the change in capacitance with the applied voltage and the ionic concentration. This model improved upon the Helmholtz model by introducing diffuse layer

in which ions are loosely bound and are free to move. This diffuse layer allows for the Maxwell-Boltzmann statistics to be applied to the charge distribution. This model also takes into account the effect of electric and thermal fields on the electrolyte ions. According to this model, the charge distribution varies exponentially with distance from the electrode surface. The diffuse charge (q_D) for an electrolyte with mono-valent ions is given by,

$$q_D = \sqrt{\left(\frac{2kTn_o\varepsilon}{\pi}\right)} \sinh \frac{e_oV}{kT} \dots \text{eq. (2)}$$

The differential capacity is given by the equation,

$$C = \sqrt{\left(\frac{n_o\varepsilon e_o^2}{2\pi kT}\right)} \cosh \frac{e_oV}{2kT} \dots \text{eq (3)}$$

where ' n_o ' is the number of ions of positive and negative sign per unit volume in the bulk of the electrolyte and 'V' is the potential drop from the metal to the bulk of the electrolyte.

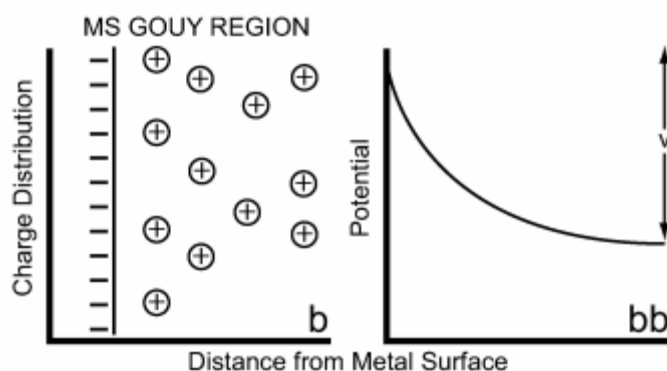


Figure 3. Graphical demonstration of the Gouy-Chapman model and potential variation at the electrode-electrolyte interface. (Reproduced by permission from Springer Nature e-book Fuel cells From Fundamentals to Applications; License no. 4331731210411).

Although the model is a good description of an electrochemical double layer, it does not account for ion-ion interaction which becomes important at high concentration of the electrolyte. Also, it assumes a constant value for the dielectric constant in the region between the electrode and electrolyte.

1.2.2.3 Stern Model (Compact Diffuse-layer Model)- This model given by Otto Stern⁹ in 1924 is a combination of Helmholtz model of the compact double layer and diffuse layer

model of Gouy-Chapman. This model considers charges to be of a finite size which are located at a finite distance from the electrode. In this description, the charge distribution is divided into two component, the Helmholtz component associated with compact layer and charge distribution in the diffuse layer of the Stern model which are in series. The total charge associated with double layer is given by,

$$q = q_H + q_G \dots \text{eq. (4)}$$

' q_H ' is the charge associated with Helmholtz layer while ' q_G ' is the charge contained in the diffuse layer.

Similarly, the potential drop across the interface may be represented as,

$$V_e - V_{el} = (V_e - V_H) + (V_H - V_{el}) \dots \text{eq. (5)}$$

where, the symbol 'e' represents the electrode, 'H' is the Helmholtz layer and 'el' is the electrolyte.

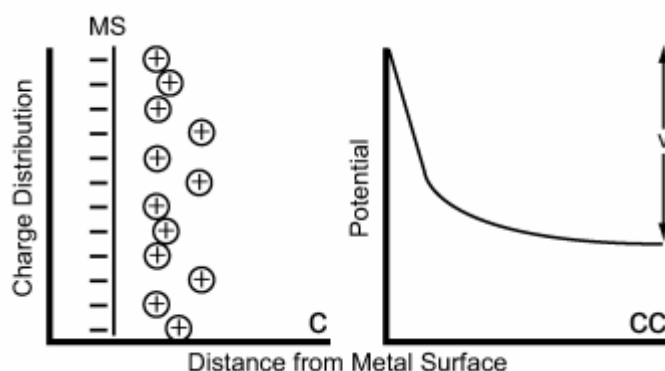


Figure 4. Schematic representation of the Stern model and the change in potential with distance from the electrode surface. (Reproduced by permission from Springer Nature e-book Fuel cells From Fundamentals to Applications; License no. **4331731210411**).

Similar to the Helmholtz model, the potential varies linearly in the compact layer whereas the potential shows semi-exponential variation in the diffuse layer. The total capacitance of the interface can be obtained by differentiating the potential drop across the interface with respect to charge which is the series combination of the capacitance of the Helmholtz layer and the diffuse layer that is given by

$$\frac{1}{C} = \frac{1}{C_H} + \frac{1}{C_G} \dots eq. (6)$$

At a high electrolyte concentration, the value of $1/C_H$ is considerably higher than $1/C_G$. In this case, most of the capacitance is contributed by C_H . At a lower concentration, the thickness of the diffuse layer is much greater which results in higher C_G than C_H , and the double layer structure approaches Gouy-Chapman model. This model fails to explain the differential capacity in the case of specifically adsorbed ions; it also fails to account for the effect of solvent and ion hydration on the structure of double layer.

1.2.2.4 Triple-Layer Model (Esin and Markov¹⁰, Grahame,¹¹ and Devanathan Model¹²) -

This model includes the specifically adsorbed ions in the double layer structure. According to this model, the hydrated ions undergo dehydration in the direction of metal and occupy the space between Helmholtz layer and the electrode. This inner layer between the Helmholtz layer and the electrode is the locus of centers of un-hydrated ions attached to the electrode. Devanathan had derived an equation for the capacitance of the triple layer which is given below.

$$\frac{1}{C} = \frac{1}{C_{M-1}} + \left(\frac{1}{C_{M-2}} + \frac{1}{C_{2-b}} \right) \left(1 - \frac{dq_1}{dq_M} \right) \dots eq (7)$$

where C_{M-1} and C_{M-2} are the integral capacities of inner layer (space between electrode and inner Helmholtz plane) and between inner Helmholtz plane and outer Helmholtz plane, C_{2-b} is the differential capacity of the diffuse double layer, and $\frac{dq_1}{dq_M}$ represents the rate of change of the specifically adsorbed charge with charge on metal. Some interesting implications of this model are:

1. When $\frac{dq_1}{dq_M}$ is zero, the above expression is equivalent to three capacitors in series, *i.e.* inner Helmholtz, outer Helmholtz, and Gouy. Hence, it is called as triple layer model.
2. If $\frac{dq_1}{dq_M}$ is zero, the capacity is minimum.
3. If $\frac{dq_1}{dq_M} > 1$, the differential capacity attains high values.
4. The minimum in the capacity is observed at a potential of zero charge.

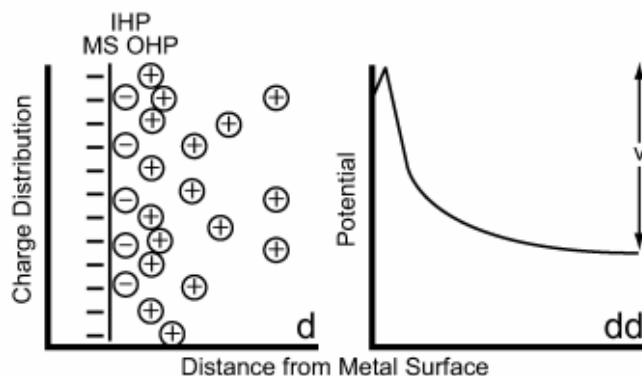


Figure 5. Schematic representation of Triple layer model. (Reproduced by permission from Springer Nature e-book Fuel cells From Fundamentals to Applications; License no. 4331731210411).

1.2.2.5 Water Dipole Model (Bockris-Devanathan-Muller model)—The models discussed above describes the structure of the double layer based on the interfacial charge characteristics of the electrode and ions in electrolyte¹³. As a large number of reactions occur in the aqueous media and other non-aqueous media which are polar, it can contribute to the potential drop at the interface. To include this effect, Bockris, Devanathan and Muller proposed Water Dipole model. According to this model, because of strong interaction between charged electrode and water dipole, a strongly held highly oriented layer of water molecules is formed at the electrode. In this layer, some specifically adsorbed ions can also be present because of strong competitive adsorption. The locus of the center of these ions is the inner Helmholtz plane. Adjacent to this layer is the OHP comprising a layer of solvated ions. OHP is followed by the diffuse layer, which is prevalent in dilute solutions. The first layer of water molecules has a strong orientation (either parallel or anti-parallel to the electric field depending on the charge on the metal) which yields a dielectric constant of 6 for this layer. The second layer of the water molecule is somewhat disoriented due to electric and thermal forces, and, hence, the dielectric constant increases to 40-60. The next layers of water molecules behave like bulk water giving it a dielectric constant of 80.

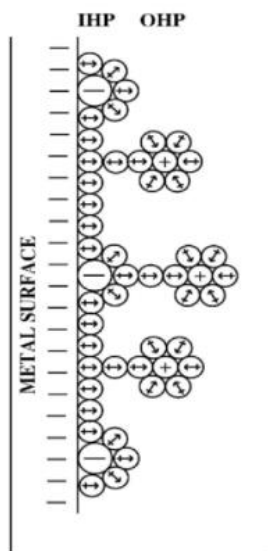


Figure 6. Water Dipole model describing different layers of water dipole. (Reproduced by permission from Springer Nature e-book Fuel cells From Fundamentals to Applications; License no. 4331731210411).

1.2.3 Classification of Electrochemical Capacitors- Electrochemical capacitors are broadly classified into two categories, namely, electrical double layer capacitor (EDLC) and pseudocapacitors depending on the charge storage mechanism. Based on the combination of EDLC and pseudocapacitors, capacitors are also classified as hybrid electrochemical capacitors.

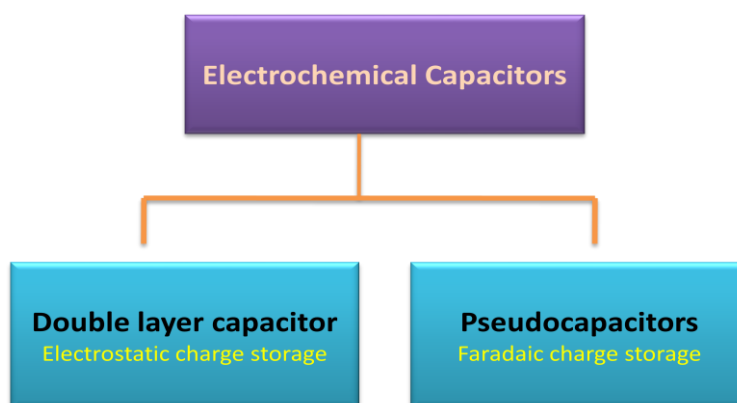


Figure 7. Classification of the electrochemical capacitors.

1.2.3.1 Electrochemical Double Layer Capacitors- EDLCs are the earliest class of capacitors developed for the practical applications. Historically, the double layer charge storage was first observed in the year 1745 by Ewald Georg Von Kleist of Pomerania when he discovered charge storage by connecting a high voltage electrostatic generator to a volume of

water by a connecting wire in glass jar.¹⁴ After one year, a Dutch physicist Pieter van Musschenbroek built a capacitor, named Leyden jar after the name of the city, by cementing metal foils inside and outside of a glass jar.¹⁵ In the Leyden jar, metal foils act as a metal electrode and glass jar work as a dielectric. The image of the earliest capacitor, *i.e.*, Leyden jar is given in Figure 8.

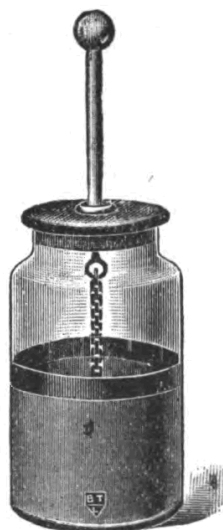


Figure 8. Leyden jar (https://en.wikipedia.org/wiki/Leyden_jar#/media/File:Leyden_jar_engraving.png).

Since then, the double layer charge storage has progressed a great deal during which glass dielectrics have been replaced with aqueous, non-aqueous, gel and solid electrolytes and metal foils are replaced with high surface area carbons. The new systems store an enormous amount of energy made possible by the very high surface area of the electrode and the high dielectric constant of the electrolyte.

1.2.3.1.1 Mechanism of Charge Storage in EDLC- The formation of electrical double involves only the adsorption of electrolyte ion at the interface under the influence of electric field. Ideally, it is a purely electrostatic effect which does not involve any chemical changes under the solvent stability window. The charge storage in the EDL can be understood or explained through the electron density variation at the electrode. During charging, when an electrochemical capacitor is connected to a power source, the surface charge density of the two electrodes is changed.¹⁶ The charge accumulated at the two electrodes is balanced by the ions of opposite charges in the electrolyte moving to respective electrodes. The charge stored in the capacitor is directly proportional to the surface area of the material, to this end high

surface area microporous carbons are used as EDLC material in the commercial supercapacitors which store millions of times more charge than metal plates. However, the surface area of the activated carbon, widely used in electrochemical capacitors, lies between 500-3000 m² g⁻¹ and the capacitance realized lies in the range of 100-250 F g⁻¹.¹⁷ Considering this huge surface area, the capacitance achievable should be much higher than the capacitance obtained. This low realizable capacitance has been explained by the limited accessibility of the electrolyte to the available surface which decreases the material utilization. Recently, the low capacitance of materials with the low density of states such as 2-D systems like semiconductor surface or graphene has been explained by the concept of quantum capacitance given by Serge Luryi in 1987.¹⁸ The quantum capacitance acts as another capacitor connected in series which brings down the resultant capacitance. For single layer graphene having area 2300 m² g⁻¹, the capacitance obtained is 10 μF cm⁻² while for the nitrogen-doped graphene; the areal capacitance has a threshold value of 23 μF cm⁻². Thus, a theoretical limitation is imposed on the capacitance of materials with the low density of states.³

1.2.3.1.2 Materials Exhibiting Double Layer Capacitance- In the conventional dielectric capacitors, metals and metal oxides are used as electrodes. However, in the electrochemical capacitors, different morphologies of carbon with the high surface area and high conductivity are used as electrode materials. The most widely studied and exploited carbon forms are the activated carbons or engineered carbon, carbon nanotubes, carbon nanofiber, graphene, etc. Morphologies like carbon nanohorns, carbon onions are less explored for the electrochemical capacitor application.

1.2.3.1.2.a Porous or Activated Carbon- Activated carbon with microporous (pore size < 2 nm)¹⁹ and mesoporous (2-4 nm)²⁰ structure is the most widely used material in supercapacitors. Activated carbon is produced from carbonaceous materials such as coconut husk,²¹ bamboo,²² willow peat²³, wood,²⁴ coir,²⁵ lignite,²⁶ coal²⁷ and petroleum pitch.²⁸ During synthesis, carbonaceous materials are first pyrolyzed at a high temperature (450-900 °C) in the presence of inert gases such as nitrogen or argon to obtain the carbon. This carbon is then activated mainly through two processes, physical activation²⁹ or chemical activation.³⁰ In physical activation of carbon, it is exposed to an oxidizing atmosphere such as steam or oxygen in the temperature range of 600-1200 °C. In the chemical activation process, the source material is mixed with acid (phosphoric acid), a strong base (sodium hydroxide, potassium hydroxide) or salt (calcium chloride). It is then carbonized at high temperatures.

Thus, carbonization and activation take place simultaneously. Activated carbon possesses high specific surface area up to the order of $3000 \text{ m}^2 \text{ g}^{-1}$. Thus, it can store an enormous amount of charge at the interface compared to the conventional metal capacitors. Also, it possesses high electronic conductivity which results in high power capability, making it ideal for high power applications. As the charge storage is essentially taking place at the surface, the process is highly reversible with high response time, and as the chemical nature of carbon is not affected within safe working voltages, they usually exhibit high cycle life (can be cycled millions of times). In addition to the above advantages, carbon can be operated under a high potential window of 2.5-3.0 V in organic electrolytes.³¹ Thus, wide operating voltage and high energy density can be obtained. The charge storage of activated carbon can be further improved by introducing surface functional groups which provide significant pseudocapacitance to the carbon.³² Hetero-atom doping with elements like N,³³ S, P,³⁴ B,³⁴, etc. has also shown to improve the charge storage ability in carbon by introducing bond polarization and enhanced charge density.³⁵

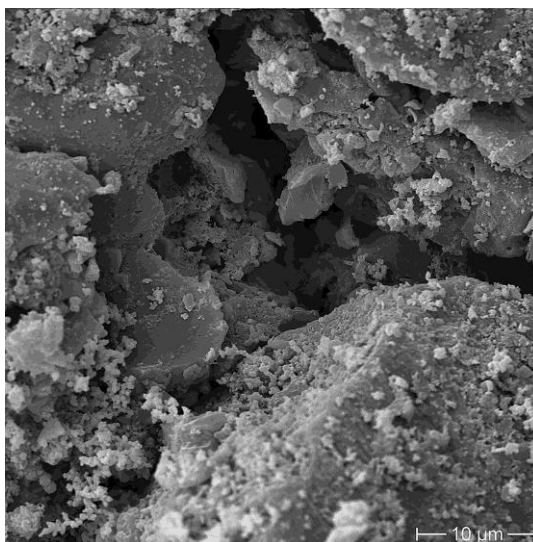


Figure 9. Scanning electron microscope image of activated carbon (source <https://commons.wikimedia.org/wiki/File:ActivatedCharcoal.jpg>).

1.2.3.1.2.b Carbon Nanotubes (CNTs)– Carbon nanotubes, discovered in 1991 by Sumio Iijima,³⁶ are the cylindrical nanostructures of carbon. They have a tubular structure; the properties of CNTs depend on the axis of rolling. The pristine CNTs are made up of sp^2 hybridized carbon layer which is rolled into tubes. CNTs possess very unusual properties which are highly important in electronics, optics, and material science. CNTs are the stiffest materials discovered till date with the tensile strength of 63 gigapascal and specific strength of

48000 kNm kg⁻¹ (high carbon steel has specific strength of 154 kNm kg⁻¹).³⁷ From the point of view of electrochemical applications, it possesses high electrical conductivity in the range of 10⁴-10⁵ S cm⁻¹ along with high thermal conductivity (3500 W·m⁻¹·K⁻¹) which provide excellent heat dissipation during device operation.³⁸ This extraordinary electrical and thermal conduction is caused by the nanoscale cross-section which allows conduction only along the tube axis giving rise to ballistic transport.³⁹ Depending upon the number of carbon layers, they are classified as single-walled carbon nanotubes (SWCNT), double-walled carbon nanotubes (DWCNT) and multiwalled carbon nanotubes (MWCNT). CNTs also possess high SSA which is 1315 m² g⁻¹ for SWCNT to 300 m² g⁻¹ for MWCNT which is important for the electrochemical applications.⁴⁰ CNTs were first applied in electrochemical capacitors by Niu et al. in 1997, MWCNTs with a surface area of 430 m² g⁻¹ showed the capacitance of 102 F g⁻¹.⁴¹ Since then CNTs have been extensively researched for the electrochemical capacitors. CNTs have been modified through surface functionalization using chemical and physical approaches, hetero-atom doping to manipulate their electronic properties, making composites of CNTs with other material like metal oxides and conducting polymers. CNTs have a high surface to volume ratio which makes ideal for the deposition of other capacitive material along the axis, where the CNT core can provide better current collection and transport.

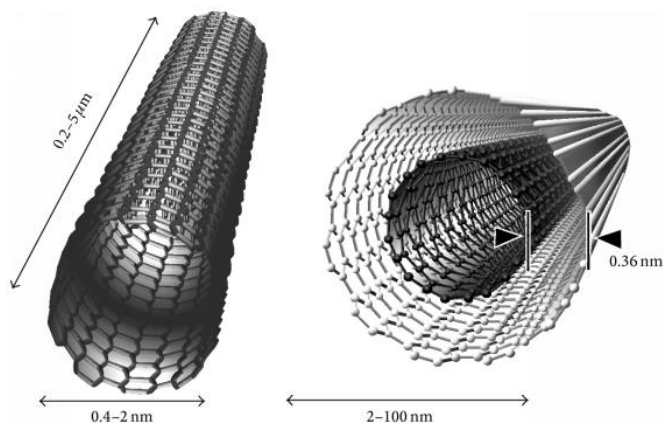


Figure 10. Graphic representation of the construction of SWCNT and DWCNT. (Reproduced by permission from Journal of Nuclear Medicine, doi: 10.2967/jnumed.107.041723).

1.2.3.1.2.c Graphene- According to the International Union for Pure and Applied Chemistry (IUPAC), graphene is defined as “a single carbon layer of graphite structure, describing its nature by analogy to a polycyclic aromatic hydrocarbon of quasi-infinite size”.⁴² In 2004,

Andre Geim and Kostya Novoselov isolated a single atom thick sheet of carbon which they named graphene.⁴³ The importance of the discovery of graphene can be judged by the fact that Geim and Novoselov were awarded Nobel Prize in physics in 2010. Graphene is a wonder material which has far-reaching applications encompassing the fields of medicine, material science, engineering, nanotechnology, energy, etc.⁴⁴ Since its discovery, a large number of articles involving graphene have been published, showing the scale of research focussing graphene. Graphene shows very high electron mobility with theoretical limits of $200000 \text{ cm}^2 \text{ V}^{-1} \text{ s}^{-1}$ and practical mobility as high as $15000 \text{ cm}^2 \text{ V}^{-1} \text{ s}^{-1}$ has been achieved.⁴⁵ Graphene consists of highly delocalized electrons called pi-electron above and below the plane of graphene; these delocalized electrons endow graphene with exceptional electronic and thermal conductivities. Graphene synthesis has progressed a great deal in recent years. High-quality graphene can be synthesised by chemical vapour deposition technique, molecular beam epitaxy, micromechanical cleavage, photo-exfoliation, precipitation from metal, etc. However, these methods produce graphene in low quantities.⁴⁴ For large-scale graphene synthesis, Hummer's method and exfoliation of graphite in organic solvents are the well-known methods.⁴⁶ Recently, electrochemical exfoliation of graphite has been reported for graphene synthesis in significant quantities.⁴⁷

Properties like high SSA ($2630 \text{ m}^2 \text{ g}^{-1}$), good electrical conductivity, flexibility and high mechanical strength make it an ideal material for electrochemical capacitors with theoretical capacitance of 550 F g^{-1} .⁴⁸ Rao et al.⁴⁹ demonstrated the application of graphene in EDLC in 2008 and later by Rouff et al.⁵⁰ Gravimetric capacitance obtained for graphene ranges from 150 F g^{-1} to 298 F g^{-1} depending upon the synthesis method, surface area, pore size, etc. However, the capacitance of graphene is limited by quantum capacitance phenomenon caused by the low density of states which puts the limit of $13.5 \text{ } \mu\text{F cm}^{-2}$.³ Heteroatom doping of graphene with nitrogen, boron, phosphorus, sulphur, etc. has shown to improve the capacitance of graphene.⁵¹ For nitrogen doped single-layer graphene, the areal capacitance has been shown to improve to $23 \text{ } \mu\text{F cm}^{-2}$ compared to $13.5 \text{ } \mu\text{F cm}^{-2}$ for pristine graphene.⁵²

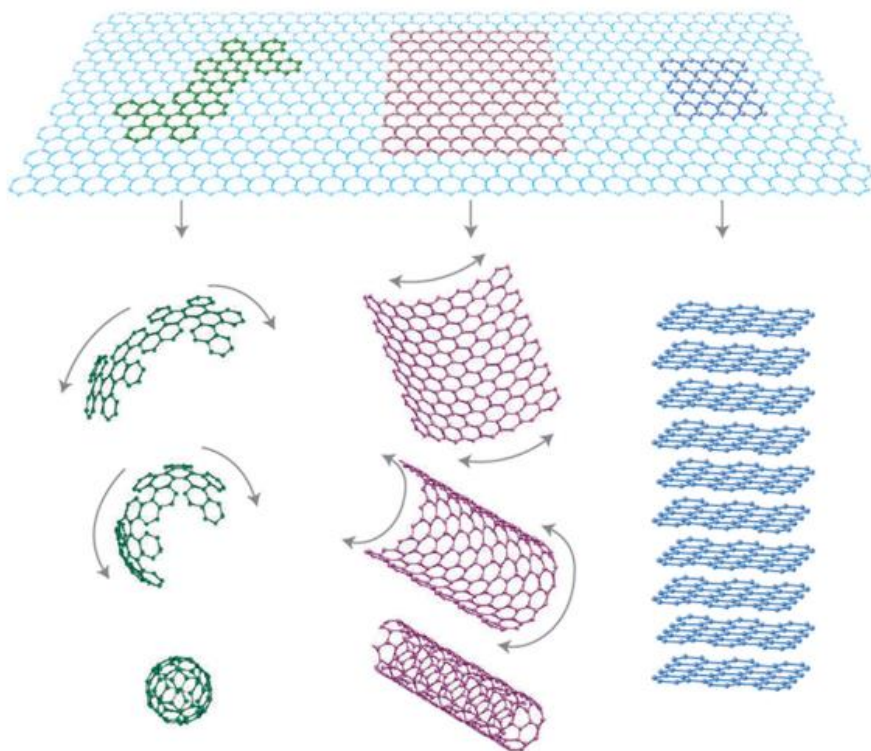


Figure 11. Graphene rightly called as mother of all carbon morphologies; the figure depicts the evolution of different carbon morphologies from 2D graphene sheet. (Reproduced by permission from Springer Nature License no. 4331741199891).

1.2.3.1.2.d Carbon Nanofibers- Graphene layers arranged as stacked cones, cups or plates give rise to cylindrical nanostructures called carbon nanofibers (CNFs), vapour grown carbon fibers (VGCFs), or vapor grown carbon nanofibers (VGCNFs). The earliest technical records for the carbon nanofibers date back to 1889 by Hughes and Chamber for the filamentous carbon.⁵³ Vapour grown carbon nanofibers have a smaller diameter (less than 200 nm) whereas the diameter of the vapour grown carbon fibers is comparatively larger. CNFs are easy to synthesis, possess high electrical conductivity, high aspect ratio, and capability to form free-standing films make them interesting for many electrochemical applications like supercapacitors, batteries, fuel cell, etc.⁵⁴ Carbon nanofibers are prepared through chemical vapour deposition technique in which gas phase molecules (hydrocarbons) are decomposed over the transition metal catalyst such as Fe, Co, Ni, Mn, MgO, Al₂O₃, etc.⁵⁵ Decomposition of hydrocarbons results in the deposition of carbon over the catalyst around which the growth of carbon fiber takes place. A relatively different technique involving the synthesis of polyacrylonitrile films through electrospinning followed by stabilization and carbonization produces continuous carbon nanofibers.⁵⁶ Surface area as high as 1162 m² g⁻¹ can be achieved through various physical and chemical activation processes similar to the activation of

carbon.⁵⁷ Versatile properties of CNF have led to its application in therapeutic drugs, rechargeable Li-ion batteries, as a field emission source, and also in electrochemical capacitors. The capacitance value of 140 F g^{-1} has been achieved for activated carbon nanofibers.⁵⁸ Although the capacitance obtained with CNF is low, they have been used to synthesize composite material in conjunction with different metal oxides like MnO_2 ,⁵⁹ conducting polymers such as PEDOT⁶⁰ through different synthesis procedures for high-performance electrochemical capacitors. A CNF paper derived from the carbonization of PAN-based paper with SSA $705 \text{ m}^2 \text{ g}^{-1}$ was used as a binder-free electrode in a supercapacitor; it showed 100 F g^{-1} in organic electrolyte and area normalized capacitance of $67 \mu\text{F cm}^{-2}$ in aqueous electrolyte.⁶¹ CNF has also been derived from pyrolysis of bacterial nanocellulose, Yu et al. synthesized nitrogen-doped CNF through hydrothermal treatment bacterial cellulose at a temperature of $180 \text{ }^\circ\text{C}$ for 12 h which showed the capacitance of 194 F g^{-1} at a current density of 1 A g^{-1} .⁶²

1.2.3.1.2.e Carbon Nanohorns- Carbon nanohorns (CNHs) are the aggregated graphene which is arranged in a horn-shaped sheath. CNH is derived from SWCNT having tube length in the range of 40-50 nm and about 2-3 nm in diameter; it possesses a five-pentagon conical cap with a cone opening angle of approximately 20° .^{63, 64} SWCNH can be synthesized from CO_2 laser ablation and arc discharge method.⁶⁵ In CO_2 laser ablation method, a graphite rod is exposed to a high power CO_2 laser in the presence of argon; this method produces SWCNHs at room temperature without using any catalyst. In arc discharge method, SWCNHs are obtained by a simple pulsed arc discharged between two graphite rods (preheated to $1000 \text{ }^\circ\text{C}$) at an arc current of 120 A and 15 V voltage between the rods. SWCNH produced by this method is of superior quality with 90 % purity compared to CO_2 laser ablation. CNH possesses microporosity as well as mesoporosity caused by the specific structure of the nanohorns. Application of CNH in the electrochemical capacitor was first demonstrated by Yang et al., CNH exhibited a capacitance of 66 F g^{-1} in an aqueous electrolyte which increased to 114 F g^{-1} for the oxidized SWCNH. This capacitance enhancement after oxidation was attributed to the generation of porosity due to functionalization.⁶⁶ A composite of CNT and SWCNH was demonstrated by Hata et al. which showed a capacitance of 63 F g^{-1} in the organic electrolyte and exhibited good rate capability, retaining 71 % capacitance when current density increased 500 times.⁶⁷ Low capacitance of CNH compared to the other carbon morphologies has hindered its development as a capacitive material.

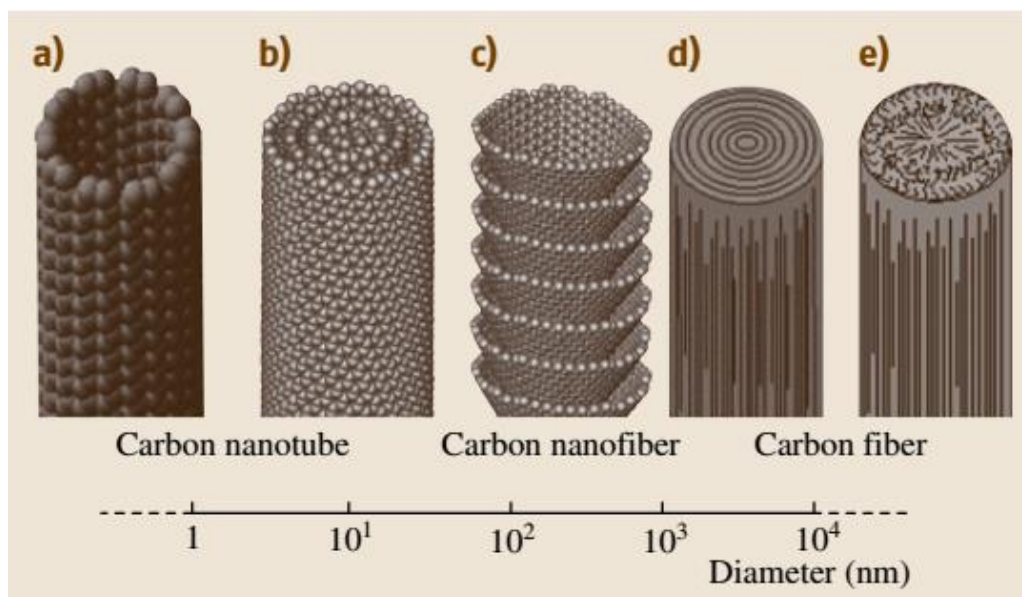


Figure 12. Schematic comparison of the diameter dimensions on a log scale for various types of fibrous carbon materials. (Reproduced by permission from Springer Nature, Springer Handbook of Nanomaterial; License no. 4331760171393).

1.2.3.2 Pseudocapacitors- Double layer capacitance as discussed arises due to the potential dependence of the surface density of charges stored electrostatically at the electrode-electrolyte interface. On the capacitor electrode, the accumulated charge is a combination of excess or deficit of conduction band electrons which are balanced by the charge densities of the cations and anions of the electrolyte. In such charge storage, the charge does not cross both sides of the electrode-electrolyte interface; in other words, charge transfer does not occur across the interface. In contrast, pseudocapacitance charge storage arises out of a completely different mechanism which is Faradaic in nature, *i.e.*, charge transfer indeed occurs during which material changes its oxidation state. Also, the charge storage in pseudocapacitors is different from the batteries (Faradaic charge storage) which arise on account of a relation between the extent of charge acceptance (Δq) and the potential change (ΔV) so that the derivative $dq/dv \neq 0$. This derivative gives the value of capacitance. However, in batteries charge and discharge is not a function of potential; batteries show discharge at a constant potential. Hence, $dq/dv = 0$. From thermodynamic aspect, pseudocapacitive charge storage arises when some property (y), proportional to charge passed, is related to the potential by the equation.⁶⁸

$$\frac{y}{1-y} = K \exp\left(\frac{VF}{RT}\right) \dots \text{eq. (8)}$$

The quantity 'y' can be the fractional coverage of the electrode (for example H at Pt), an extent of fractional coverage of ions in some intercalation host, or extent of conversion of an oxidized species to a reduced species or vice-versa in an electrolyte solution. Thus, pseudocapacitance appears when the extent of reaction (Q) is a continuous function of potential so that dQ/dV arises that has properties of capacitance. Such charge storage is Faradaic in nature involving changes in the chemical state of reactant species unlike the double layer charge storage where chemical changes in the material do not occur.

1.2.3.2.1 Types of Pseudocapacitance- Pseudocapacitance is classified into adsorption, redox, and intercalation pseudocapacitance. Their origin is discussed hereafter.

1.2.3.2.1.a Origin of Adsorption Pseudocapacitance- The differential capacitance of an electrode-electrolyte interface arising due to the change in coverage of electroactive species with potential across the interface is categorized as adsorption capacitance.⁶⁹ Adsorption pseudocapacitance is generally observed for the electrochemical reactions where an electron transfer precedes rate-determining step. Underpotential deposition (UPD) of hydrogen on Pt, UPD of Pb over Au are few examples of the process that results in adsorption pseudocapacitance.⁷⁰ Pseudocapacitance is given by the change in charge; here, charge is a function of surface coverage with potential. Thus, charge is given by

$$q = q_0 \Theta \dots \text{eq. (9)}$$

where, Θ is the surface coverage and q_0 is the charge when $\Theta=1$.

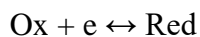
$$\text{Then, } C_p = q_0 \left(\frac{d\Theta}{dV} \right) \dots \text{eq. (10)}$$

Adsorption pseudocapacitance depends on the type of adsorption isotherm. For the Langmuir adsorption isotherm, pseudocapacitance is given by

$$C_p = \frac{q_0 F}{RT} C_A \frac{K_1 \exp(VF/RT)}{(1 + C_A K_1 \exp(VF/RT))^2} \dots \text{eq. (11)}$$

In case of H UPD on Pt surface with 10^5 Pt sites per cm^2 , maximum capacitance, when $\Theta=0.5$, is $1.6 \times 10^3 \mu\text{F cm}^{-2}$. This value is 100 times higher than the double layer capacitance at the ideally polarisable interface.

1.2.3.2.1.b Origin of Redox and Intercalation Pseudocapacitance⁷⁰ - Redox pseudocapacitance arises due to the oxidation or reduction of reactant species at the electrode-electrolyte interface. Consider a reaction,



The Nernst equation can be written for the above reaction as,

$$E = E^{\circ} + (RT/F) \ln[\text{Ox}]/[\text{Red}] \dots \text{eq}(12)$$

The equation can be re-written as,

$$E = E^{\circ} + (RT/F) \ln[\text{Ox}/Q]/[\text{Red}/Q] \dots \text{eq} (13)$$

$$E = E^{\circ} + (RT/F) \ln[\text{Ox}/Q]/(1-[\text{Ox}/Q]) \dots \text{eq.} (14)$$

Where, Q is the amount of Ox or Red available for the reaction.

Since $[\text{Ox}]+[\text{Red}]=Q$, the equation can be rearranged as,

$$[\text{Ox}/Q]/(1-[\text{Ox}/Q]) = \exp (E-E^{\circ})F/RT \approx \exp(\Delta E \cdot F /RT) \dots \text{eq.} (15)$$

Where, E° is the standard potential for the redox couple.

When the above equation differentiated with ΔE , a formal capacitance quantity is obtained which can be experimentally measured.

Intercalation of metal-ion into a host material has been widely used for high energy density metal-ion batteries, e.g., Li-ion battery. Intercalation phenomenon exemplifies the transition between supercapacitor and battery behaviour. Consider the intercalation of Li into an intercalation host such as TiS_2 , as the Faradaic charge is required for deposition of Li in the intercalation host, the amount of Li intercalated (X) depends continuously on the charge passed. The differentiation of X with V gives rise to a pseudocapacitive quantity which is given by,

$$E = E^{\circ} + (RT/F) \ln[X/1-X] \dots \text{eq.} (16)$$

The intercalation pseudocapacitance shows similarity to the adsorption pseudocapacitance due to quasi-two-dimensional nature of ion intercalation occurring at the layer surfaces in the Van der Waal gaps of the host lattice.⁷¹ The cyclic voltammogram behaviour is similar to the CV

responses for adsorption pseudocapacitance which is shown in Figure 13 for the intercalation of Li in MoO₂.

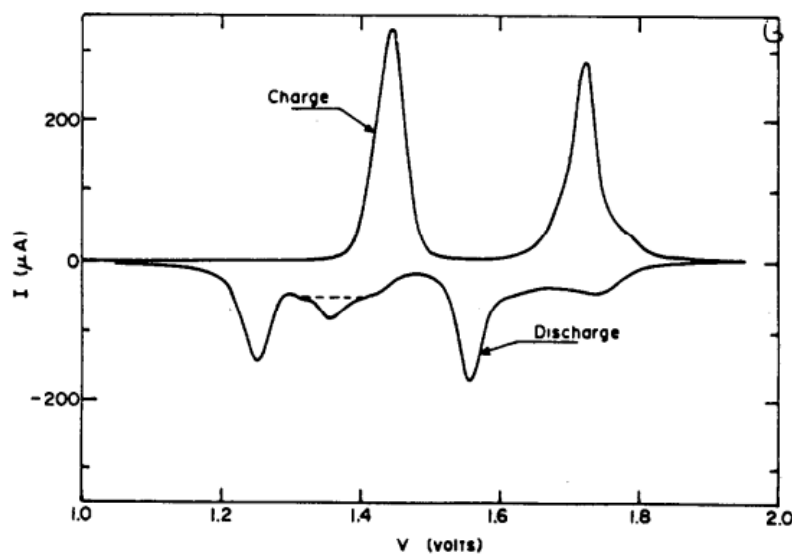


Figure 13. Cyclic voltammogram (sweep rate $9.6 \mu\text{V s}^{-1}$) for Li intercalation into MoO₂. (Reproduced by permission from Elsevier; License no. 4331851252949)

1.2.3.2.2 Pseudocapacitive Materials-Pseudocapacitive materials include transition metal oxides, metal sulphides, metal hydroxides, and metal nitrides, intercalating materials and conducting polymers. These materials exhibit high capacitance due to the redox reaction. Every molecule participates in the Faradaic charge transfer, and thus these materials exhibit high energy density. However, compared to EDLC materials, they exhibit low power density and low rate capability due to kinetic limitations on the charge transfer reaction. Moreover, they suffer from a low electrochemically active surface area which gravely impedes the capacitance obtained from these materials. Some strategies have been devised to overcome the limitations which are discussed hereafter in this treatise.

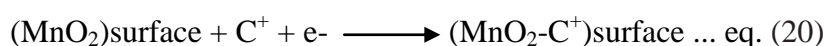
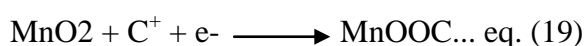
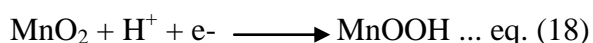
1.2.3.2.2.a Transition Metal Oxides (TMOs)- Transition metal oxides such as RuO₂, MnO₂, V₂O₅, Co₃O₄, Mn₃O₄, Fe₃O₄, Fe₂O₃, etc. have shown to exhibit pseudocapacitive charge storage through redox reaction.⁷² During charge storage, the transition metal atom undergoes a change in the oxidation state through electron transfer at the electrode-electrolyte interface resulting in Faradaic charge storage. Among TMOs, RuO₂ was the first TMO to show pseudocapacitive charge storage and has been extensively studied since then. It possesses quasi-metallic conductivity allowing facile electron transfer, good stability and involves multiple oxidation state transitions which consequently result in high capacitance under a

voltage window of 1.4 V.⁷³ RuO₂ can show multiple oxidation states, Ru²⁺, Ru³⁺, Ru⁴⁺, Ru⁶⁺, with high reversibility, an equation showing redox transition is given in eq. 17. RuO₂ had shown to exhibit rate capability comparable to EDLC material retaining 75 % capacitance when the scan rate increased from 2 to 500 mV s⁻¹.⁷⁴



Its high conductivity and presence of structural water in the RuO₂ lattice help in high material utilization exhibiting capacitance as high as 1340 F g⁻¹, almost 96 % of the theoretical capacitance.⁷⁵ It showed great promise for use in commercial electrochemical capacitors, but it is highly expensive and toxic which has severely impeded its prospects of application in capacitors.

Another TMO which has shown good capacitive behaviour is MnO₂; it is low cost and environmentally friendly. Its synthesis is easy and economical and can be prepared from various methods like electrochemical deposition,⁷⁶ hydrothermal syntheses,⁷⁷ room temperature reduction of KMnO₄,⁷⁸ etc. MnO₂ exists in different phases, namely, α, β, γ, and δ-MnO₂.^{79, 80} Except δ-MnO₂, other three phases have tunnel structure; such tunnel structure is important to access the inner surface of MnO₂. α-MnO₂ possesses large tunnel structure (2X2 octahedral units) compared to the other phases and is known to exhibit high capacitance than the other MnO₂ phases.⁸⁰ Lee and Goodenough in 1999 demonstrated the charge storage properties of MnO₂ in KCl solution which exhibited capacitance of 200 F g⁻¹. This study also showed that strong acids could be replaced by mild aqueous salt solution as electrolyte.⁸¹ The charge storage mechanism in MnO₂ involves tunnelling of Mn oxidation state between III and IV with simultaneous adsorption or intercalation of H ion or alkali metal ion. The diffusion coefficient of H ion in MnO₂ is of the order of 6 x 10⁻¹⁰ cm² s⁻¹; such a low diffusion coefficient of H ion infers that the involvement of intercalation mechanism is less likely.⁸² Following equation shows the intercalation and adsorption mechanism of charge-storage in MnO₂.⁸²



Due to the restricted adsorption or intercalation of cation in the MnO_2 , only thin films exhibit good capacitance values. Moreover, low conductivity of MnO_2 (10^{-5} to 10^{-6}) impedes its rate capability considerably.⁸³ Thicker MnO_2 films show capacitance in the range of 200-250 F g^{-1} caused by the impervious inner surface and less active sites for charge transfer. For 5 μm thick films of MnO_2 , Belanger *et al.* obtained the capacitance as high as 1380 F g^{-1} which for 100 μm thick films decreased to 150 F g^{-1} . These results show that thicker films of MnO_2 possess low electrochemically active surface area with largely inaccessible MnO_2 molecules.⁸²

In recent years, spinel metal oxides such as NiO , Co_3O_4 , Fe_3O_4 , Mn_3O_4 and mixed transition metal spinels such as NiCo_2O_4 and MnFe_2O_4 have been demonstrated as promising high-performance pseudocapacitive materials for their high theoretical capacitance ($>3000 \text{ F g}^{-1}$). Shen *et al.* synthesized nano/micro NiO superstructures with hierarchical porosity which showed capacitance of 710 F g^{-1} at 1 A g^{-1} current density.⁸⁴ Mesoporous Co_3O_4 nanowires grown directly on Ni foam was synthesized by Zhang *et al.* through hydroxide precipitation and calcinations showed very high capacitance of 1160 F g^{-1} at a current density of 2 A g^{-1} .⁸⁵

1.2.3.2.2.b Conducting Polymers- Conjugated organic polymers which are intrinsically electronic conductors are called conducting polymers. The synthesis of conducting polymers dates back to 1862 when H. Letheby at the college of London hospital electropolymerized aniline sulphate into a bluish-black solid layer on a Pt electrode. The chemical nature and electrical conductivity were unknown at that time.⁸⁶ In 1977, Alan J. Heeger, Hideki Shirakawa, and Alan G. MacDiarmid reported an electrically conducting doped polyacetylene.⁸⁷ World record for the organic polymer was set in 1987 by Naarmann and Theophilou for stretched iodine-doped polyacetylene, they reported 100,000 S cm^{-1} conductivity value.⁸⁸ Since then many conducting polymer have been synthesised and a number of applications have been demonstrated. From the electrochemical capacitor electrode point, polyaniline, polypyrrole, polythiophene and poly(3,4-ethylene dioxythiophene) have emerged as important conducting polymers.⁸⁹ These conducting polymers in their doped state, *i.e.*, oxidized or reduced, are highly conducting and show pseudocapacitive charge storage through doping-dedoping of conjugated polymer chains.

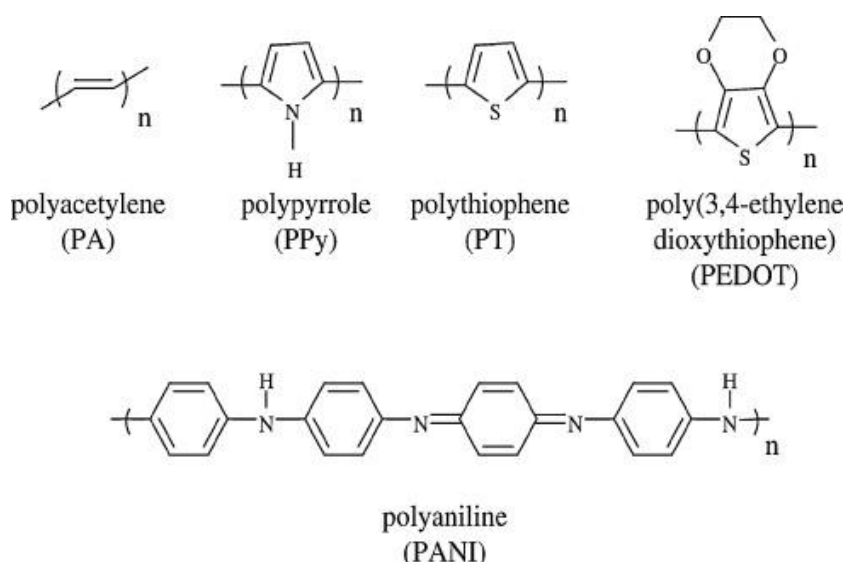


Figure 14. Chemical structure of a few conducting polymers. (Reproduced by permission from Elsevier, doi.org/10.1016/j.jcis.2009.09.029; License no. 4331840152711).

Most common method for synthesis of conducting polymer is the oxidative polymerization where an oxidizing agent oxidizes the monomer forming a radical cation which then undergoes chain growth.⁹⁰ The quality of polymer synthesized depends upon the rate of polymerization, the crystallinity of the polymer chain, etc. Electropolymerization, where the oxidation of monomer is performed by the application of current has also been widely used. Electropolymerization gives better control of the synthesis and it can directly be polymerization over the current collector giving better contact to it.⁹⁰ Vapour phase polymerization has also been used to form thin films and needle-like morphologies of conducting polymers. Conducting polymers possess high capacitance, wide potential window (1.2 V), easy to synthesis, good stability, and possess high energy density. All these attributes make it ideal for the electrochemical capacitors.

1.2.3.2.2.b.i Poly (3,4-ethylene dioxythiophene) (PEDOT) - PEDOT is a conducting polymer which belongs to the class of polythiophenes. PEDOT is generally prepared by the oxidative polymerization of 3,4-ethylene dioxythiophene using an oxidizing agent like FeCl_3 ,⁹¹ $\text{Fe}(\text{ClO}_4)_3$,⁹² ammonium persulphate,⁹³ etc. PEDOT exhibits high conductivity which strongly depends upon the counter ions and the highest conductivity is reported for the perchlorate ion (780 S cm^{-1}).⁹⁴ The conductivity of PEDOT also depends on the crystallinity of the polymer chains; high crystallinity leads to the better intra-chain charge carrier mobility as well as inter-chain charge hopping resulting in high conductivity.⁹⁵ PEDOT is highly stable even in the doped conditions under ambient conditions. High stability of PEDOT results from

the electron donating effect of the two oxygen atoms present at the 3,4 position balancing the positive charge on the oxidized polymer chain. Also, the structure of the monomer allows the polymerization at 2 and 5 positions resulting in the well-ordered polymer chains containing fewer defects compared to polythiophene.⁹⁶

PEDOT has been demonstrated as a promising material for the electrochemical capacitors owing to its desirable attributes like high conductivity, ease of synthesis, environmental stability, good theoretical capacitance (210 F g^{-1}) and wide operating potential window (1.2).⁹⁷ The first demonstration of PEDOT as a capacitive material in the electrochemical capacitor was given by Frackowiak *et al.* in the report in 2004.⁹⁷ The PEDOT-CNT composite exhibited a capacitance of 60 to 160 F g^{-1} in different electrolytes. They showed that PEDOT is stable in all the electrolytes, acidic, basic and organic electrolytes. Since then, literature has been flooded with a large number of reports on PEDOT and its application in electrochemical capacitors. Highly conducting phase of PEDOT was synthesized by EDOT polymerization at the aqueous/organic interface on the cellulose paper. PEDOT exhibited a high conductivity of 375 S cm^{-1} with the sheet resistance of only $3 \Omega \square^{-1}$; the flexible PEDOT paper supercapacitor showed a high volumetric capacitance of 11 of 145 F cm^{-3} along with an energy density of 1 mWh cm^{-1} .⁹²

1.2.3.2.2.b.ii Polyaniline (PANI) - Polyaniline is one of the most studied intrinsically conducting polymers. Although discovered in 1862 as a bluish-black mass, it only attracted the interest of scientific community after the rediscovery of conductivity in conjugated polymers. Similar to the other conducting polymers, it is also polymerized through oxidative polymerization, electropolymerization, and vapour phase methods.⁹⁸ Polyaniline is a cost-effective material that can be easily synthesized, and its blend with polystyrene sulphonate is easily processible.⁹⁹ Polyaniline has been shown to exhibit metallic transport¹⁰⁰ with conductivity as high as 1000 S cm^{-1} , but solution processed PANI generally shows low conductivity. Depending on the degree of oxidation, three different states of PANI are identified, leucomeraldine base (completely reduced), emeraldine base (half oxidized) and pernigraniline base (completely reduced).¹⁰¹ Only half oxidized state of PANI, *i.e.*, the emeraldine base is conducting due to delocalization of charge along the polymer chain. Polyaniline is a highly beguiling material for electrode material in electrochemical capacitor owing to its high theoretical capacitance, environmental stability, low-cost monomer and ease of synthesis. Although PANI possesses high theoretical capacitance, high capacitance is difficult to realize due to low conductivity and low electrolyte accessible surface area.

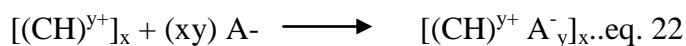
Polyaniline and its composite with various carbon morphologies and metal oxides have been studied in detail. A flexible graphene-PANI composite paper prepared by anodic electrodeposition of aniline was reported by Cheng *et al.*; the composite paper showed a gravimetric capacitance of 233 F g^{-1} but charge transfer resistance was high.¹⁰² Capacitance value of 480 F g^{-1} was reported for the PANI hydrogel prepared using phytic acid as a gelator. The high capacitance was attributed to the high surface area and good conductivity of the PANI hydrogel.¹⁰³

1.2.3.2.3 Doping in Conducting Polymers¹⁰⁴⁻¹⁰⁶ - The usage of term doping in conducting polymers is taken from the doping of semiconductor in condensed matter physics. However, the processes are mechanistically different but phenomenologically similar as it results in a great deal of improvement in conductivity in semiconductors and CPs. Hence, the term doping can confuse the mind of the reader if he/she is not aware of the process of doping in CPs. Doping in semiconductors is referred to the introduction of impurity atom in host lattice while in the CPs, it means the chemical oxidation or reduction of the polymer chain. Doping in CPs is classified into two types: p-doping and n-doping. The polymer can be p-doped through its oxidation chemically or electrochemically whereas, n-doping results from the reduction of polymer chain through chemical and electrochemical methods. In both the cases, polymer develops an excess positive (p-doped) and negative charge (n-doped) which is neutralized or balanced by the counter anion and cation, respectively. The doping phenomenon can be understood from the equations given below for the p and n-doping of polyacetylene.

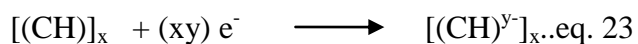
The oxidation of polyacetylene removes the electron from the polymer chain resulting in a net positive charge (eq. 21).



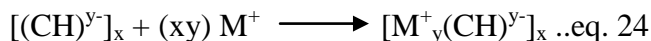
The positive charge is balanced by the counter anions which get associated with the oxidized molecule (eq. 22).



For n-doping, a reducing agent introduces an e^- into the polymer chain causing the net negative charge on the polymer chain.



The negative charge induced by reduction is balanced by the association of cations in the polymer backbone.



Ionization of the polymer chain changes the equilibrium state of the polymer in which HOMO level is shifted upward while the LUMO level shifts down. This change in the position of HOMO and LUMO creates new energy band in the band which is delocalized over the entire polymer chain and results in a charge ‘island.’ The larger the ionization of the polymer chain, the more the islands overlap and delocalize providing it electronic conductivity. The one-dimensionality of the conducting polymer allows for the Jahn-Teller type relaxation called Peirls distortion, resulting in the separation of filled and unfilled portions of the sp^2 band.^{89, 107} High doping level alone does not lead to high conductivity, charge carrier mobility is also highly important for the polymer to exhibit high conductivity. Poor charge mobility can result in the insulating behaviour of polymer and result in inferior electrochemical performance.

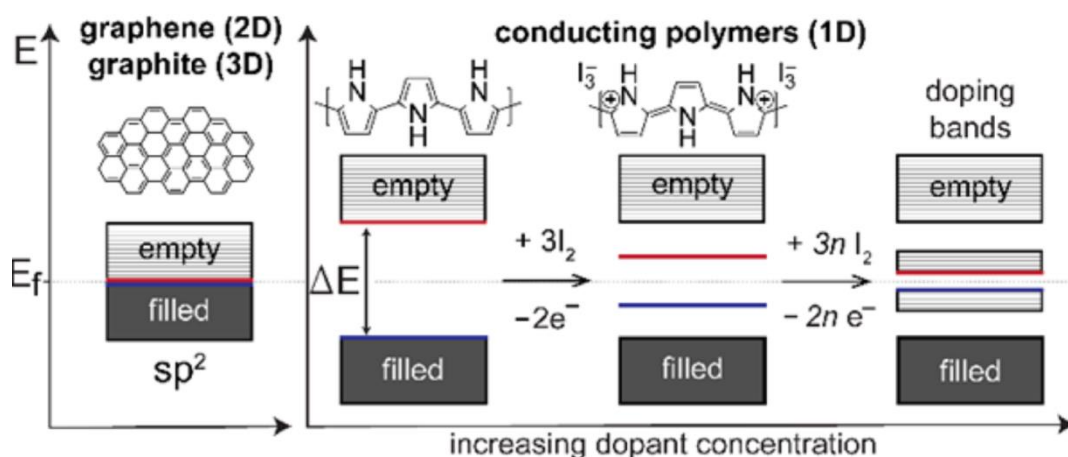


Figure 15. Unlike graphene or graphite, polypyrrole has a distinct band gap leading to its semiconducting nature. In chemical p-doping, two electrons are removed from the chain, creating a carbocation, or bipolaron, balanced by dopant counterions. As the polymer is doped to its saturation limit, more and more bipolaronic states are formed. Their energy bands overlap, creating intermediate band structures which facilitate electronic transport throughout the polymer. (Reproduced with permission from American Chemical Society; *Chem. Mater.* **28**, 17, 5989-5998).

1.2.3.2.4 Issues of Low Capacitance and High Equivalent Series Resistance in Pseudocapacitive Materials- Pseudocapacitive materials have a high theoretical capacitance ranging from 200-3000 $F g^{-1}$, owing to their redox behaviour. Such high capacitance can lead

to high energy density as $E = \frac{1}{2} CV^2$.¹⁰⁸ However, the practical capacitance or the realizable capacitance remains low; this reduced practical capacitance results from low and inefficient electrochemically active surface area (ESA) and high resistance. For the electrochemical systems, the surface accessible to the electrolyte or the surface which participates in the electrochemical process is called electrochemically active surface area. This surface is different from the BET surface area obtained through gas adsorption experiments. Therefore, to obtain maximum performance from the electroactive material, it is indispensable to achieve sizeable electrode-electrolyte interface. In addition to ESA, the ion mobility to the electrode-electrolyte interface is also very important as it defines the rate capability of the device. The strategies that have been developed to increase the surface area of material include reduction of the particle size or creating porosity. Although the surface area is increased following the above-mentioned strategies, it inevitably increases the number of grain boundaries which results in high resistance. Further, the equivalent series resistance, which determines the power capability and electrical losses, is the sum of the resistance of the material, and resistance posed to the movement of electrolyte ion (diffusion). Also, since the electrochemical processes are the surface process occurring only at the electrode-electrolyte interface, the material inaccessible to the electrolyte remains dead which decreases the gravimetric capacitance of pseudocapacitive material. Thus, it is necessary to increase the ESA, improve the electrolyte accessibility and reduce dead volume for increasing or improving the performance of the pseudocapacitive material for the wide-scale applications. A conductive wrapping strategy of graphene MnO₂ composite was demonstrated by Bao et al. by coating the composite with CNT or conducting polymer.¹⁰⁹ The strategy improved the capacitance of composite by 45 %. However, the ESR obtained was high 41 Ω which is detrimental to the rate capability of the composite.

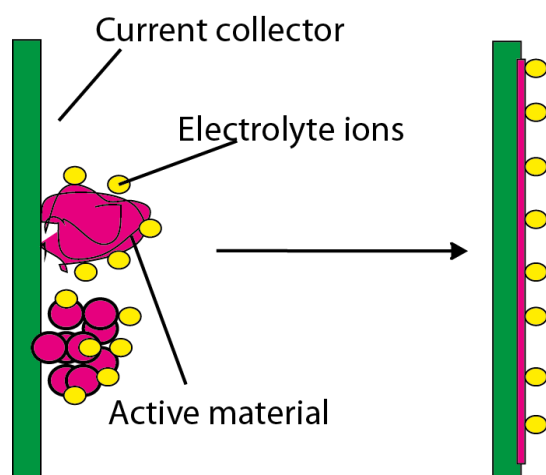


Figure 16. Schematic representation of the concept of performance enhancement through surface alignment of pseudocapacitive material.

A strategy to improve ESA with a simultaneous increase in the conductivity is to provide an arrangement in which a very thin layer of capacitive material is seamlessly supported over a conducting core keeping the density of grain boundaries as low as possible. As can be seen in **Figure 16**, the active material with an uneven shape or in the form of fine particles, only the outer surface is available to the electrolyte. The bulk of the active material remains unutilized and also the inter-particle spaces hinder the charge transport resulting in inferior conductivity. However, if the active material is stretched or structurally aligned in a seamless manner over a current collector, not only the un-used material is minimized but at the same time, grain boundaries and inter-particle spaces are also reduced substantially. In this context, 1D or 2D carbon morphologies can be utilized as conducting core over which even, seamless and smooth deposition of the pseudocapacitive materials like PEDOT, PANI, MnO_2 , etc. will be a viable and effective strategy to achieve high capacitance and rate capability.

1.3 Composites of Pseudocapacitive Materials and Carbon Morphologies- A large number of publications dealing with the synthesis of composites of carbon nanotubes, carbon nanofibers and graphene with metal oxides (MnO_2 , RuO_2 , etc.) and conducting polymers (PEDOT, PANI, polypyrrole) has been reported. The primary end towards synthesizing the composites of pseudocapacitive materials with carbon materials is to tackle the low conductivity, particle agglomeration, and poor cyclic stability. 1D and 2D carbon morphologies have been applied to composite synthesis, each having its advantages. For the synthesis of CP composites, *in-situ*, solution blend method, physical mixing, electrochemical polymerization, etc. have been adopted. Xie *et al.* adopted skeleton/skin strategy where CNT acts as the skeleton and PANI forms the skin. CNT film prepared through chemical vapour deposition was used as a template for the electrodeposition of PANI. The capacitance of the composite was modest at 236 F g^{-1} , a much lower value than the theoretical capacitance. Also, the ESR of the composite electrode was substantially high.¹¹⁰ Sulphonated MWCNT was used as a support material over which PANI was polymerized through chemical oxidation method. The composite showed capacitance of 515.2 F g^{-1} for 76.4 wt% of PANI. Scanning electron microscope images showed thicker PANI deposition; however, the addition of MWCNT improved the cycling to a good degree.¹¹¹ A flexible electrode prepared by the polymerization of PANI on the CNTs in a free-standing buckypaper film was demonstrated by Fan *et al.*, the thickness of PANI deposited on the CNT surface was estimated between 50-

90 nm. The specific capacitance of 360 F g^{-1} could be obtained at a current density of 1 A g^{-1} . However, the ESR was significantly high at 11.1Ω which is undesirable for high-performance supercapacitor.¹¹² Various composites of PEDOT with EDLC material and metal oxide have been prepared; these composites show better performance compared to individual components. In one such report, PEDOT nanowires were electrochemically deposited in the alumina template, it is further decorated with MnO_2 nanoparticles by reduction of KMnO_4 , the composite showed good capacitive behaviour with capacitance of 450 F g^{-1} .¹¹³ For the ESA enhancement of MnO_2 , ultrathin nanofibers of MnO_2 with thickness of $\sim 40 \text{ nm}$ were grown on graphitic hollow carbon spheres and the composite showed good rate capability at 55 % retention at a current density of 15 A g^{-1} .¹¹⁴ Literature on the pseudocapacitive material and their composites reveals that the strategies designed although succeeds in enhancing one or other property, the wholesome improvement is not observed. Thus, a synthesis strategy or material design which improves the rate capability, cycling performance and capacitance is necessary for the far-flung applications of electrochemical capacitors using pseudocapacitive materials.

1.4 Electrochemical Characterization Techniques and Calculations for Supercapacitors

1.4.1 Cyclic Voltammetry

Cyclic voltammetry is one of the most diverse electroanalytical techniques which has been used in a variety of electrochemical analyses encompassing the fields of batteries, capacitors, sensors, corrosion, biochemistry, etc. In this technique, the potential of the working electrode is scanned at a particular scan rate in an electrolyte solution, and the resultant current is measured as a function of potential. It provides information on redox reactions, electron transfer, and surface adsorption of species. Also, the location of the redox potential of electroactive species can be identified using this technique. The current response obtained as a function of potential is called cyclic voltammogram. In the study of a material for supercapacitor application, CV analysis can identify capacitive behaviour. It can also differentiate between pseudocapacitive behaviour, characterized by the appearance of redox current peaks, from EDLC in which CV shows rectangular shape with no redox current. Rate behaviour of a capacitor is also analyzed by running CV at increasing scan rates and plotting obtained peak current as a function of scan rate. Capacitance can be calculated from the CV curve using the equation given below:

$$C = \frac{1}{mV(V_2-V_1)} \int_{V_1}^{V_2} IdV \dots \text{eq. 25}$$

where, m= mass of the active material (g)

V= scan rate (mV s^{-1})

I= current (mA)

V_2-V_1 = potential window

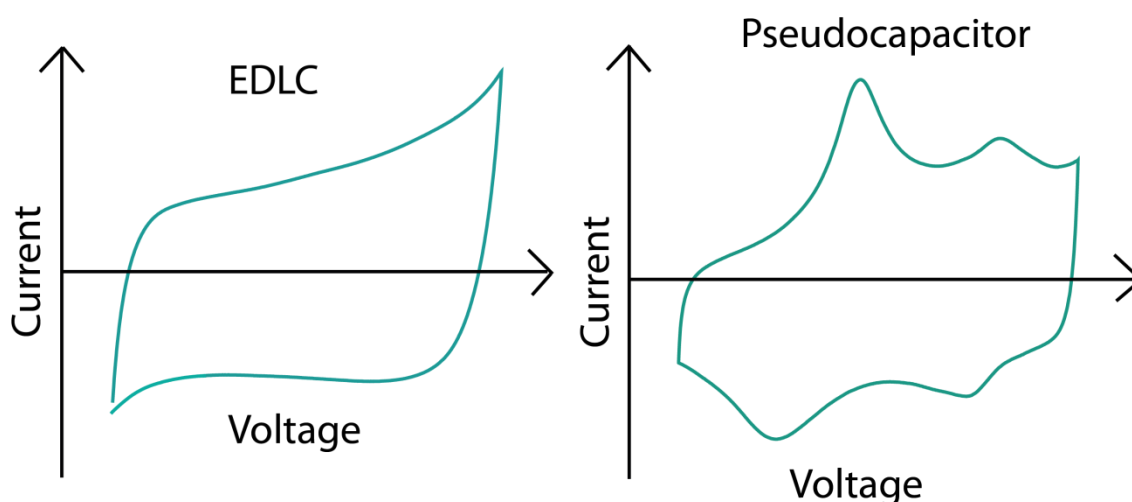


Figure 17. Representation of the differences observed in the CV features of EDLC and pseudocapacitive charge storage.

1.4.2 Galvanostatic Charge-discharge

This measurement is widely used for characterizing charge storage properties of electrochemical devices such as supercapacitors and batteries. In this measurement, capacitor device is charged to a fixed potential by applying a constant current and then discharge to another potential. The GCD curve shows a triangular profile for the EDLC behaviour whereas slight deviation may arise in the GCD of pseudocapacitive materials due to redox reaction. GCD measurements are most reliable and commonly used for the calculation of capacitance, internal resistance and other performance parameters of a supercapacitor.

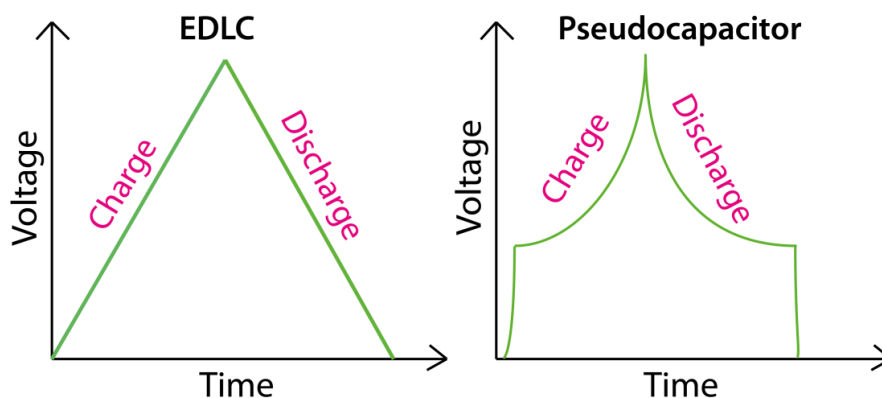


Figure 18. Representation of the typical features of GCD curves for EDLC and pseudocapacitive materials.

1.4.3 Electrochemical Impedance Spectroscopy

Electrochemical Impedance spectroscopy has become one of the most important electrochemical techniques over the years, finding applications in studying internal properties of the electrochemical systems like corrosion, charge-storage devices, electrocatalysis, sensors, biochemistry, etc. EIS measurements are performed by applying an AC potential to the electrochemical cell and recording the corresponding current response of the cell. For supercapacitors, EIS is carried out to understand frequency behavior, measurement of capacitance, finding ESR, charge transfer resistance, studying diffusion properties, etc. In EIS analysis of supercapacitors, the imaginary component of impedance (Z_{Im}) is plotted vs. real component of impedance (Z_{Real}) and the representation is called the Nyquist plot. This plot features an intercept at the high-frequency region which gives the ESR of the device; it is followed by a semi-circle towards the low frequency the region. The diameter of this semi-circle is the measure of charge-transfer resistance. Following the semi-circle is the diffusion region called Warburg impedance, characterized by a horizontal line. A low-frequency vertical line (capacitive region) follows the Warburg impedance. For ideal capacitive behaviour, low-frequency line is vertical parallel to the imaginary axis.

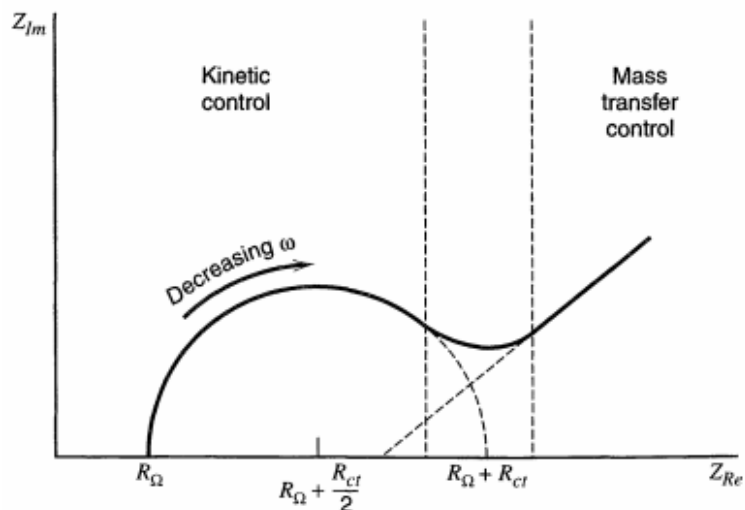


Figure 19. Impedance plot for an electrochemical system. Regions of mass-transfer and kinetic control are found at low and high frequencies, respectively. (Reproduced by permission from John Wiley & Sons; License no. 4331850236708)

1.4.4 Calculations

1.4.4.1 Weight of Material Deposited through Electrodeposition

The amount of material deposited through electrodeposition is calculated by Faraday's equation,

$$W = \frac{M \cdot I \cdot t}{nF} \text{..eq. 26}$$

where, w = weight of material deposited in grams;

M= molecular weight of monomer or metal oxide (g mol^{-1})

I= current applied (A)

t= time period for which the current is passed (s)

n= number of electrons involved in redox reaction

F= 96485 (Faraday constant)

1.4.4.2 Specific Capacitance

The following equation is used for calculating the specific capacitance from galvanostatic charge-discharge curves,

$$C_s = \frac{I \times \Delta t \times 2}{\Delta V} \text{ F g}^{-1} \text{..eq. 27}$$

Where, 'I' is the current density (A g^{-1}),

' Δt ' is the discharge time,

' ΔV ' is the potential window.

The equation has been multiplied by 2 for obtaining capacitance of the single electrode (or material).

1.4.4.3 Volumetric Capacitance,

$$C_v = \frac{I \times \Delta t}{\Delta V \times v} \text{ F cm}^{-3} \text{..eq. 28}$$

Here, 'v' is the volume of the device in cm^3 .

1.4.4.4 Areal Capacitance,

$$C_A = \frac{I \times \Delta t \times 2}{\Delta V \times A} \text{ F cm}^{-2} \text{..eq. 29}$$

Here, 'A' is the area of the electrode in cm^2 .

1.4.4.5 Volumetric Energy Density,

$$E_v = \frac{C_v \Delta V^2}{2} \text{ Wh cm}^{-3} \text{..eq. 30}$$

1.4.4.6 Volumetric Power Density

$$P_v = \frac{E_v}{\Delta t} \text{ W cm}^{-3} \text{..eq. 31}$$

1.4.4.7 Maximum Volumetric Power Density,

$$P_m = \frac{\Delta V^2}{4R \times v} \text{ W cm}^{-3} \text{..eq. 32}$$

1.4.4.8 Specific Energy Density,

$$E_d = \frac{C\Delta V^2}{2} \text{ Wh kg}^{-1} \text{..eq. 33}$$

Here, C is the specific capacitance of the device.

1.4.4.9 Specific Power Density,

$$P_d = \frac{E_d}{\Delta t} \text{ W kg}^{-1} \text{..eq. 34}$$

1.5 Scope and Objectives of the Current Thesis- Analysis of the literature on the pseudocapacitive materials, conducting polymers and metal oxides, unveils the issues of low practical capacitance, high equivalent series resistance, low rate capability and durability which have marred application of these materials in commercial devices. The designs of the devices, material properties, electrode-electrolyte interaction are the parameters that define the overall performance. Fundamental understanding of the charge-storage in the pseudocapacitive material has shown the importance of the electrochemically active surface area and the electrolyte accessibility along with high conductivity, necessary for fast redox kinetics. Furthermore, the conventional supercapacitor designs, which employ liquid electrolyte, are not adequate to meet the safety and economic aspects. Moreover, they are bulky and heavy which result in low specific capacitance and energy density. Solid supercapacitors, in contrast to the conventional devices, are lightweight, thin, flexible, cost-effective and safer. However, the low ionic conductivity of solid, semi-solid or gel electrolytes than the liquid counterparts used in the solid electrochemical capacitors is a pertaining issue. Given this limitation, it is utmost necessary to increase the electrochemically active surface area and accessibility of the electrolyte to the active material for achieving large electrode-electrolyte interface. Therefore, the advancement and improvements in the material properties are needed for the full-fledged development of the solid devices. The principal focus of this thesis is to develop strategies to address the issues like low electrochemically active surface area and inferior practical performance of the pseudocapacitive materials. Towards this end, structural alignment of the pseudocapacitive materials on the carbon morphologies in a uniform and seamless manner is proposed. Carbon morphologies like CNT, CNF, and graphene are used as the scaffolds which perform the dual function of mechanical support and current collection. Conducting polymers and metal oxides in a uniform seamless manner are deposited over the surface of carbon morphologies. To achieve this design, the thesis begins (**Chapter-2**) with the 1D alignment of PEDOT on the

CNTs in the entangled free-standing flexible film called Buckypaper. This is accomplished by confining the polymerization to the surface through interfacial polymerization. In the next work (**Chapter 3**), the thickness of the PEDOT deposited on the CNTs is further reduced by carrying out an oxidant-free hydrothermal synthesis. Then the attention moves towards another conducting polymer, polyaniline (**Chapter 4**). In this case, near theoretical capacitance is achieved by manipulating the hydrophilicity of PANI to enhance the wettability along with uniform deposition of PANI in a free-standing carbon fiber network. Finally, the concept of structural alignment is applied to MnO_2 , where, a highly conducting low-cost and flexible substrate is derived from Grafoil sheet and scotch tape which is further modified electrochemically over which thin fibers of MnO_2 are electrodeposited (**Chapter 5**).

The key objectives of this treatise are listed below:

1. The primary aim of this thesis is to achieve high electrochemically active surface area in redox capacitive materials by replacing their dead volume with carbon morphologies to provide mechanical support and charge conduction.
2. Structural alignment of the active pseudocapacitive materials in seamless and uniform fashion over suitable carbon morphologies to reduce grain boundaries for achieving both high conductivity and rate capability.
3. Improving the wettability of the active materials towards gel electrolyte to achieve high electrode-electrolyte interface.
4. To study the effect of electrodeposition parameters on the morphology and capacitive properties of the conducting polymers and metal oxides.
5. Developing simple, efficient and scalable strategies to achieve surface confined growth and deposition of active materials through surfactant-free polymerization techniques.
6. Application of a shear thinning gel electrolyte to attain better infiltration and impregnation in the cases where the material surface is hydrophobic.
7. To study the effect of modification of the scaffold surfaces on the properties of deposited redox materials towards the capacitance and device performance.
8. Electrochemical treatment of carbon morphologies and its effect on the morphology and surface properties, and its subsequent impact on the supercapacitor performance.
9. Development of highly conducting free-standing flexible substrates for the application as a scaffold material in the flexible solid supercapacitors.

10. Achieving near theoretical capacitances in the pseudocapacitive materials without compromising on the power density and rate capability of the device.

1.6 References

1. T. F. Stocker, D. Qin, G.-K. Plattner, L.V. Alexander, S.K. Allen, N.L. Bindoff, F.-M. Bréon, J.A. Church, U. Cubasch, S. Emori, P. Forster, P. Friedlingstein, N. Gillett, J.M. Gregory, D.L. Hartmann, E. Jansen, B. Kirtman, R. Knutti, K. Krishna Kumar, P. Lemke, J. Marotzke, V. Masson-Delmotte, G.A. Meehl, I.I. Mokhov, S. Piao, V. Ramaswamy, D. Randall, M. Rhein, M. Rojas, C. Sabine, D. Shindell, L.D. Talley, D.G. Vaughan and S.-P. Xie, *Cambridge University Press, Cambridge, United Kingdom and New York, NY, USA*, 2013.
2. L. R. F. A. J. Bard, *Electrochemical methods: Fundamentals and applications*, 2001.
3. H. Ji, X. Zhao, Z. Qiao, J. Jung, Y. Zhu, Y. Lu, L. L. Zhang, A. H. MacDonald and R. S. Ruoff, *Nat. Commun.*, 2014, **5**, 3317.
4. L. L. Zhang, X. Zhao, H. Ji, M. D. Stoller, L. Lai, S. Murali, S. McDonnell, B. Cleveger, R. M. Wallace and R. S. Ruoff, *Energy Environ. Sci.*, 2012, vol. 5, p. 9618.
5. H. Helmholtz, *Annalen der Physik*, 1853, **165**, 211-233.
6. H. H. a. W. Abhandl, *Physic. Tech. Reichsanst Alt.*, 1879, **1**, 925.
7. A. Gouy, *Ann. Chin. Phys.*, 1903, **29**, 145.
8. D. L. Chapman, *Phil. Mag.*, 1913, **25**, 475.
9. O. Stern, *Z. Electrochem.*, 1924, **30**, 508.
10. O. A. E. a. B. F. Markov, *Zh. Fiz. Khim.*, 1939, **13**, 318.
11. D. C. Grahame, *J. Electrochem. Soc.*, 1951, **98**, 313.
12. M. A. V. Devanathan, *Trans. Faraday Soc.*, 1954, **50**, 373.
13. M. A. V. D. a. K. M. J. O'M Bockris, *Pro. Ray. Soc., Ser. A.*, 1963, **274**, 55.
14. H. S. Williams.
15. J. F. Keithley, 1999, **John Wiley & Sons.**, 23.
16. B. E. Conway, *Springer*, 1999.
17. A. G. Pandolfo and A. F. Hollenkamp, *Journal of Power Sources*, 2006, **157**, 11-27.
18. S. Luryi, *Appl. Phys. Lett.*, 1988, **52**, 501-503.
19. L. Radhakrishnan, J. Reboul, S. Furukawa, P. Srinivasu, S. Kitagawa and Y. Yamauchi, *Chem. Mater.*, 2011, **23**, 1225-1231.
20. J. Chmiola, G. Yushin, Y. Gogotsi, C. Portet, P. Simon and P. L. Taberna, *Science*, 2006, **313**, 1760-1763.
21. D. P. S. D. Das, and B. C. Meikap, *J Chem Eng Process Technol*, 2015, **6**, 248.
22. M. Fujishige, I. Yoshida, Y. Toya, Y. Banba, K.-i. Oshida, Y.-s. Tanaka, P. Dulyaseree, W. Wongwiriyanpan and K. Takeuchi, *Journal of Environmental Chemical Engineering*, 2017, **5**, 1801-1808.
23. Y. T. Y. Uraki, M Ogawa, S. Gaman and S. Tokura, *BioResources*, 2009, **4**, 205-213.
24. D. L. a. X.-J. Ma, *Cellulose*, 2013, **20**, 1649-1656.
25. C. N. a. K. Kadirvelu, *Bioresource Technology*, 1997, **62**, 123-127.
26. M. V. Navarro, R. Murillo, J. M. López, T. García, M. S. Callén and A. M. Mastral, *Energy & Fuels*, 2006, **20**, 2627-2631.
27. H. Teng, T.-S. Yeh and L.-Y. Hsu, *Carbon*, 1998, **36**, 1387-1395.
28. E. Vilaplana-Ortego, M. A. Lillo-Ródenas, J. Alcañiz-Monge, D. Cazorla-Amorós and A. Linares-Solano, *Carbon*, 2009, **47**, 2141-2142.
29. H. Demiral, İ. Demiral, B. Karabacakoglu and F. Tımsek, *Chemical Engineering Research and Design*, 2011, **89**, 206-213.
30. J. i. Hayashi, A. Kazehaya, K. Muroyama and A. P. Watkinson, *Carbon*, 2000, **38**, 1873-1878.
31. X. Lin, H. Lou, W. Lu, F. Xu, R. Fu and D. Wu, *Chinese Chemical Letters*, 2018, **29**, 633-636.

32. P. Suktha, P. Chiochan, P. Iamprasertkun, J. Wutthiprom, N. Phattharasupakun, M. Suksomboon, T. Kaewsongpol, P. Sirisinudomkit, T. Pettong and M. Sawangphruk, *Electrochimica Acta*, 2015, **176**, 504-513.
33. X. Chen, J. Zhang, B. Zhang, S. Dong, X. Guo, X. Mu and B. Fei, *Scientific Reports*, 2017, **7**, 7362.
34. L. F. Chen, Z. H. Huang, H. W. Liang, H. L. Gao and S. H. Yu, *Advanced Functional Materials*, 2014, **24**, 5104-5111.
35. J. P. Paraknowitsch and A. Thomas, *Energy & Environmental Science*, 2013, **6**, 2839-2855.
36. S. Iijima, *Nature*, 1991, **354**, 56.
37. T. Filleter, R. Bernal, S. Li and H. D. Espinosa, *Advanced Materials*, 2011, **23**, 2855-2860.
38. Q. W. Li, Y. Li, X. F. Zhang, S. B. Chikkannanavar, Y. H. Zhao, A. M. Dangelewicz, L. X. Zheng, S. K. Doorn, Q. X. Jia, D. E. Peterson, P. N. Arendt and Y. T. Zhu, *Advanced Materials*, 2007, **19**, 3358-3363.
39. T. Ando, H. Matsumura and T. Nakanishi, *Physica B: Condensed Matter*, 2002, **323**, 44-50.
40. A. Peigney, C. Laurent, E. Flahaut, R. R. Bacsa and A. Rousset, *Carbon*, 2001, **39**, 507-514.
41. C. Niu, E. K. Sichel, R. Hoch, D. Moy and H. Tennent, *Applied Physics Letters*, 1997, **70**, 1480-1482.
42. *IUPAC Recommendations 1995*, **67**.
43. K. S. Novoselov, A. K. Geim, S. V. Morozov, D. Jiang, Y. Zhang, S. V. Dubonos, I. V. Grigorieva and A. A. Firsov, *Science*, 2004, **306**, 666-669.
44. F. Bonaccorso, A. Lombardo, T. Hasan, Z. Sun, L. Colombo and A. C. Ferrari, *Materials Today*, 2012, **15**, 564-589.
45. J.-H. Chen, C. Jang, S. Xiao, M. Ishigami and M. S. Fuhrer, *Nature Nanotechnology*, 2008, **3**, 206.
46. D. C. Marcano, D. V. Kosynkin, J. M. Berlin, A. Sinitskii, Z. Sun, A. Slesarev, L. B. Alemany, W. Lu and J. M. Tour, *ACS Nano*, 2010, **4**, 4806-4814.
47. J. Wang, K. K. Manga, Q. Bao and K. P. Loh, *Journal of the American Chemical Society*, 2011, **133**, 8888-8891.
48. R. S. Dey, H. A. Hjuler and Q. Chi, *Journal of Materials Chemistry A*, 2015, **3**, 6324-6329.
49. S. R. C. Vivekchand, C. S. Rout, K. S. Subrahmanyam, A. Govindaraj and C. N. R. Rao, *Journal of Chemical Sciences*, 2008, **120**, 9-13.
50. M. D. Stoller, S. Park, Y. Zhu, J. An and R. S. Ruoff, *Nano Letters*, 2008, **8**, 3498-3502.
51. X. Wang, G. Sun, P. Routh, D.-H. Kim, W. Huang and P. Chen, *Chemical Society Reviews*, 2014, **43**, 7067-7098.
52. L. L. Zhang, X. Zhao, H. Ji, M. D. Stoller, L. Lai, S. Murali, S. McDonnell, B. Cleveger, R. M. Wallace and R. S. Ruoff, *Energy & Environmental Science*, 2012, **5**, 9618.
53. T. V. H. a. C. R. Chambers, *Manufacture of Carbon Filaments*, 1889, **U.S. Patent 405,480**.
54. B. Zhang, F. Kang, J.-M. Tarascon and J.-K. Kim, *Progress in Materials Science*, 2016, **76**, 319-380.
55. K. P. De Jong and J. W. Geus, *Catalysis Reviews*, 2000, **42**, 481-510.
56. L. Zhang, A. Aboagye, A. Kelkar, C. Lai and H. Fong, *Journal of Materials Science*, 2014, **49**, 463-480.
57. J. S. Bonso, G. D. Kalaw and J. P. Ferraris, *Journal of Materials Chemistry A*, 2014, **2**, 418-424.
58. C. Kim, B. T. N. Ngoc, K. S. Yang, M. Kojima, Y. A. Kim, Y. J. Kim, M. Endo and S. C. Yang, *Advanced Materials*, 2007, **19**, 2341-2346.
59. D. G. Lee and B.-H. Kim, *Synthetic Metals*, 2016, **219**, 115-123.
60. A. K. Cuentas Gallegos and M. E. Rincón, *Journal of Power Sources*, 2006, **162**, 743-747.
61. E. J. Ra, E. Raymundo-Piñero, Y. H. Lee and F. Béguin, *Carbon*, 2009, **47**, 2984-2992.
62. L.-F. Chen, Z.-H. Huang, H.-W. Liang, W.-T. Yao, Z.-Y. Yu and S.-H. Yu, *Energy & Environmental Science*, 2013, **6**, 3331-3338.
63. M. Yudasaka, S. Iijima and V. H. Crespi, in *Carbon Nanotubes: Advanced Topics in the Synthesis, Structure, Properties and Applications*, eds. A. Jorio, G. Dresselhaus and M. S. Dresselhaus, Springer Berlin Heidelberg, Berlin, Heidelberg, 2008, pp. 605-629.

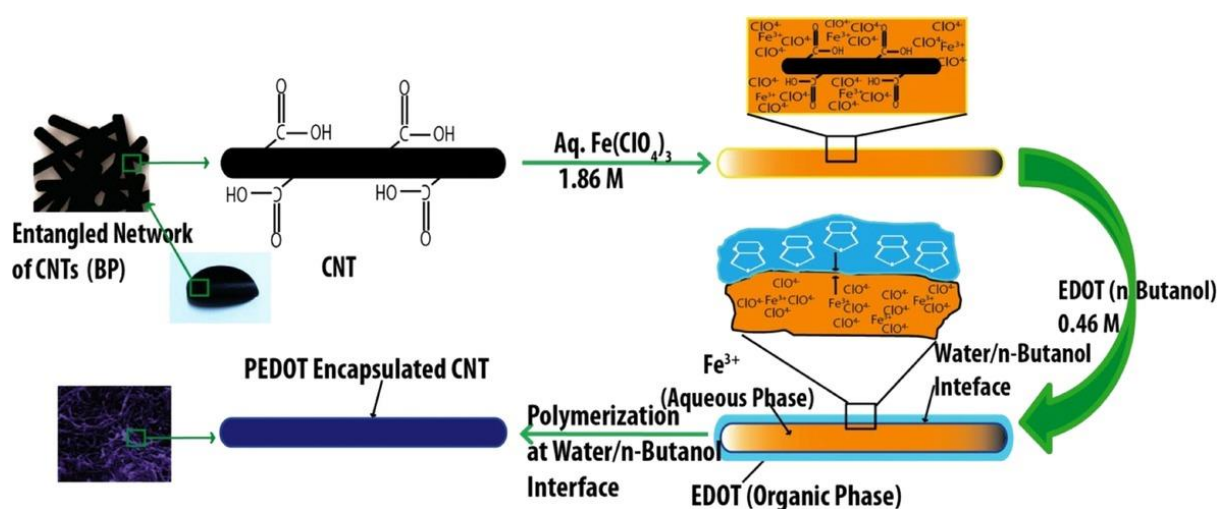
64. G. Pagona, G. Mountrichas, G. Rotas, N. Karousis, S. Pispas and N. Tagmatarchis, *Properties, applications and functionalisation of carbon nanohorns*, 2009.
65. S. Iijima, M. Yudasaka, R. Yamada, S. Bandow, K. Suenaga, F. Kokai and K. Takahashi, *Chemical Physics Letters*, 1999, **309**, 165-170.
66. C.-M. Yang, Y.-J. Kim, M. Endo, H. Kanoh, M. Yudasaka, S. Iijima and K. Kaneko, *Journal of the American Chemical Society*, 2007, **129**, 20-21.
67. A. Izadi-Najafabadi, T. Yamada, D. N. Futaba, M. Yudasaka, H. Takagi, H. Hatori, S. Iijima and K. Hata, *ACS Nano*, 2011, **5**, 811-819.
68. B. E. Conway, *Springer*, 1999, **Chapter 10**, 221-257.
69. A. D. Graves and D. Inman, *Nature*, 1965, **208**, 481.
70. B. E. Conway and W. G. Pell, *Journal of Solid State Electrochemistry*, 2003, **7**, 637-644.
71. B. E. Conway, *Electrochimica Acta*, 1993, **38**, 1249-1258.
72. M. Y. Ho, P. S. Khiew, D. Isa, T. K. Tan, W. S. Chiu and C. H. Chia, *Nano*, 2014, **09**, 1430002.
73. S. T. a. G. Buzzanca, *J. Electroanal. Chem.*, 1971, **29**, 1-5.
74. W. Sugimoto, H. Iwata, K. Yokoshima, Y. Murakami and Y. Takasu, *The Journal of Physical Chemistry B*, 2005, **109**, 7330-7338.
75. W. C. a. K. C. C. Hu, *J. Electrochem. Soc.*, 2004, **151**, A281-A290.
76. S.-L. Chou, J.-Z. Wang, S.-Y. Chew, H.-K. Liu and S.-X. Dou, *Electrochemistry Communications*, 2008, **10**, 1724-1727.
77. V. Subramanian, H. Zhu, R. Vajtai, P. M. Ajayan and B. Wei, *The Journal of Physical Chemistry B*, 2005, **109**, 20207-20214.
78. Y. Luo, *Materials Letters*, 2007, **61**, 1893-1895.
79. S. W. Donne, A. F. Hollenkamp and B. C. Jones, *Journal of Power Sources*, 2010, **195**, 367-373.
80. S. W. Zhang and G. Z. Chen, *Energy Materials*, 2008, **3**, 186-200.
81. H. Y. Lee and J. B. Goodenough, *Journal of Solid State Chemistry*, 1999, **144**, 220-223.
82. M. Toupin, T. Brousse and D. Bélanger, *Chemistry of Materials*, 2004, **16**, 3184-3190.
83. T. B. a. J. W. L. D. Belanger, *Manganese Oxides: Battery Materials Make the Leap to Electrochemical Capacitors*, 2008, **The Electrochemical Society Interface** 49-52.
84. C. Yuan, X. Zhang, L. Su, B. Gao and L. Shen, *Journal of Materials Chemistry*, 2009, **19**, 5772-5777.
85. F. Zhang, C. Yuan, X. Lu, L. Zhang, Q. Che and X. Zhang, *Journal of Power Sources*, 2012, **203**, 250-256.
86. H. Letheby, *Journal of the Chemical Society*, 1862, **15**, 161-163.
87. H. Shirakawa, E. J. Louis, A. G. MacDiarmid, C. K. Chiang and A. J. Heeger, *Journal of the Chemical Society, Chemical Communications*, 1977, 578-580.
88. J. T. a. A. Takahashi, *Synthetic Metals*, 1991, **41**, 7-12.
89. A. M. Bryan, L. M. Santino, Y. Lu, S. Acharya and J. M. D'Arcy, *Chemistry of Materials*, 2016, **28**, 5989-5998.
90. G. Inzelt, in *Conducting Polymers: A New Era in Electrochemistry*, Springer Berlin Heidelberg, Berlin, Heidelberg, 2012, pp. 149-171.
91. B. Anothumakkool, S. N. Bhange, S. M. Unni and S. Kurungot, *RSC Advances*, 2013, **3**, 11877.
92. B. Anothumakkool, R. Soni, S. N. Bhange and S. Kurungot, *Energy & Environmental Science*, 2015, **8**, 1339-1347.
93. N. Paradee and A. Sirivat, *Polymer International*, 2014, **63**, 106-113.
94. M. Granström and O. Inganäs, *Polymer*, 1995, **36**, 2867-2872.
95. T. Y. Kim, J. E. Kim and K. S. Suh, *Polymer International*, 2006, **55**, 80-86.
96. Y. Wang, *Journal of Physics: Conference Series*, 2009, **152**, 012023.
97. K. Lota, V. Khomeenko and E. Frackowiak, *Journal of Physics and Chemistry of Solids*, 2004, **65**, 295-301.
98. Z. Boeva and V. Sergeev, *Polyaniline: Synthesis, Properties, and Application*, 2014.
99. J. Luo, S. Jiang, R. Liu, Y. Zhang and X. Liu, *Electrochimica Acta*, 2013, **96**, 103-109.
100. K. Lee, S. Cho, S. H. Park, A. J. Heeger, C. W. Lee and S. H. Lee, *Nature*, 2006, **441**, 65-68.

101. H. Li, J. Wang, Q. Chu, Z. Wang, F. Zhang and S. Wang, *Journal of Power Sources*, 2009, **190**, 578-586.
102. D.-W. Wang, F. Li, J. Zhao, W. Ren, Z.-G. Chen, J. Tan, Z.-S. Wu, I. Gentle, G. Q. Lu and H.-M. Cheng, *ACS Nano*, 2009, **3**, 1745-1752.
103. L. Pan, G. Yu, D. Zhai, H. R. Lee, W. Zhao, N. Liu, H. Wang, B. C.-K. Tee, Y. Shi, Y. Cui and Z. Bao, *Proceedings of the National Academy of Sciences*, 2012, **109**, 9287-9292.
104. A. G. MacDiarmid, R. J. Mammone, R. B. Kaner, S. J. Porter, R. Pethig, A. J. Heeger and D. R. Rosseinsky, *Philosophical Transactions of the Royal Society A: Mathematical, Physical and Engineering Sciences*, 1985, **314**, 3-15.
105. S. Quillard, G. Louarn, S. Lefrant and A. G. Macdiarmid, *Physical Review B*, 1994, **50**, 12496-12508.
106. G. Inzelt, in *Conducting Polymers: A New Era in Electrochemistry*, Springer Berlin Heidelberg, Berlin, Heidelberg, 2012, pp. 191-244.
107. G. R. Mitchell, F. J. Davis and C. H. Legge, *Synthetic Metals*, 1988, **26**, 247-257.
108. P. Simon and Y. Gogotsi, *Nature Materials*, 2008, **7**, 845.
109. G. Yu, L. Hu, N. Liu, H. Wang, M. Vosgueritchian, Y. Yang, Y. Cui and Z. Bao, *Nano Letters*, 2011, **11**, 4438-4442.
110. Z. Niu, P. Luan, Q. Shao, H. Dong, J. Li, J. Chen, D. Zhao, L. Cai, W. Zhou, X. Chen and S. Xie, *Energy & Environmental Science*, 2012, **5**, 8726-8733.
111. Z.-z. Zhu, G.-c. Wang, M.-q. Sun, X.-w. Li and C.-z. Li, *Electrochimica Acta*, 2011, **56**, 1366-1372.
112. C. Meng, C. Liu, L. Chen, C. Hu and S. Fan, *Nano Letters*, 2010, **10**, 4025-4031.
113. R. Liu, J. Duay and S. B. Lee, *ACS Nano*, 2010, **4**, 4299-4307.
114. Z. Lei, J. Zhang and X. S. Zhao, *Journal of Materials Chemistry*, 2012, **22**, 153-160.

Chapter-2

1D Alignment of PEDOT on CNTs through Interfacial Polymerization towards High Conductivity and Low Equivalent Series Resistance

In this chapter, a highly conducting phase of PEDOT has been attained over the surface of CNTs in the buckypaper through interfacial polymerization, where the polymerization was confined at the interface of two immiscible liquids. Here, the hydrophilic interaction between the functionalized CNTs and the oxidizing agent (iron perchlorate, $\text{Fe}(\text{ClO}_4)_3$) present in the aqueous phase along with the restricted interaction of the oxidizing agent with the monomer (ethylenedioxythiophene) in the organic layer at the immiscible interface is playing a vital



role to establish a uniform and aggregate-free growth pattern of PEDOT on CNT. By carefully optimizing the amount of polymer in the paper, an electrode with a sheet resistance of $3.4 \Omega \square^{-1}$ and equivalent series resistance of 0.95Ω could be prepared. The power density and energy density of the electrode are 9.94 W cm^{-3} and 8.85 mW cm^{-3} , respectively. The device also delivered a high volumetric capacitance of 18 F cm^{-3} and areal capacitance of 354 mF cm^{-2} .

Content of this chapter is published in the following article:

ChemElectroChem, 2016, 3, 1329-1336.

(<https://onlinelibrary.wiley.com/doi/10.1002/celec.201600229>)

Reproduced by permission of ChemElectroChem, Wiley Online Library

2.1 Introduction

Polyethylenedioxythiophene (PEDOT) has emerged as an attractive candidate to make the electrodes for supercapacitors due to features like moderate capacitance (210 F g^{-1}), wide operable potential window (1.2 V), good stability and high electrical conductivity ($300\text{-}550 \text{ S cm}^{-1}$).¹ However, low areal capacitance and high ESR in the PEDOT-based solid supercapacitors are daunting its utilization in the solid flexible supercapacitors.^{2, 3} Also, the monomer EDOT from which PEDOT is prepared is expensive; therefore, to make the devices using PEDOT affordable, it is necessary to reduce the dead volume of PEDOT. As only the surface of PEDOT takes part in charge storage and the inner core mainly acts as a scaffold and helps to transport electrons, it will be an intelligent thing to replace the core of the PEDOT with some other less expensive conducting materials. Among the carbon morphologies, carbon nanotubes (CNTs) possess high aspect ratio, high surface area and good conductivity. Also, they are commercially readily available. These entire features make CNT an ideal material to choose as a conducting core of PEDOT. Moreover, to obtain maximum power density and rate capability, the resistance of the electrode should be kept as low as possible. For realizing this, the grain boundaries and inter-particle distance should be kept to a minimum level.

Buckypaper (BP), which is a self-standing film of CNTs, exhibits very good flexibility and mechanical strength along with high conductivity and porosity.⁴ Therefore, establishing an aligned growth of PEDOT along the surface of the CNT units in the porous structure of BP will be an efficacious strategy by which the desirable features of the two attractive materials can be integrated to overcome the pertinent issues related to flexibility, thickness and energy density in a supercapacitor. The literature deals with various types of conducting polymer-CNT composite papers; however, most of them suffer from the issues like high internal resistance and low operable potential window.^{5,6}

This chapter is focused on tackling some of these issues. A BP-based device could be prepared by establishing surface-aligned growth of PEDOT on the surface of CNTs and also by carefully extending the electrode/electrolyte interface in the electrode matrix with the help of a poly(vinyl alcohol)/lithium chloride (PVA-LiCl) gel electrolyte.⁷ The gel electrolyte, unlike a solid film electrolyte, infiltrates the matrix and helps to effectively establish the electrode/electrolyte interface. The BP/PEDOT/gel electrolyte combination in the present study has a very low device impedance of 0.95Ω .

2.2 Experimental Section

2.2.1 Materials

Multi-walled carbon nanotubes (MWCNT) were purchased from Nanocyl Inc. 3,4 Ethylenedioxythiophene (EDOT) and iron perchlorate $[\text{Fe}(\text{ClO}_4)_3]$ were bought from Sigma-Aldrich whereas n-butanol and lithium chloride (LiCl) were procured from Thomas-Baker. Polyvinyl alcohol (PVA) ($\text{MW } 115\,000 \text{ g mol}^{-1}$) was purchased from LobaChemie. Sulphuric acid (H_2SO_4) and nitric acid (HNO_3) were supplied by Rankem Chemicals.

2.2.2 Functionalization of Carbon Nanotube (CNT)

400 mg of pristine MWCNT was sonicated in 36 ml nitrating mixture containing concentrated sulphuric acid and nitric acid (3:1). This mixture was sonicated for 4 h. The mixture was then diluted with de-ionised water, washed several times until the pH becomes neutral and filtered. Functionalization was confirmed by ascertaining carbonyl and hydroxyl stretching frequencies of the carboxylic group from the infra-red spectra, the IR data is given in Figure 1.

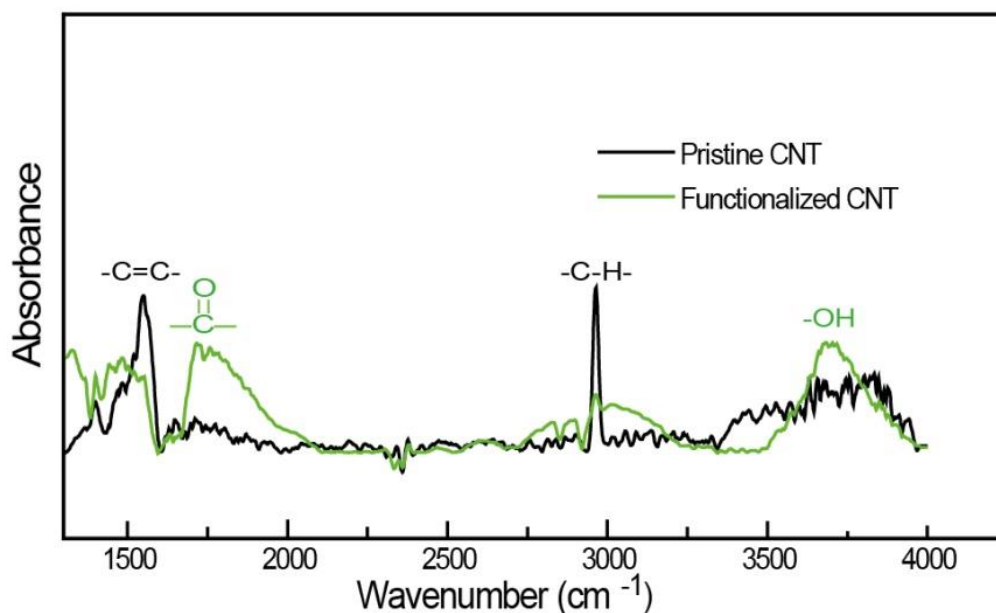


Figure 1. Infra-red spectra of the pristine CNT and functionalized CNT.

2.2.3 Preparation of Buckypaper (BP)

BP was synthesized by following a reported method with some modifications.⁸ In a typical BP synthesis, 35 mg of the acid functionalized MWCNT was mixed in de-ionized water (200 ml) and the mixture was ultrasonicated for 1 h. Subsequently, the suspension was filtered through a PTFE membrane filter paper (0.45 micron pore size) using vacuum at a pressure of 0.25 metric ton. The CNT film deposited on the filter paper was then allowed to dry under ambient

conditions for 12 h. After drying, the CNT film-coated filter paper was pressed at a temperature of 70°C for 5 min using a hot-press at a pressure of one ton. No surfactant or binder was used during the BP synthesis, which relieves the system from the problems of surfactant washing and associated adverse effects of the contamination of the system by traces of the binder. BP is obtained by carefully peeling out the CNT film from the filter paper. However, the fabrication of the hybrid electrode with PEDOT was done before peeling off the CNT layer from the filter paper and the details are given in the following section.

2.2.4 Preparation of PEDOT Modified Buckypaper (PEDOT-BP)

To make PEDOT-BP, a bar coating method was employed using a K-Coater (a multi-coater procured from RK Print Coater, UK) for forming a thin layer of PEDOT. An interfacial polymerization process has been adopted in the present work to establish a surface aligned growth pattern of a thin layer of PEDOT on the surface of the individual MWCNTs in the BP. Briefly, unpeeled CNT film on the PTFE paper was placed on the coater and 250 µl of 1.84 M $\text{Fe}(\text{ClO}_4)_3$ solution in water was coated and the surface was allowed to dry in air. Subsequently, 250 µl of 0.46 M EDOT solution in n-butanol was coated and dried in the same way as the $\text{Fe}(\text{ClO}_4)_3$ coating was done. In this procedure, it should be noted that water and n-butanol are immiscible, and, this results in the formation of an interface. This interface formation plays a crucial role in restricting the polymerization essentially at the interface, leading to the formation of a thin and surface aligned growth of PEDOT along the surfaces of the CNTs in BP. Also, due to the low solubility of $\text{Fe}(\text{ClO}_4)_3$ in n-butanol and EDOT in water, probability of bulk polymerization is relatively low. The PTFE paper with the PEDOT grown CNT layer was then washed with ethanol until all the unused oxidizing agent is washed off. The same procedure was repeated three times to achieve a different polymer thickness and sheet resistance. The PTFE paper having the PEDOT grown CNT film was pressed at a temperature of 70°C for 5 min using a hot-press at a pressure of one ton and the CNT layer was peeled off from the filter membrane to obtain the free-standing PEDOT modified BP. Optimal properties were obtained for the BP with two coatings of the polymer. The corresponding sample is named as BP-2C and was directly taken for device fabrication, where the integer 2 represents the two coatings of PEDOT. The ratio between the oxidizing agent and the monomer was maintained at 4:1, which was found to be the optimized composition for attaining high conductivity.

2.2.5 Characterization

Quanta scanning electron microscope (SEM) and Nova Nano SEM 450 were used to analyze the surface morphology of the polymer modified BP. Transmission electron microscopy (TEM) was performed on a Tecnai-T20 at an accelerated voltage of 200 kV. X-ray diffraction (XRD) patterns were recorded on a RigakuSmartLab diffractometer for Cu K α radiation ($\lambda=1.5406 \text{ \AA}$) at a scan rate of 2° min^{-1} . A Bio-Logic SP-300 PG Stat was used for conducting the electrochemical analyses including cyclic voltammetry (CV), impedance and galvanostatic charge-discharge measurements. Electrochemical data was analyzed by EC-Lab software V10.19. Sheet resistance measurements were done using a four-probe conductivity meter having a probe spacing of 0.2 mm, whereas, the conductivity changes under flexible conditions were measured by I-V polarization). All the characterizations stated below were exclusively done on the PEDOT modified BP (BP-2C) without using any conducting substrate.

2.3 Result and Discussion

2.3.1 Interfacial Polymerization

For the confinement of PEDOT growth exclusively on the CNTs in the buckypaper (BP), the polymerization of EDOT is restricted at the aqueous/organic interface. Oxidising agent $\text{Fe}(\text{ClO}_4)_3$ is present in the aqueous phase which is uniformly coated on the CNTs through bar coating. The interaction of water with the functional groups incorporated on the surface of CNTs through functionalization ensures the confinement of oxidising agent on the outer surface of CNTs. On the other hand, EDOT is mixed in n-butanol and it is immiscible with water. A thin layer of EDOT-n-butanol solution is coated in a similar manner, which forms an immiscible organic phase layer above the aqueous phase. This arrangement ensures growth of PEDOT only on the periphery through slow diffusion of the reactant at the interface. Prevention of the bulk polymerization of PEDOT in the vacant space available in BP thus ensures preservation of adequate porosity in the system all the while maintaining high active surface area through the interconnected and 1-D aligned polymer network. Good porosity in the electrode helps in easy penetration of ions, which is a key parameter in achieving low charge transfer resistance during the charge-discharge process of the device. This, along with the high available surface area of the electroactive layer, makes the system technically ideal to get enhanced capacitance and its retention under different dragging conditions.

2.3.2 SEM and TEM analysis

The field-emission (FE) SEM images in [Figure 2a](#) show the presence of randomly oriented intertwined CNTs forming a porous network. After EDOT polymerization, the porous network was found to be intact, as can be seen in the FESEM image of BP-2C in [Figure 2b](#). There are no indications that PEDOT is formed outside the periphery of the CNTs. This could be accomplished by maintaining controlled interfacial polymerization in the system, whereby the aqueous layer containing $\text{Fe}(\text{ClO}_4)_3$ is retained by the hydrophilic surface of the acid-functionalized CNTs and the subsequent polymerization of EDOT is confined to the water/n-butanol interface. Prevention of bulk polymerization of EDOT in the vacant space available in BP thus ensures preservation of adequate porosity in the system all the while maintaining a high active surface area through the interconnected and 1D aligned polymer network. Good porosity in the electrode facilitates penetration of ions, which is a key parameter in achieving low charge-transfer resistance during the charge/discharge process of the device. This, along with the high available surface area of the electroactive layer, makes the system technically ideal to achieve enhanced capacitance and capacitance retention under different dragging conditions. The TEM image in [Figure 2c](#) shows that the CNTs in BP have a thickness of 10 nm, whereas the thickness of the tube increases to 16.6 nm in BP-2C ([Figure 2d](#)). Thus, PEDOT, as indicated by the TEM images, forms a very thin nanometre-scale layer on the CNTs.

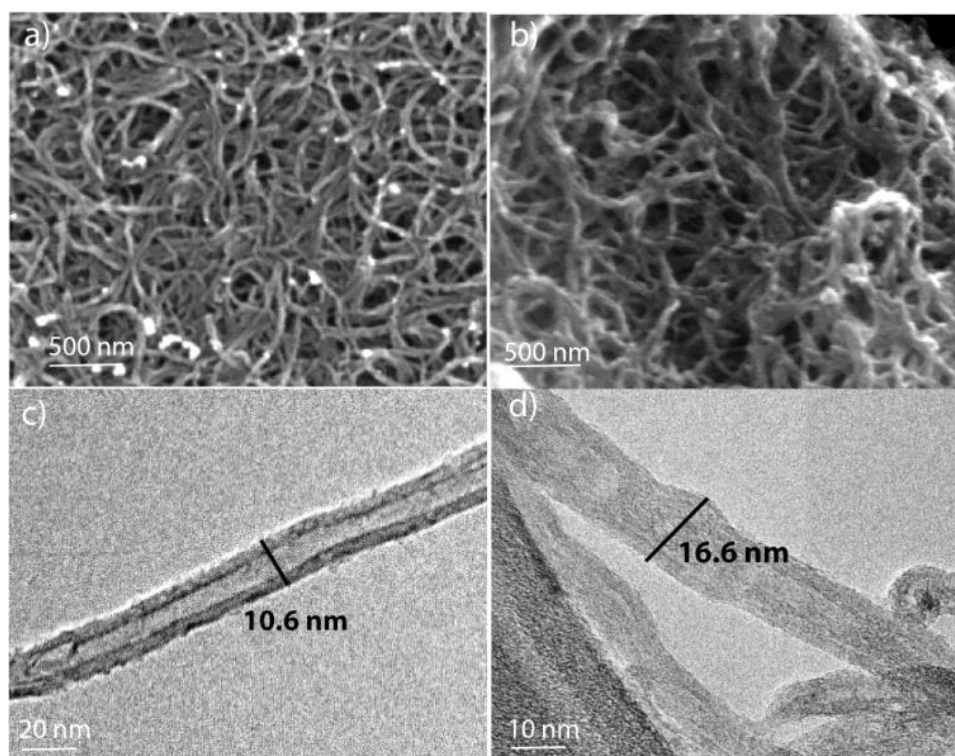


Figure 2. FESEM and TEM images: a) FESEM image of BP (top view) depicting the intertwined network structure of CNTs, b) FESEM image of BP-2C, which shows that the intertwined structure in BP is retained completely in BP-2C after the polymer coating, c) TEM image showing the diameter of the CNTs in BP and d) TEM image showing the increased diameter of the CNTs in BP-2C due to the formation of a layer of PEDOT on the surface.

2.3.3 X-ray Diffraction Analysis

The X-ray diffraction pattern of PEDOT-modified buckypaper with two coatings of polymer (BP-2C) in **Figure 3** shows characteristic peaks at $2\Theta=13.40^\circ$ (200) and 25.70° (020). The (200) peak at 13.40° is shifted to higher angles from the usual peak position by 1.48° , which suggests close packing of the polymer chains. Together with the 1D alignment of PEDOT, the close packing between the polymer layers results in faster and easier charge hopping. The characteristic peaks of the multiwalled (MW) CNTs can be identified at 2Θ values of 26° (002) and 42.80° (100).⁹

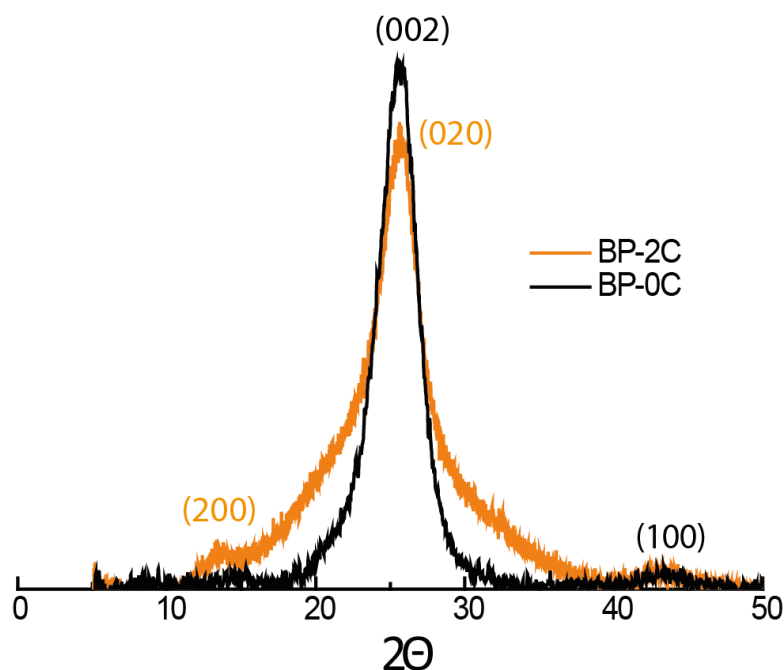


Figure 3. XRD patterns of the buckypaper (BP) and the PEDOT modified buckypaper (BP-2C).

2.3.4 Surface Area Analysis

Surface area and pore size are especially important in solid-state supercapacitors because the structure of the electrode must provide enough space in the matrix for infiltration of the gel electrolytes, which have relatively high viscosity compared to their liquid counterparts. Hence, the high surface area of the electrode must be supplemented by adequate porosity in

the system. BET analysis of BP-2C was carried out to determine the surface area and pore size distribution. The N_2 adsorption isotherms of BP and BP-2C (Figure 4a) indicate Type V behaviour. BP-2C and its pristine counterpart BP have more or less the same surface area (BP: $296 \text{ m}^2 \text{ g}^{-1}$; BP-2C: $300 \text{ m}^2 \text{ g}^{-1}$). The pore size distribution profiles of BP and BP-2C (Figure 4b), which lie in the range of 10–25 nm, clearly indicate mesoporosity of the CNT networks, and thus an important criterion for their serving as potential electrode materials for solid-state supercapacitors is fulfilled. The average pore volume of the composite paper is estimated to be $0.95 \text{ cm}^3 \text{ g}^{-1}$. The surface area and pore size analysis of BP and BP-2C clearly indicates that the intrinsic porosity and surface area of the former are more or less retained in the latter. Credit for this goes to the interfacial polymerization of EDOT, which controls polymer growth as a thin layer confined on the surface of the MWCNTs. Avoidance of bulk polymerization by this method helps to prevent pore blocking and thereby ensures a relatively high pore volume of $0.95 \text{ cm}^3 \text{ g}^{-1}$.

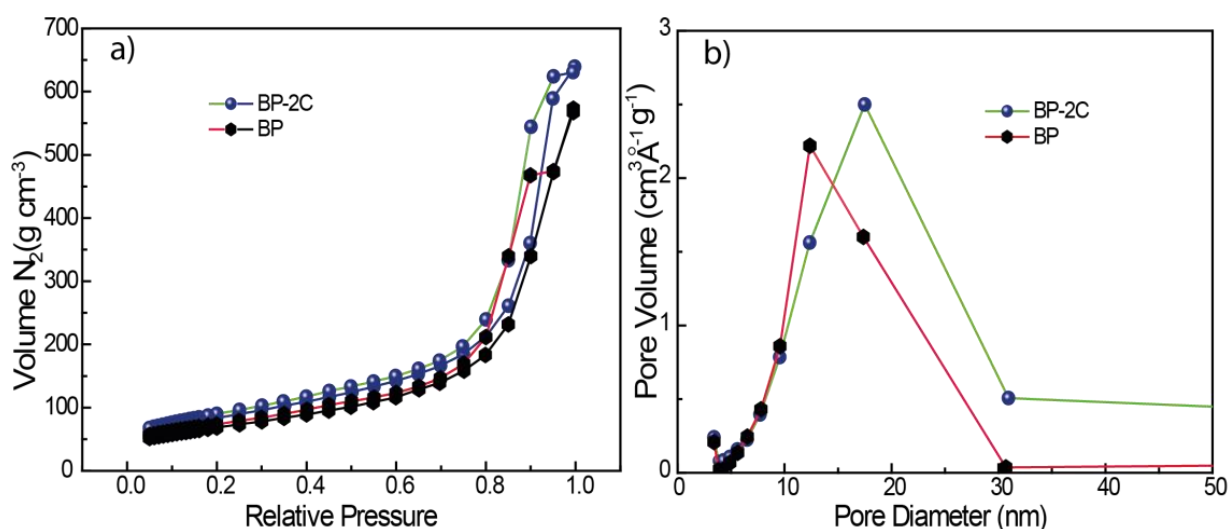


Figure 4. Pore distribution analysis: a) the adsorption isotherms of the surface modified buckypaper (BP-2C) and BP and b) the comparative pore distribution profiling of BP and BP-2C.

2.3.5 Elemental Mapping Analysis

To further substantiate the role of the surface functionality and hydrophilicity, cross-sectional elemental mapping was carried out to check the distribution of the polymer phase deep into the CNT network. The well-dispersed and uniform sulphur distribution evident in the case of BP-2C (Figure 5a) confirms the homogeneous distribution of PEDOT along the thickness of BP-2C. Moreover, the distribution of chlorine (Figure 5b) is also quite undifferentiated, and thus further testifies to the penetration and uniform coating of the polymer. To check the

superiority of interfacial polymerization, a PEDOT-coated BP sample was also prepared by non-interfacial polymerization (designated BP-2C-NI), in which water was replaced by n-butanol as the solvent for $\text{Fe}(\text{ClO}_4)_3$. The elemental mappings of sulphur and chlorine in the sample clearly show that the polymerization is limited to the surface and is non-uniform (Figure 5c, d).

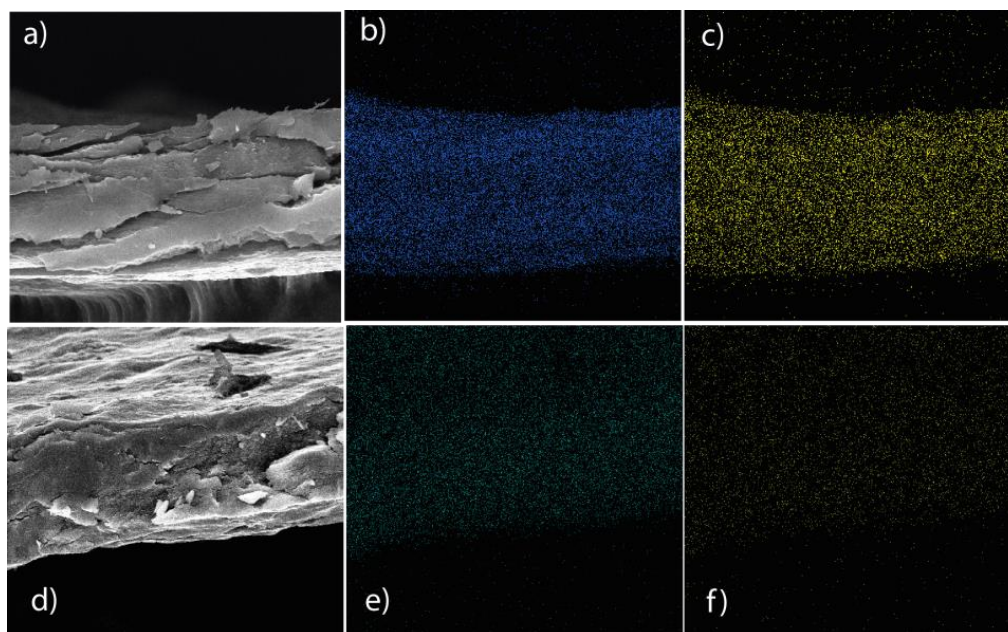


Figure 5. Elemental mapping (acquired through the vertical cross-section) of sulphur and chlorine for the interfacial and non-interfacial polymerized PEDOT: a) SEM image of the cross-section of BP-2C; b) and c) represent the distribution of sulphur and chlorine for the PEDOT modified buckypaper (BP-2C) formed through the interfacial polymerization; d), e) and f) represent the SEM image, elemental mapping of sulphur and chlorine, respectively, in the case of BP-2C-NI, *i.e.*, the PEDOT modified buckypaper prepared by the non-interfacial polymerization.

This difference in the nature of the polymerization in the latter case is attributed to the weak interaction between the hydrophobic n-butanol and the hydrophilic CNTs which prevents its penetration into the interior and formation of a uniform coating of the oxidizing agent.

2.3.6 Sheet Resistance and Flexibility Test

To achieve high performance, it is necessary to maintain the sheet resistance of the electrode as low as possible. The sheet resistance of the functionalized CNT, measured by the four-probe method, is $2.3 \Omega \square^{-1}$, which increased to $4 \Omega \square^{-1}$ after BP formation, presumably due to the damage caused by sonication and the large dead volume in the CNT network of the BP. After coating with a PEDOT layer by interfacial polymerization, the sheet resistance

decreases from $4 \Omega \square^{-1}$ for BP to $3 \Omega \square^{-1}$ for BP-3C (Figure 6a). Although the sheet resistance is lowest for BP-3C, the capacitance properties of BP-2C are found to be superior. We also checked the effect of bending on the conductivity of the electrode by performing current–voltage (I–V) polarization at different numbers of bending cycles. As shown in Figure 6b, no appreciable changes in the resistance and I–V features at different bending cycles are noticed and the plots are perfectly superimposable. To further confirm the role of the surface functionality of the CNTs of BP, we carried out the same synthetic protocol for preparing another type of BP from pristine un-functionalized CNTs. The sheet resistance in this case is $2.26 \Omega \square^{-1}$, and it shows no appreciable change with subsequent PEDOT coating due to the less effective surface-aligned polymerization (Figure 7). In this case, since the CNTs are un-functionalized, the surfaces of the tubes do not bear carboxyl groups and

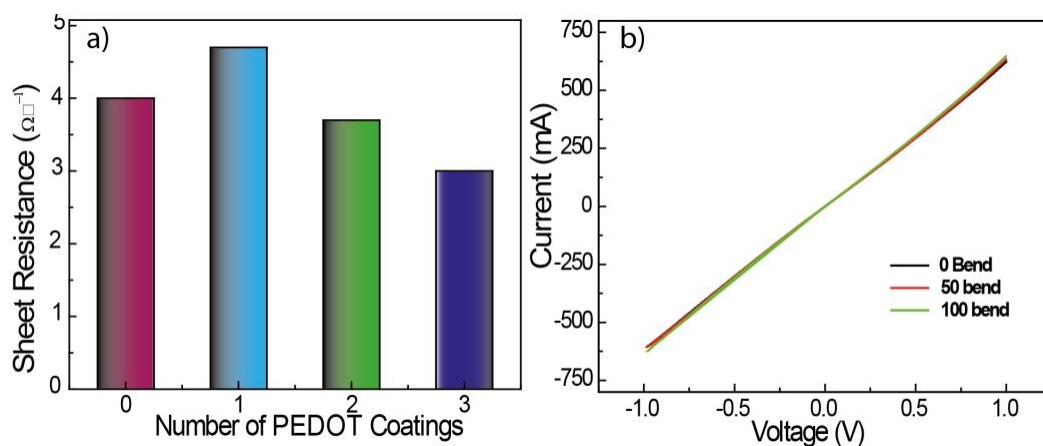


Figure 6. a) Variation in the sheet resistance of PEDOT-modified BP as a function of the number of the polymer coatings. The sheet resistance gradually decreases due to the increased loading of the highly conducting PEDOT phase; b) I–V polarization curves for the different bending states of BP-2C.

the conjugation of the exterior wall is intact, in contrast to the functionalized CNTs. Hence, the conductivity of the paper in this case is higher compared to that prepared from the functionalized CNTs. This result thus provides support for the influential role played by the hydrophilic nature of the CNT surface in accomplishing 1D surface alignment of the polymer to give a very low sheet resistance.

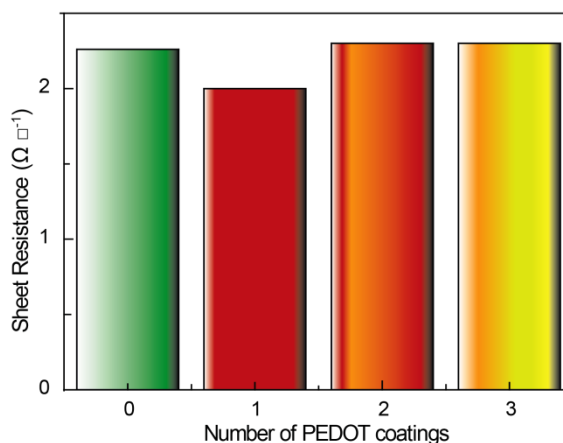


Figure 7. Variation of the sheet resistance with increasing the number of the PEDOT coatings for the PEDOT modified BP directly prepared from the pristine un-functionalized CNTs.

2.3.7 Electrochemical Characterization

All the electrochemical studies were carried out with a two-electrode solid-state device by using 20 wt % PVA-LiCl gel electrolyte. BP-2C was selected as the prime candidate for this analysis due to its optimum performance compared to the other PEDOT-coated materials.

2.3.7.1 Cyclic Voltammetry

Cyclic voltammetry is the most widely used technique to examine the capacitance behaviour of supercapacitors. All the measurements were carried out at room temperature in a potential window of 1.2 V and at different scan rates of 5, 10, 50, 100, 200, and 500 mV s^{-1} . The solid-state device prepared from bare BP shows typical double-layer capacitance behaviour in the cyclic voltammogram (CV) recorded at a scan rate of 5 mV s^{-1} (Figure 8a). The areal capacitance measured in this case is 182 mF cm^{-2} . Compared to the device made with the BP electrodes, corresponding devices with electrodes based on its PEDOT-based counterparts show marked difference in the CV features with the presence of the broad redox peaks of PEDOT (Figure 8a). This can be attributed to the pseudocapacitive behaviour of the polymer in the system. The capacitance increases gradually up to two coatings of PEDOT (*i.e.*, BP-2C) and it remains more or less same in the case of the system with three coatings (*i.e.*, BP-3C). Areal and volumetric capacitance calculated for the single electrode from the charge/discharge measurements for BP-2C are 354 mF cm^{-2} and 44 F cm^{-3} , respectively. These values are significantly high compared to the corresponding values of BP (182 mF cm^{-2} and 36.4 F cm^{-3} , respectively). This large increase in capacitance originates from the controlled interplay of the uniformly aligned and interconnected morphology of PEDOT with the high pore volume and interfacial area acquired by the system. The CVs of the device made

from BP-2C retain more or less similar features even at very high scan rates (Figure 8b). This retention of the capacitive nature of the system authenticates the credibility of the device as an efficient supercapacitor when the power requirements significantly rise. This was made possible by the attainment of ultralow resistance and excellent conductivity of the electrode material. To validate the flexibility of the device, the measurement was also carried out on bending the device at an approximate angle of 60° between the two ends. The nearly superimposable CVs of the device in the bent and normal states (Figure 9) underline the flexibility of the device.

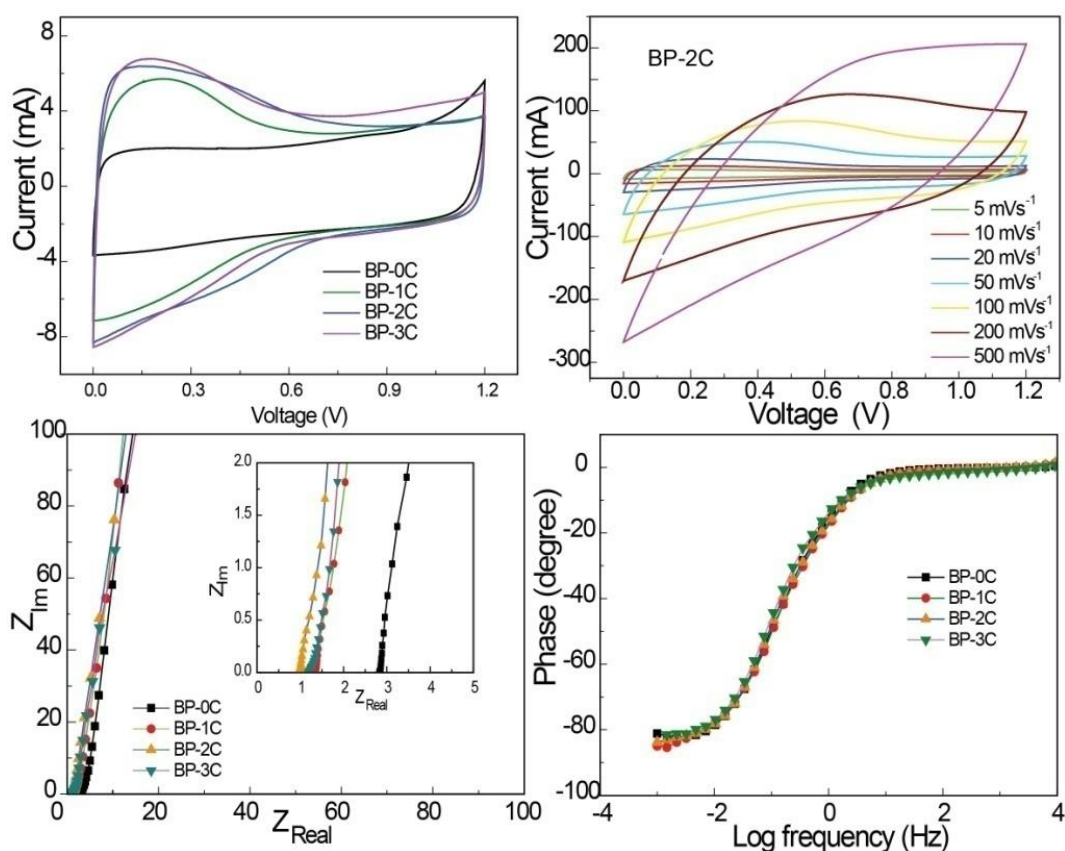


Figure 8. a) CVs depicting the difference in the capacitance behaviour of BP and the BP-PEDOT-based solid-state devices having different numbers of PEDOT coatings, recorded at a scan rate of 5 mV s^{-1} ; b) CVs of the BP-2C device recorded at different scan rates; c) Nyquist plots for the devices with different coatings of PEDOT where the inset shows the zoomed portion of the high frequency region of the parent plots; d) Bode plots for devices having different PEDOT coatings, depicting the phase-angle changes.

2.3.7.2 Electrochemical Impedance Spectroscopy

To analyze the internal characteristics of the BP-2C electrode, electrochemical impedance spectroscopy (EIS) was performed in the frequency range from 1 MHz to 1 mHz on the BP-

2C based solid-state device. The Nyquist plot of the imaginary component of the impedance Z_{im} versus the real component Z_{real} is shown in Figure 8c. The value of the intercept on the X-axis (Z_{Real}) gives the ESR of the device; the main contribution to the ESR comes from the electrode and electrolyte resistance. Even with PVA-LiCl gel electrolyte, which is less conducting than conventional acid- or alkali-based electrolytes, a low ESR of 0.95Ω could be measured. This substantially low ESR for the solid electrolyte can be ascribed to the low resistance of the electrode and to the effective interface of the gel electrolyte inside the porous electrode. The EIS profile does not show an evident semicircle in the high-frequency region, and this indicates that an electrode having low charge-transfer resistance was obtained.¹⁰ Such low impedance testifies to efficient impregnation of the electrolyte on the electrode surface resulting in the formation of well-organized electrode/electrolyte interface in the electrode matrix. The first segment in the impedance loop is generally followed by the Warburg diffusion line, which can be taken as a combination of the resistive and capacitive behaviour of the ions penetrating into the pores of the electrode and gives indirect evidence for the porous nature of the electrode.¹¹ The absence of an appreciable diffusion line in the Nyquist plot evidences a short path length of ion diffusion during the charge/discharge process.¹² It is followed by a nearly straight line inclined to the Z_{im} axis, representing the dominant capacitive behaviour due to the formation of ionic and electric charges of the double-layer system in the mesopores of BP-2C. Further, the knee frequency, that is, the frequency below which the whole capacitance can be realized, of BP-2C of 26 Hz (Figure 10) is higher than those of commercial supercapacitors (knee frequency < 1 Hz) designed for high power applications.¹³

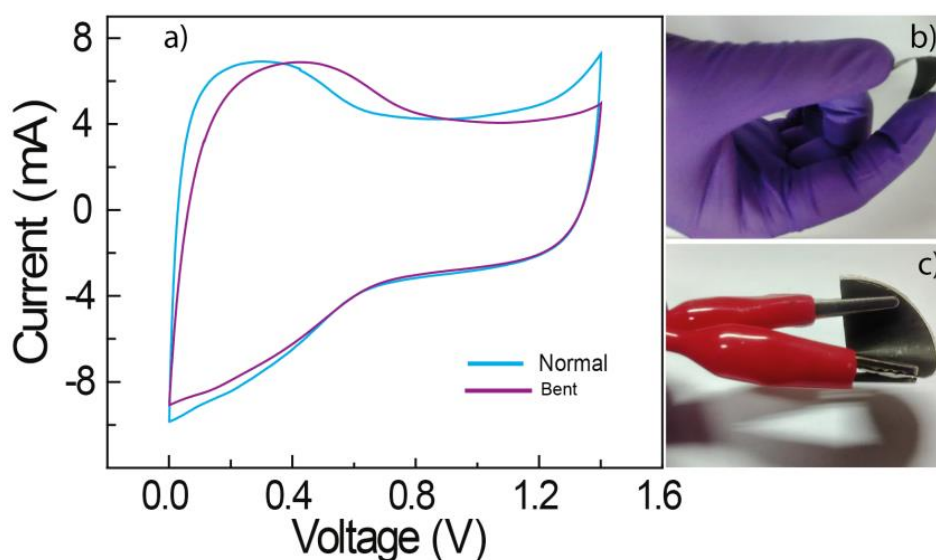


Figure 9. a) Cyclic voltammograms recorded at 5 mV s^{-1} under normal and bent conditions of BP-2C where the CV profiles are well-nigh superimposable indicating its utility under flexible conditions; b) and c) represent the bending conditions of the device during the CV recording.

A close look at the EIS profiles of the different polymer coated devices disclosed enhanced capacitive behaviour of the system with increasing the PEDOT loading. This is evident from the progressive shift of the capacitive line towards the imaginary axis in the Nyquist plot. The RC time constant, which is another important performance indicator for evaluating the response characteristics of a supercapacitor, represents how fast the stored energy can be delivered on demand. The RC time constant improved from 2.46 s for BP to 1.61 s for BP-2C. A Bode plot was constructed to estimate the phase-angle changes with respect to the number of PEDOT coatings on BP (Figure 8d). As expected, the phase angle improved from 82° for BP to 84° for BP-2C, which is close to the ideal phase angle of 90° .

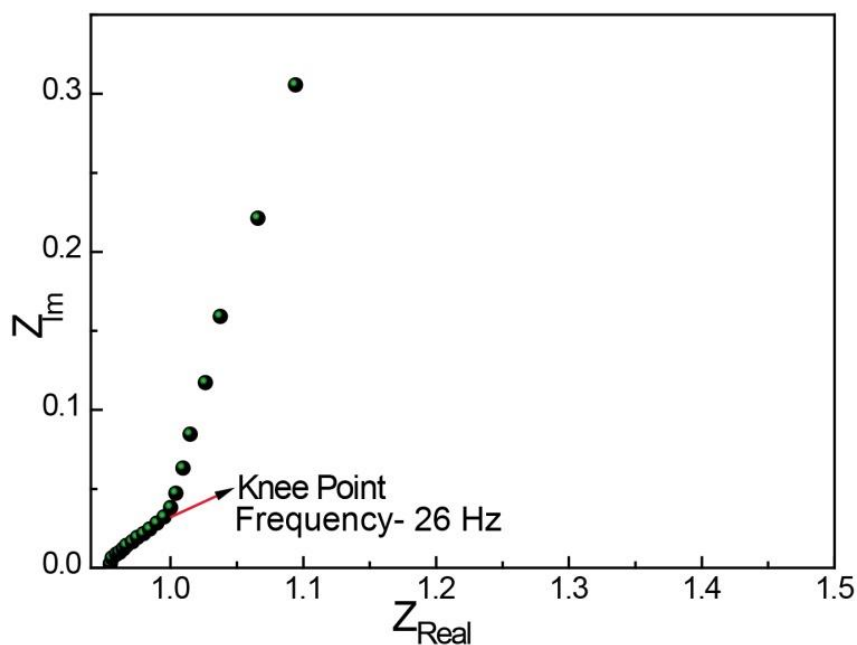


Figure 10. Nyquist plot showing the knee frequency (the frequency below which capacitor shows dominant capacitance behaviour) of BP-2C.

2.3.7.3 Galvanostatic Charge-Discharge

To assess the performance and cycle life of the solid-state device, galvanostatic charge/discharge (GCD) was carried out at current densities varying from 1 to 5 mA cm^{-2} . Figure 11a shows the GCD profiles of the flexible device derived from BP-2C, which show the typical triangular waveforms. However, a close look at the plots reveals that the GCD curves deviate slightly from ideal triangular shape, presumably due to the pseudocapacitive

contribution of PEDOT, which is in good accordance with the CV profiles. In addition, the shapes of the curves at different current densities are quite similar. The areal capacitance and volumetric capacitance of the BP-2C-based device are estimated to be 354 mF cm^{-2} and 18 F cm^{-3} , respectively. The areal capacitance of the BP-2C-based device is almost twice that obtained for the device based on BP (182 mF cm^{-2}). Moreover, the lightness gives the device a specific capacitance of 13.4 F g^{-1} , which is calculated on the basis of the overall device weight (127 mg). This value is higher than the corresponding value (4.6 F g^{-1}) obtained with the BP device. Furthermore, the volumetric capacitance measured for a single electrode with a thickness of 80 mm is 44 F cm^{-3} . The output capacitance of the device of 1.7 F is an outstanding value for such a thin, lightweight supercapacitor assembly. Such a high capacitance is essentially possible because of the ease of accessibility of the ions into the pores and effective impregnation of the electrolyte on the electrode,¹⁴ which significantly benefit from the highly porous network and pore size distribution of BP-2C. Figure 11b shows the change in the areal and volumetric capacitances at different current densities. When the current density is increased fivefold to 5 mA cm^{-2} , the decreases in the areal capacitance and volumetric capacitance are just 17 and 16 %, respectively.

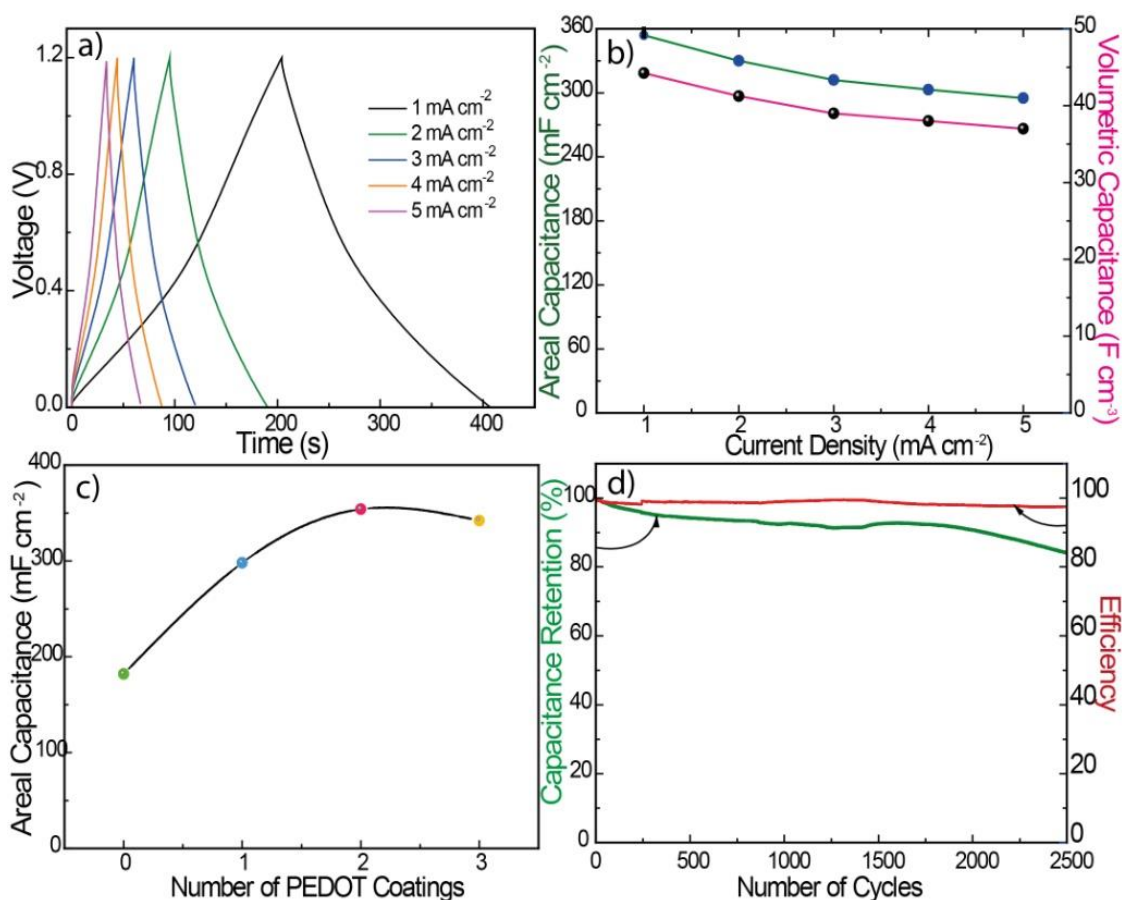


Figure 11. a) CD profiles of the BP-2C-based flexible solid-state supercapacitor device at different current densities; b) plots showing the variation in areal capacitance and volumetric capacitance as a function of the current density; c) plot showing how the areal capacitance increases with the number of PEDOT layers; d) capacitance retention and coulombic efficiency measured at a current density of 1 mA cm^{-2} over 2500 cycles.

Besides, by using PVA-LiCl gel as the electrolyte, the energy density could be further improved, since the operating potential is extendable to 1.2 V. Because the gel electrolyte is neutral, it helps to increase the overpotential for hydrogen and oxygen evolution and thereby assists in expanding the operable potential window of the device. In addition, the gel electrolyte prevents dissolution and irreversible electrochemical oxidation of the electrode material.¹⁵ The energy density calculated for the single electrode at 1 mA cm^{-2} current density is 8.85 mWh cm^{-3} , which is reasonably high for such a thin electrode without a current collector. The specific capacitance of PEDOT in the composite is 138 F g^{-1} , and those of the composite and CNT in the BP are 73 and 50 F g^{-1} , respectively, at a current density of 1 mA cm^{-2} . Besides high energy density, the system could also deliver high power density owing to the low internal resistance. The measured power densities are 9.94 W cm^{-3} for the electrode and 3.93 W cm^{-3} for the device. **Figure 11c** shows a linear dependence of the areal capacitance with the amount of PEDOT up to two coatings; thereafter, the energy density reaches nearly saturation behaviour with further increase in the number of PEDOT coatings. The cycle stability of the device (**Figure 11d**) was tested for 2500 cycles, and the capacitance retention was found to be 84%. Here, the decrease in the capacitance can be attributed to electrolyte degradation or material oxidation due to cycling at high potential.

2.3.7.4 Performance Comparison of Interfacial and Non-interfacial Polymerized PEDOT

To check the superiority of the interfacial polymerization process over the non-interfacial route, a PEDOT-modified BP was prepared by using n-butanol instead of water as the solvent for the oxidizing agent (BP-2C-NI). The areal capacitance calculated for BP-2C-NI was 302 mF cm^{-2} , as opposed to 354 mF cm^{-2} for BP-2C (**Figure 12a**). Moreover, an unfavourable deviation in the impedance behaviour is observed when the polymerization is carried out by the non-interfacial route: the ESR increases by more than 100% to 2.6Ω (**Figure 12b**).

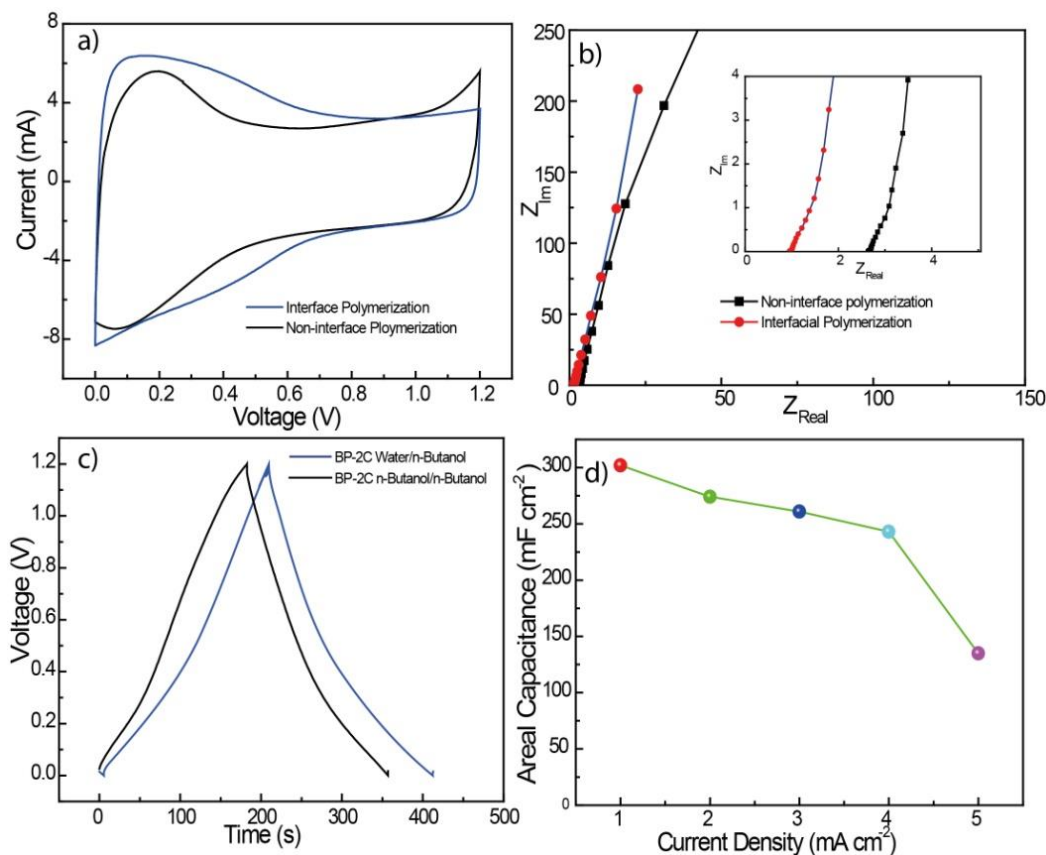


Figure 12. Electrochemical properties of BP-2C-NI device prepared by following non-interface chemistry: a) cyclic voltammograms recorded at 5 mV s^{-1} of the devices having the electrodes synthesized through the interfacial and non-interfacial polymerization routes, b) Nyquist plots for the two devices, where the ESR of BP-2C-NI is found to be increased significantly compared to BP-2C, c) charge-discharge curves at a current density of 1 mA cm^{-2} in the case of the two devices, where the charging time has been decreased in case of BP-2C-NI, and d) change in the areal capacitance with current density in the case of BP-2C-NI, where the capacitance retention is very poor at high current density.

One striking difference between the two systems is the capacitance retention at high current density. In the case of BP-2C-NI, only 44% of the original capacitance could be retained when the current density was raised from 1 to 5 mA cm^{-2} (Figure 11d), as opposed to 83% retention displayed by BP-2C. These experiments thus clearly show the advantages of the current strategy adopted for maintaining the PEDOT phase in the electrode over the conventional method.

2.4 Conclusion

A thin and flexible solid-state supercapacitor could be developed by using a hybrid electrode derived from MWCNT-based BP and PEDOT and creating an electrode/electrolyte interface

by infiltration of PVA-LiCl gel electrolyte. Interfacial polymerization ensured surface-aligned growth of PEDOT along the surface of the CNTs in the BP. The hydrophilic interaction between the carboxyl groups on the surface of CNTs and the oxidizing agent, iron perchlorate, helped the system to establish a uniform and aggregate-free growth pattern of PEDOT. This controlled growth of the polymer phase and effective intercalation with the gel electrolyte helped to realize a flexible electrode with low sheet resistance and charge-transfer resistance. Careful optimization of the composition of PEDOT in the paper provided an electrode with an ultralow sheet resistance of $3.4 \Omega \square^{-1}$ and an ESR of 0.95Ω . A solid-state supercapacitor with a thickness of 210 μm , fabricated by sandwiching two BP-2C electrodes with a Celgard separator, was found to be flexible with good retention of the capacitive characteristics in the bent and normal states. The device delivered a volumetric capacitance of 18 F cm^{-3} and an areal capacitance of 354 mF cm^{-2} , which are the highest in its class. The laboratory scale process demonstrated here is scalable and can be conveniently applied to prepare large-area PEDOT-modified BP in a short span of time.

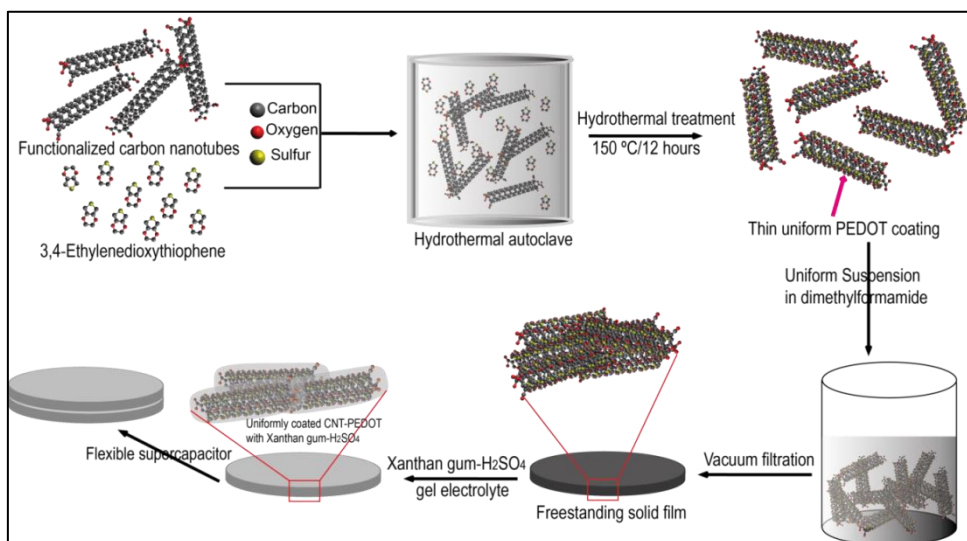
2.5 References

1. S. Kirchmeyer and K. Reuter, *Journal of Materials Chemistry*, 2005, **15**, 2077-2088.
2. B. Anothumakkool, R. Soni, S. N. Bhange and S. Kurungot, *Energy & Environmental Science*, 2015, **8**, 1339-1347.
3. S. Lehtimäki, M. Suominen, P. Damlin, S. Tuukkanen, C. Kvarnström and D. Lupo, *ACS Applied Materials & Interfaces*, 2015, **7**, 22137-22147.
4. S. W. Lu, C. X. Zhang, X. J. Zeng, J. J. Wang, P. Nie and Y. Gao, *Advanced Materials Research*, 2013, **765-767**, 3162-3165.
5. C. Meng, C. Liu, L. Chen, C. Hu and S. Fan, *Nano Letters*, 2010, **10**, 4025-4031.
6. S. Hu, R. Rajamani and X. Yu, *Applied Physics Letters*, 2012, **100**, 104103.
7. L. Liu, Y. Yu, C. Yan, K. Li and Z. Zheng, *Nature Communications*, 2015, **6**, 7260.
8. L. J. Sweetman, L. Nghiem, I. Chironi, G. Triani, M. in het Panhuis and S. F. Ralph, *Journal of Materials Chemistry*, 2012, **22**, 13800-13810.
9. T. Y. Kim, C. M. Park, J. E. Kim and K. S. Suh, *Synthetic Metals*, 2005, **149**, 169-174.
10. K. Lota, V. Khomenko and E. Frackowiak, *Journal of Physics and Chemistry of Solids*, 2004, **65**, 295-301.
11. P. L. Taberna, P. Simon and J. F. Fauvarque, *Journal of The Electrochemical Society*, 2003, **150**, A292.
12. F. Müller, C. A. Ferreira, D. S. Azambuja, C. Alemán and E. Armelin, *The Journal of Physical Chemistry B*, 2014, **118**, 1102-1112.
13. J. R. Miller, *ECS Symp. Proc. Electrochem. Soc.*, 1996, **246**.
14. B. Anothumakkool, A. Torris A. T, S. N. Bhange, M. V. Badiger and S. Kurungot, *Nanoscale*, 2014, **6**, 5944-5952.
15. G. Wang, X. Lu, Y. Ling, T. Zhai, H. Wang, Y. Tong and Y. Li, *ACS Nano*, 2012, **6**, 10296-10302.

Chapter-3

Oxidant-Free Hydrothermal Synthesis of Ultrathin PEDOT over CNTs and Introduction of Xanthan Gum-Based Shear Thinning Gel electrolyte

Performance of a pseudocapacitive material in supercapacitor devices largely depends on how comfortable and facile the movement of electrolyte ions is to the electrode. At the same time, resistance properties of the electrode material play a vital role in the capacitive behaviour, where lowering the resistance leads to improved performance. PEDOT possesses high theoretical conductivity; however, high density of grain boundaries, low accessible surface area and low rate capability have been pervasive issues for the PEDOT-based supercapacitors. To this end, a hydrothermal method is proposed in this chapter where oxygen functional



groups incorporated on the surface of CNTs are utilized to polymerize EDOT. PEDOT forms an ultrathin well-aligned coating on the surface of CNTs.

This arrangement keeps the number of grain boundaries to the minimum and also increases the electrochemically active surface area. Also, a shear-thinning Xanthan gum- H_2SO_4 gel electrolyte is introduced to overcome the low impregnation of the conventional polyvinyl-based electrolyte due to the hydrophobicity of the CNT-PEDOT composite. This gel electrolyte on the application of stress lowers its viscosity which helps in the deeper impregnation of the electrolyte on the entire available surface. The device showed a very low ESR of 0.31Ω which leads to a high power density of 74 W cm^{-3} .

The Manuscript of this work has been communicated

3.1 Introduction

As an alternative to carbon, intrinsic conducting polymers like PEDOT which exhibit high capacitance caused by Faradaic reaction have been tested for application in supercapacitors.¹ Due to its high stability, PEDOT has found applications in antistatic coatings,² capacitors, touch panels, organic light emitting diodes, organic solar cells, etc.² PEDOT in doped-state possesses high conductivity and capacitance.³ Due to the above properties, it is projected as a promising material for supercapacitor application. PEDOT undergoes doping-dedoping on the application of potential in electrolyte solution.⁴ Thus, only the surface of polymer which is in contact with the electrolyte is used in charge storage. For obtaining maximum performance from PEDOT, it is necessary to lower down the amount of unused PEDOT or in other words, forming a few nanometer thin PEDOT. However, thin films show high sheet resistance which adversely affects the performance.⁵ Thus a viable strategy to overcome this issue would be to form a very thin layer of PEDOT on a conducting core. PEDOT on the surface will store charge through Faradaic reaction while the conducting core helps current collection and transport. However, such an assembly is very difficult and unmanageable as it requires precise control of polymerization of EDOT on the surface to obtain very thin layer without any aggregate formation. To this end, in the first chapter, an interfacial oxidative polymerization of PEDOT on the carbon nanotube surface in a buckypaper is introduced. PEDOT was aligned exclusively on the surface of CNTs without any aggregate or bulk PEDOT formation. However, there is plenty of room to further thin down the PEDOT coating on CNT to reduce inactive polymer amount to achieve high gravimetric capacitance. Furthermore, PEDOT nanotubes have also been synthesized through alumina template method; the nanotubes obtained had a big size ranging up to few hundreds of nanometer. The capacitance obtained was relatively low at 150 F g^{-1} .⁶ This report also studied the effect of PEDOT loading on capacitance; at higher PEDOT loadings, the composite did not show any improvement in the capacitance value. This shows that only limited amount of PEDOT is used for charge storage, the rest remains un-utilized. Therefore, to increase the specific capacitance of PEDOT, it is important to reduce the amount of un-utilized PEDOT. A conventional method for PEDOT synthesis uses oxidizing agents like FeCl_3 ,⁷ $\text{Fe}(\text{ClO}_4)_3$,⁸ $(\text{NH}_4)_2\text{S}_2\text{O}_3$,⁹ etc. which causes EDOT polymerization through oxidative polymerization. In this case, it is not easy to restrict the PEDOT only to the surface of conducting core; also, the thickness of PEDOT does not have sufficient control. Vapor phase polymerization, where either the monomer or the oxidizing agent in the vapor form is used which then deposits over the substrate leading to the PEDOT synthesis, has been applied to form thin PEDOT nanofibrils.¹⁰ However, all the above

methods use oxidizing agents. Oxidant-free thin coating of PEDOT can be prepared through electrochemical polymerization; however, this method is not suitable for large-scale synthesis. In this chapter, we have synthesized an ultrathin PEDOT coating on the surface of functionalized CNTs *via* an oxidant-free hydrothermal method. The oxygen-containing functional groups on the surface of CNTs themselves act as the oxidizing agent which under high temperature and pressure oxidizes EDOT and causes polymerization. This strategy substantially reduces the amount of unused PEDOT as only a thin layer of PEDOT is formed which helps to achieve high specific capacitance. CNTs act as a conducting core and scaffold for PEDOT; CNTs facilitate current collection from PEDOT and its transfer to the outside circuit. Also, a new Xanthan gum-based H₂SO₄ gel electrolyte is also demonstrated, which shows superior performance compared to the conventional PVA-H₂SO₄ gel electrolyte with respect to infiltration and rate capability. This gel electrolyte exhibits improved equivalent series resistance and frequency behavior.

3.2 Experimental Section

3.2.1 Materials

CNTs were purchased from Global Nanotech. 3,4-Ethylene dioxythiophene and polyvinyl alcohol were procured from Sigma-Aldrich. Xanthan gum was supplied by TCI Chemicals. Sulphuric acid was purchased from Rankem Chemicals. All the chemicals were used as such without any further purification.

3.2.2 Functionalization of Carbon Nanotubes

500 mg of CNT was soaked in 36 ml nitrating mixture (conc. H₂SO₄ and conc. HNO₃ in 3:1) for 6 h. The CNT-acid mixture was then sonicated in a bath sonicator for 4 h for functionalization. The mixture was then washed with copious amount of DI water, filtered and dried.

3.2.3 Synthesis of PEDOT of PEDOT-CNT Composite

In a typical synthesis, functionalized CNTs were mixed in de-ionized water through sonication. Subsequently, EDOT monomer was added to the solution, which was stirred to allow for uniform adsorption of the monomer on the CNTs. The reaction mixture was then kept for hydrothermal reaction at a temperature of 150 °C for 12 h. Three different CNT-PEDOT composites, 1:1, 1:2, 1:4, were synthesized by changing the weight ratio of CNT and PEDOT. Conventional synthesis of PEDOT involves oxidation of EDOT to a radical cation which then leads to the chain growth. In the synthesis strategy followed in this work, the

oxygen present in the functional groups on the CNT surface take over the role of an oxidizing agent. The same procedure was followed with pristine un-functionalized CNTs; in this case, no appreciable PEDOT synthesis was observed.

3.2.4 Free-Standing Electrode Fabrication

Free-standing CNT-PEDOT electrodes were prepared by following vacuum filtration method. In brief, 60 mg of CNT-PEDOT composite was dispersed in 100 ml N,N-dimethyl formamide through sonication for 1h. The suspension was then filtered using PTFE filter membranes through a vacuum filtration set-up. The film so formed was allowed to dry in the ambient condition, which was then peeled-off from the filter membrane to obtain self-standing flexible electrodes. The images of the flexible electrode prepared following the above method is given in [Figure 1](#).



Figure 1. Photograph of the free-standing electrode made from the CNT-PEDOT composite.

3.2.5 Preparation of Xanthan Gum- H_2SO_4 (XG-SA) Gel Electrolyte

XG-SA gel electrolyte was prepared in three different compositions of 2, 3 and 4 wt. %. In a typical preparation, in 10 ml 1M H_2SO_4 solution, 200, 300 and 400 mg XG was mixed to prepare 2, 3, and 4 wt.% XG-SA gel electrolyte. These mixtures were kept for stirring at 80 °C for 2h to obtain the gel electrolyte.

3.2.6 Preparation of PVA- H_2SO_4 Gel Electrolyte

Similarly, the most widely used 10 wt. % PVA-SA gel electrolyte was prepared by mixing 1g polyvinyl alcohol in 10 ml DI water which was stirred for 2 h at 80°C. After the gel electrolyte was cooled, 1 g conc. H₂SO₄ was added drop-wise with continuous stirring.

3.2.7 Solid Supercapacitor Prototype fabrication

Small discs of flexible electrodes were cut with a geometric area of 0.784 cm². A thin layer of the gel electrolyte was applied on the two such discs; it is then kept for some time for the electrolyte to infiltrate. Two electrolyte coated electrodes were then sandwiched together separated by a Celgard membrane to prevent electrical shorting. The images of the solid supercapacitor prototype are given in [Figure 2](#).

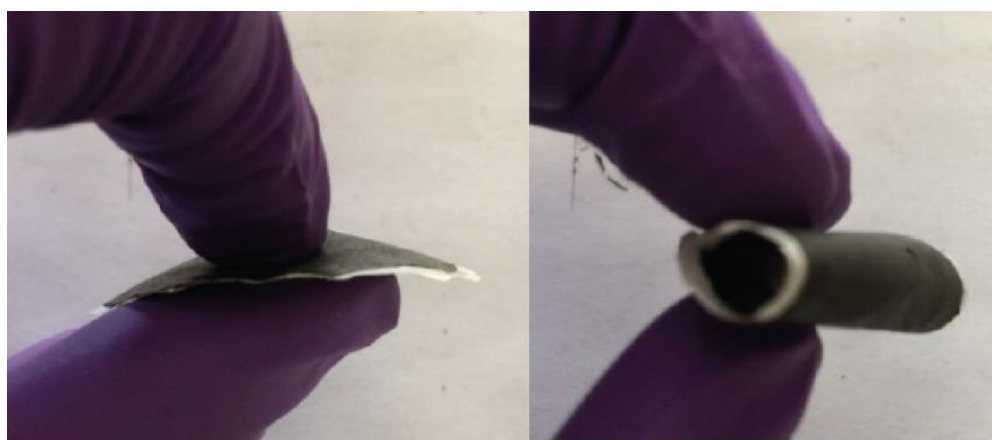


Figure 2. Digital photographs of the solid flexible supercapacitor prototype.

3.3 Result and Discussion

3.3.1 Infrared Spectroscopy

Infrared spectra of the functionalized CNT and CNT-PEDOT are given in [Figure 3a](#). IR spectrum of CNT shows C-O (alcohol) stretching frequency at 1111 cm⁻¹ which originates from the C-OH alcoholic functional groups. Also, a C-O (acid) stretching peak is detected at 1282 cm⁻¹ indicating the presence of the carboxylic functional groups. These IR features are usual for the CNTs functionalized using a nitrating mixture (HNO₃:H₂SO₄, 1:3). Close look at the IR spectrum of CNT-PEDOT shows new peaks which are assigned to the stretching of PEDOT. The peak at 704 cm⁻¹ can be assigned to the δ (C-H) vibration of the thiophene ring whereas a peak at 913 cm⁻¹ is ascribed to the O-C-C bond. The peak appeared at 984 cm⁻¹ shows the C-S stretching and the one at 1470 cm⁻¹ represents the C=C stretching of the aromatic thiophene ring.¹¹ An important observation here is the disappearance of the peak representing alcoholic C-O stretching in CNT-PEDOT; it is highly likely that it occurs due to

the interaction with EDOT during the polymerization. The role of the oxygen-containing functional groups present on the surface of CNT was assessed by following the same synthesis with the pristine un-functionalized CNTs. IR spectrum recorded for the material obtained when pristine CNTs were used is given in Figure 3b, and it is compared with that of CNT-PEDOT. The peaks observed for the various stretching frequencies of PEDOT, namely, $\delta(\text{C-H})$, O-C-C, C-O-C, C=C, etc., are not observed. It means that PEDOT is not formed when pristine CNTs were used. However, PEDOT is formed when functionalized CNT was employed. This observation points to the role of oxygen in the synthesis of CNT-PEDOT composite. The surface oxygen can act as an oxidant which can extract the electron from the EDOT molecule at a high temperature and pressure (provided in the autoclave) forming cationic radical, ultimately forming PEDOT.

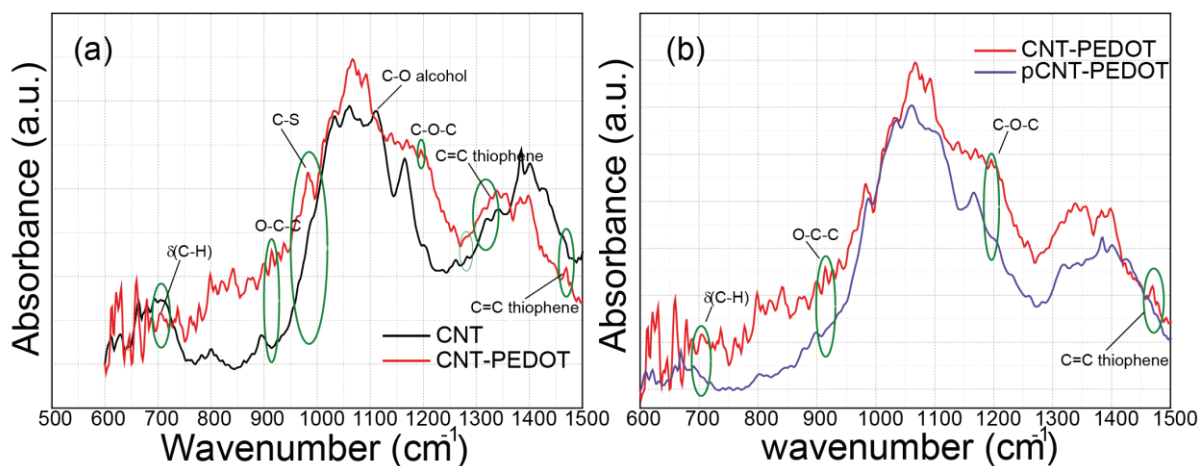


Figure 3. a) IR spectra of CNT and CNT-PEDOT composite, b) comparative IR spectra of the CNT-PEDOT composite prepared using functionalized CNT and pCNT-PEDOT composite synthesized with pristine un-functionalized CNT.

3.3.2 X-ray Diffraction Analysis

The formation of PEDOT has also been confirmed through X-ray diffraction (XRD) analysis; the XRD patterns of CNT and CNT-PEDOT are given in Figure 4. The 2θ value for the (002) plane of CNT is 25.76° ¹²; however, after PEDOT covering of carbon nanotubes, this value changed slightly to 25.53° as PEDOT also shows (020) reflection at a 2θ value of 25° ¹³. This change in diffraction angle can be assigned to the thin PEDOT layer formed on the CNT surface. Furthermore, a diffraction peak at a 2θ value of 11.22° appears due to the (200) reflections of PEDOT (Figure 4 inset); this diffraction peak is not observed for the CNTs. PEDOT coating is also indicated by the full width at half maximum (FWHM) measurement;

FWHM measured for the major reflection for CNT is 2.90° whereas after the PEDOT coating, FWHM increased to 3.03° . This increase in the FWHM for CNT-PEDOT can be understood by the amorphous nature of PEDOT formed on the CNT surface.

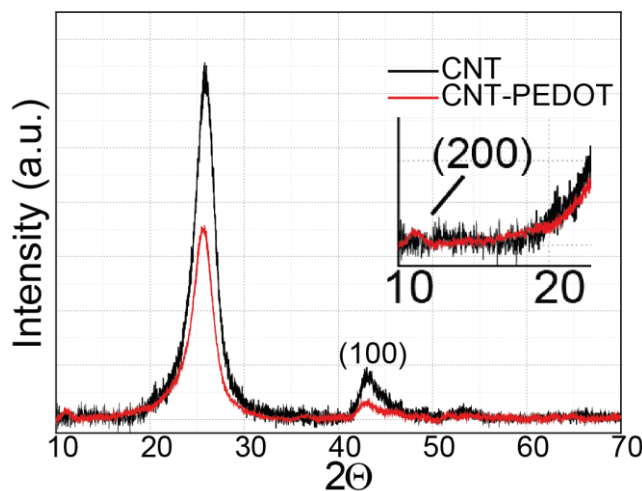


Figure 4. XRD patterns of CNT and CNT-PEDOT composite. Inset shows (200) reflection of PEDOT.

3.3.3 Thermogravimetric Analysis and Determination of PEDOT Loading

Thermogravimetric analysis (TGA) data of functionalized CNTs, PEDOT, CNT-PEDOT (1:2) and unfunctionalized CNT-PEDOT, given in [Figure 5](#), show quite different thermogram profiles. Functionalized CNT shows continuous weight loss, though to a small degree, due to decomposition of the surface functional groups into different gases. As CNT surface comprises of different functional groups which decompose at a different temperature, the thermogram shows continuous weight change. Thermogram of PEDOT shows a sudden change in weight at a temperature of 250°C , this feature in the curve is due to the sublimation of sulphur present in the PEDOT or its decomposition. The PEDOT present on the surface of CNTs should also show feature similar to pristine PEDOT. As expected, CNT-PEDOT (1:2) exhibits decomposition profile similar to PEDOT showing a characteristic weight loss starting at a temperature of 250°C . Also, the percentage loss observed for the composite is less than pristine PEDOT which infers to the low amount of PEDOT in the composite. TGA of the material obtained after the hydrothermal treatment of pristine CNT with EDOT shows profile similar to CNT. A small change observed in the weight is most probably caused by the adsorbed EDOT molecules that may have attached during the hydrothermal treatment. The content of sulfur in the composite can be used to compare the PEDOT amount in different composites. The percentage of sulfur is determined through element analysis (microanalysis). The content of sulfur increased with increase in the EDOT amount in the reaction mixture.

CNT-PEDOT 1:1 contains 2.22 % sulfur which increases to 5.81 and 6.32 % for 1:2 and 1:4 composites, respectively. The increased sulfur content can be related to the PEDOT amount on the CNT surface; therefore, the 1:4 composite contains the highest amount of PEDOT.

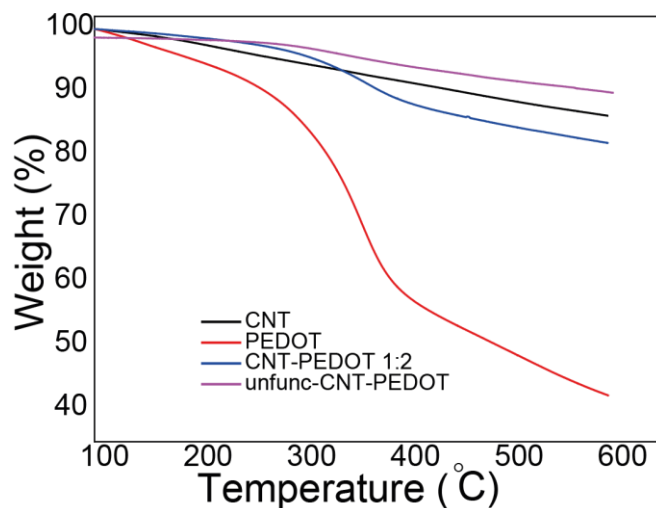


Figure 5. TGA profiles of CNT, PEDOT, and CNT-PEDOT composites.

3.3.4 X-ray Photoelectron Spectroscopy

Polymerization of EDOT on the surface of CNT was also studied through X-ray photoelectron spectroscopy (XPS); the corresponding data is given in Figure 6. XPS spectrum of CNT shows peaks for C1s at a B.E. of 284.6 eV, and signal for oxygen arising from the surface functional appears at a B.E. of 534.3 eV for O 1s. In the XPS of CNT-PEDOT, C 1s peak is shifted to a little higher B.E. at 285.1 eV which is similar to the B.E. reported for PEDOT. XPS signal for the sulphur S 2p appears at a B.E. of 165 eV; these results indicate polymerization of EDOT on the surface of CNTs.¹⁴ A small signal near S2p is due to Si 2s and Si 2p which appears from the silicon wafer.

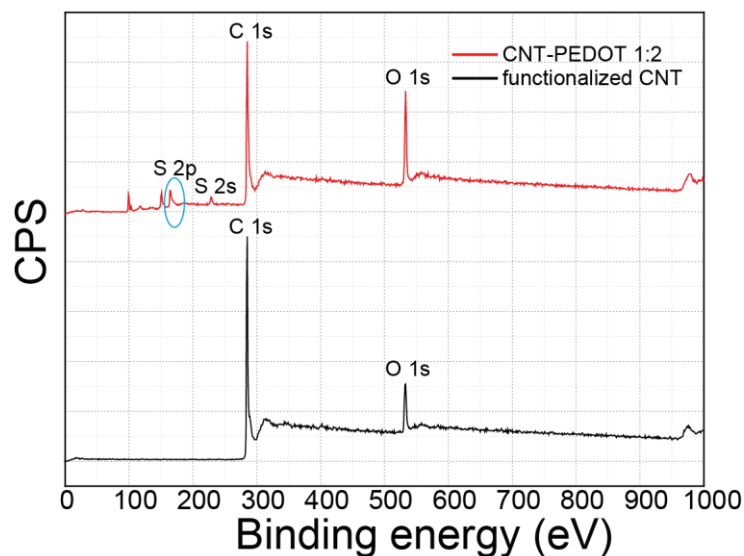


Figure 6. X-ray photoelectron spectra of CNT and CNT-PEDOT composite 1:2.

3.3.5 Electron Microscopy Analysis

Field emission electron microscopy (FESEM) images were recorded for CNT, CNT-PEDOT (1:1, 1:2, and 1:4) and CNT-PEDOT- FeClO_4 composite, where the later was prepared through the conventional method with $\text{Fe}(\text{ClO}_4)_3$ as an oxidizing agent. FESEM image of the CNT is given in [Figure 7a](#) which shows long thin tubes. SEM images for the different composites are given in the [Figure 7b-d](#); the images show similar features as CNT. An interesting thing to note is that any bulk or aggregates of PEDOT are not formed on the surface of CNTs. This well aligned and confined growth of PEDOT only on the surface is made possible by the surface restricted synthesis of PEDOT triggered by the surface functional groups. This surface confined thin layer formation of PEDOT is necessary to reduce the amount of inactive material. This consequently results in high specific capacitance for the composite.

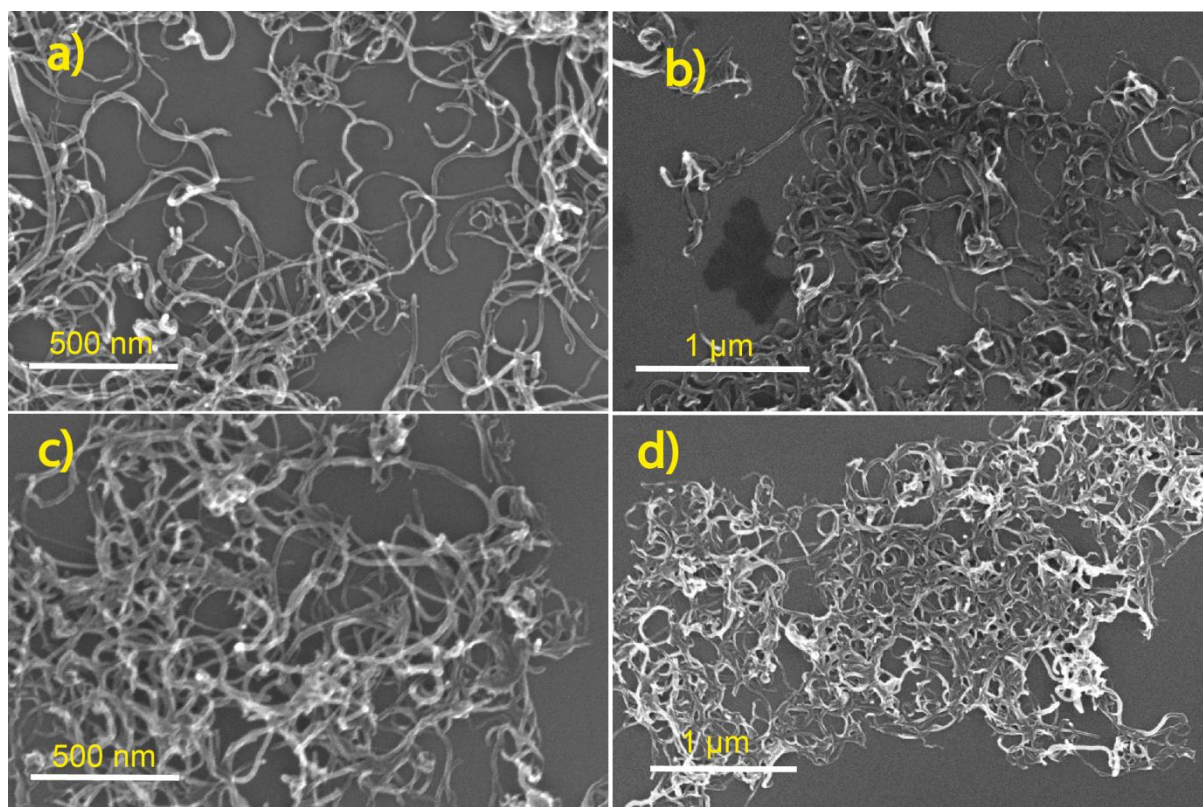


Figure 7. SEM images of a) functionalized CNT, b), c) and d) 1:1, 1:2 and 1:4 CNT-PEDOT composite, respectively.

A CNT-PEDOT composite was also prepared in the ratio of 1:2 using a conventional oxidative method using $\text{Fe}(\text{ClO}_4)_3$ as an oxidizing agent; the SEM images of the same are given in [Figure 8](#). CNTs, in this case, are covered by thick layer PEDOT characterized by the aggregate formation at some locations. This bulk synthesis and thick PEDOT coating result in high inactive PEDOT causing low gravimetric capacitance; the details are discussed in the electrochemical characterization section.

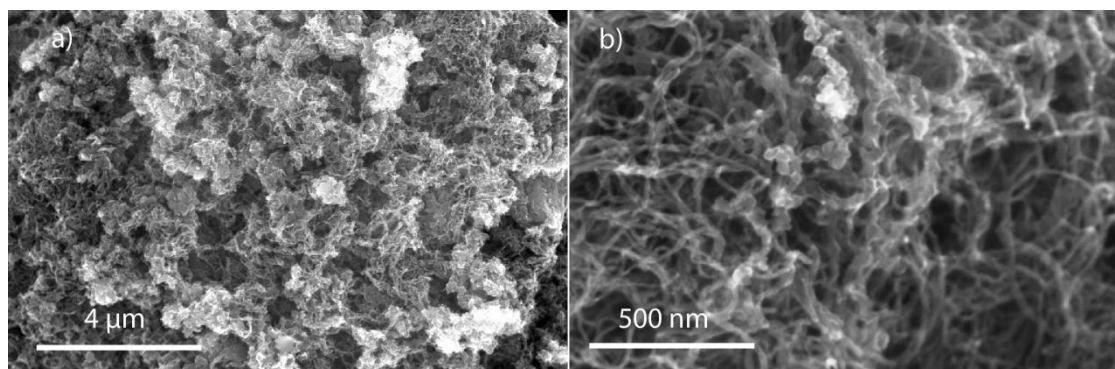


Figure 8. SEM images of CNT-PEDOT composite synthesized through the conventional oxidative method using $\text{Fe}(\text{ClO}_4)_3$ as the oxidising agent.

3.3.6 Energy Dispersive X-ray Spectroscopy (EDS)

The distribution of sulphur on the CNT was analysed by energy dispersive X-ray spectroscopy (EDS) for CNT-PEDOT 1:2 composite. The elemental map of sulphur obtained for the sample area is given in Figure 9. The sample area over which the EDS analysis was carried out is shown in Figure 9a whereas the Figure 9b shows the element map obtained for sulphur. The maps show a uniform distribution of sulphur over the entire selected area. Such a distribution is important for the better charge-storage.

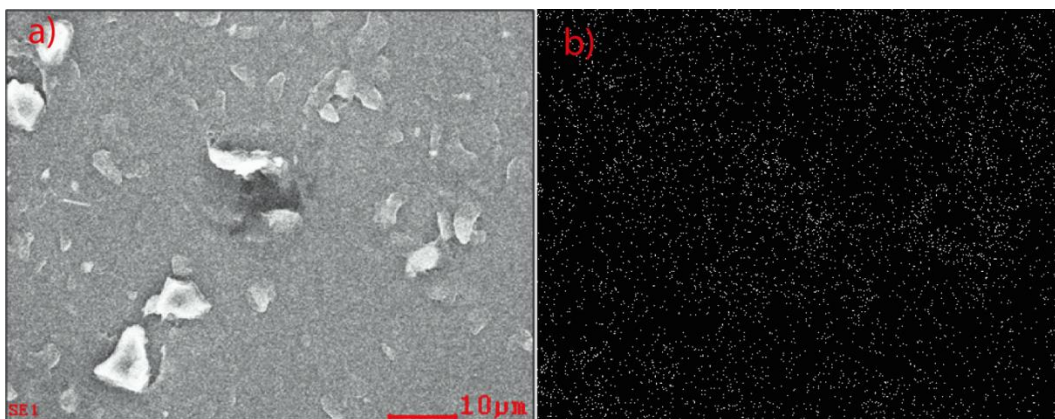


Figure 9. a) SEM image of the area selected for EDS analysis and b) EDS map of sulphur.

3.3.7 BET Analysis

Changes on the surface of CNTs affected by the PEDOT formation were analyzed through gas adsorption measurements. The gas adsorption isotherms of CNT and CNT-PEDOT (1:2) are given in the Figure 10a; both the adsorption isotherms show Type II behavior characteristic for monolayer gas adsorption. Surface area determined from BET calculation for CNTs and CNT-PEDOT (1:2) is 224 and 308 $\text{m}^2 \text{g}^{-1}$, respectively. CNT-PEDOT shows increased surface area due to increased surface roughness and increased radius of the CNT-PEDOT system after the PEDOT coating. Pore size distribution (estimated using NLDFT, non-local density functional theory) profiles of CNT and CNT-PEDOT are given in Figure 10b; the data show highly distributed pore profile for both systems depicting mesoporous structure. Interestingly, pore distribution profiles of both CNT and CNT-PEDOT show similar pore distribution; a logical explanation for this can be the uniform PEDOT covering on the underlying CNTs which is also observed in the FESEM images.

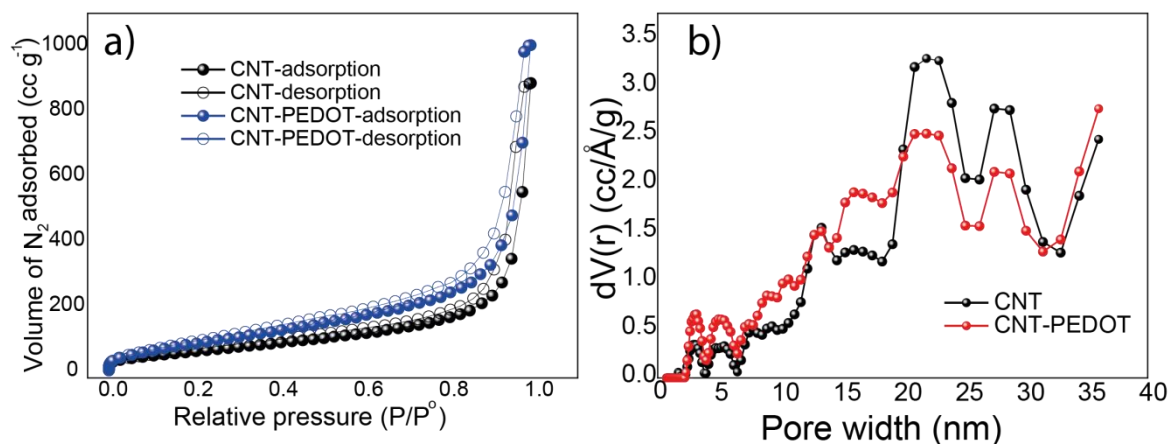


Figure 10. Surface area analysis: a) adsorption isotherms and b) pore size distribution profiles.

3.4 Study of XG-H₂SO₄ Gel Electrolyte

While using PVA-H₂SO₄ as a gel electrolyte for fabricating solid supercapacitor prototype, it was observed that the gel electrolyte was not able to infiltrate inside the electrodes. The reason can be the hydrophobic nature of CNT-PEDOT composite or high viscosity of PVA-H₂SO₄ gel electrolyte. To overcome this problem, a shear thinning material Xanthan gum gel was used, which on the application of shear stress becomes less viscous. XG-H₂SO₄ gel varieties in 2, 3 and 4 wt. % in 1 M H₂SO₄ were prepared. The resistance of the different composition was measured by electrochemical impedance spectroscopy. The conductivity cell comprised of two Pt wires with the diameter of 0.06 cm were placed 0.8 cm apart. The Nyquist plot given in Figure 11 compares the resistance of PVA-H₂SO₄ with resistance observed for three compositions of XG-H₂SO₄. The resistance measured for PVA-H₂SO₄ is 5.1 Ω whereas the resistance values obtained for 2, 3 and 4 wt. % XG-H₂SO₄ are 5.75, 5.70 and 5.65 Ω, respectively. The resistance values obtained is very close to those obtained for PVA-H₂SO₄ showing a difference of only 0.55-0.60 Ω. The close resistance value suggests that it can be used as a gel electrolyte in supercapacitors. Moreover, infiltration of the electrolyte inside the electrode is very important as it defines the electrode-electrolyte interface.

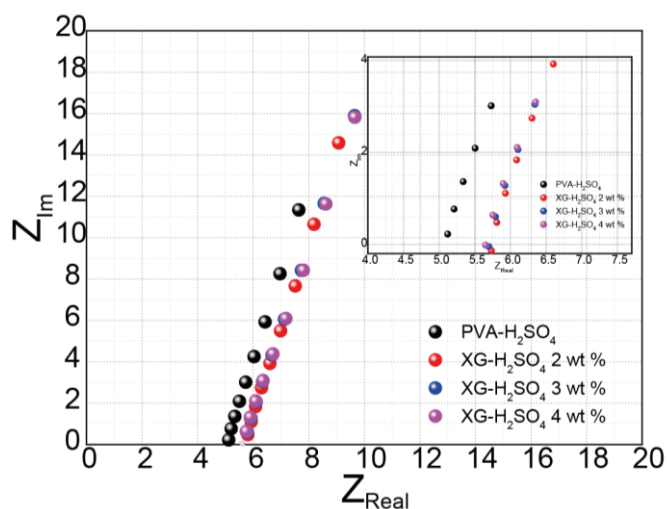


Figure 11. Nyquist plots comparing the impedance of PVA-H₂SO₄ and XG-H₂SO₄ gel electrolytes of different compositions.

3.5 Electrochemical Characterization

A thin layer of PEDOT formed on the surface of CNTs is expected to give better capacitive performance compared to the bulk synthesized CNT-PEDOT composite. Moreover, a high gravimetric capacitance is expected for the hydrothermally synthesized CNT-PEDOT because of the expected low amount of inactive PEDOT. All the liquid-state measurements were performed in 0.5 M H₂SO₄ with Hg/HgSO₄ as a reference electrode.

3.5.1 Solid Supercapacitor Prototype Study

Firstly, solid supercapacitor prototypes were assembled to study the effect of Xanthan gum amount in the XG-H₂SO₄ gel electrolyte; all the test were conducted with 1:2 composite as it is showing the best capacitive performance.

3.5.1.1 Impedance Study of XG-H₂SO₄ Gel as the Electrolyte in Solid Supercapacitor

Initially, we assembled the device using PVA-H₂SO₄ as a gel electrolyte; however, the performance was not up to the expectations. The reason we discovered was the low infiltration of PVA-H₂SO₄ gel electrolyte probably due to the hydrophobic nature of CNT-PEDOT composite (non-dispersible in water). Therefore, a gel electrolyte that has high absorption and infiltration is needed for assembling solid supercapacitor prototype. Xanthan gum-based gels have known to show property of shear thinning which undergo a decrease in viscosity under the external stress,¹⁵ so we prepared 2, 3, and 4 weight percentage Xanthan gum gel electrolytes in 1 M H₂SO₄ (XG-H₂SO₄). During coating of XG-H₂SO₄ gel to the electrode, it experiences a stress which lowers its viscosity. Moreover, the XG-H₂SO₄ gel was

immediately absorbed to the electrode, unlike PVA-H₂SO₄ which remains on the surface. Nyquist plot of the devices fabricated with PVA-H₂SO₄ and different composition of XG-H₂SO₄ is given in [Figure 12a](#). Device assembled using PVA-H₂SO₄ exhibited an ESR of 1.47 Ω ; however, when XG-H₂SO₄ is used as an electrolyte, ESR came down drastically to 0.57 for 2 wt. %, 0.31 Ω for 3 wt. % and 0.45 Ω for 4 wt. %. Five times lower ESR is obtained for the 3 wt. % XG-H₂SO₄ gel electrolyte. Lowest resistance for the 3 wt. % composition shows that it contains the optimum amount of Xanthan gum; a lower amount may not be able to provide enough proton conducting channels whereas high Xanthan amount may hinder in the efficient charge transport. In addition to the ESR, XG-H₂SO₄ shows superior frequency behaviour compared to the conventional PVA-H₂SO₄ gel electrolyte; the corresponding Bode plot showing the frequency behaviour is given in [Figure 12b](#). Evidently, XG-H₂SO₄ has superior frequency behaviour which reaches the ideal capacitive behaviour at a frequency of 238 mHz compared to 33 mHz for PVA H₂SO₄. The superior frequency behaviour shows better electrolyte impregnation, high surface accessibility and easy movement of electrolyte ions for XG-H₂SO₄. Frequency dependence of capacitance has also been analyzed for the devices fabricated with two gel electrolytes; the corresponding plots are given in [Figure 12c](#). We can see the capacitance starts to increase at a higher frequency (38.48 Hz) for XG-H₂SO₄ gel than compared to PVA-H₂SO₄ gel (8 Hz). Also, the capacitance of the device fabricated with the XG-H₂SO₄ gel shows less frequency dependence compared to the PVA-H₂SO₄ gel electrolyte.¹⁶ The close contact and easy diffusion of ions in case of the XG-H₂SO₄ gel electrolyte on the CNT-PEDOT composite surface make this excellent frequency behaviour possible. Moreover, imaginary capacitance as a function of frequency is given in [Figure 12d](#). In the plot, the imaginary capacitance goes to a maximum at a certain frequency, f_0 , and this frequency defines the time constant of the device. The time constant calculated for the device with XG-H₂SO₄ gel electrolyte is 0.27 s ($f_0=3.67$ Hz) while that obtained for the device using PVA-H₂SO₄ gel is 1.3 s. A low value of the time constant shows a very high power capability of the CNT-PEDOT electrode with XG-H₂SO₄ as a gel electrolyte.¹⁶ A high electrochemically active surface area for the hydrothermally synthesized CNT-PEDOT in concurrence with XG-H₂SO₄ gel shows a high power performance made possible by very low ESR as the maximum power obtained from a supercapacitor is a function of ESR ($P_{\max}=V^2/4R$).

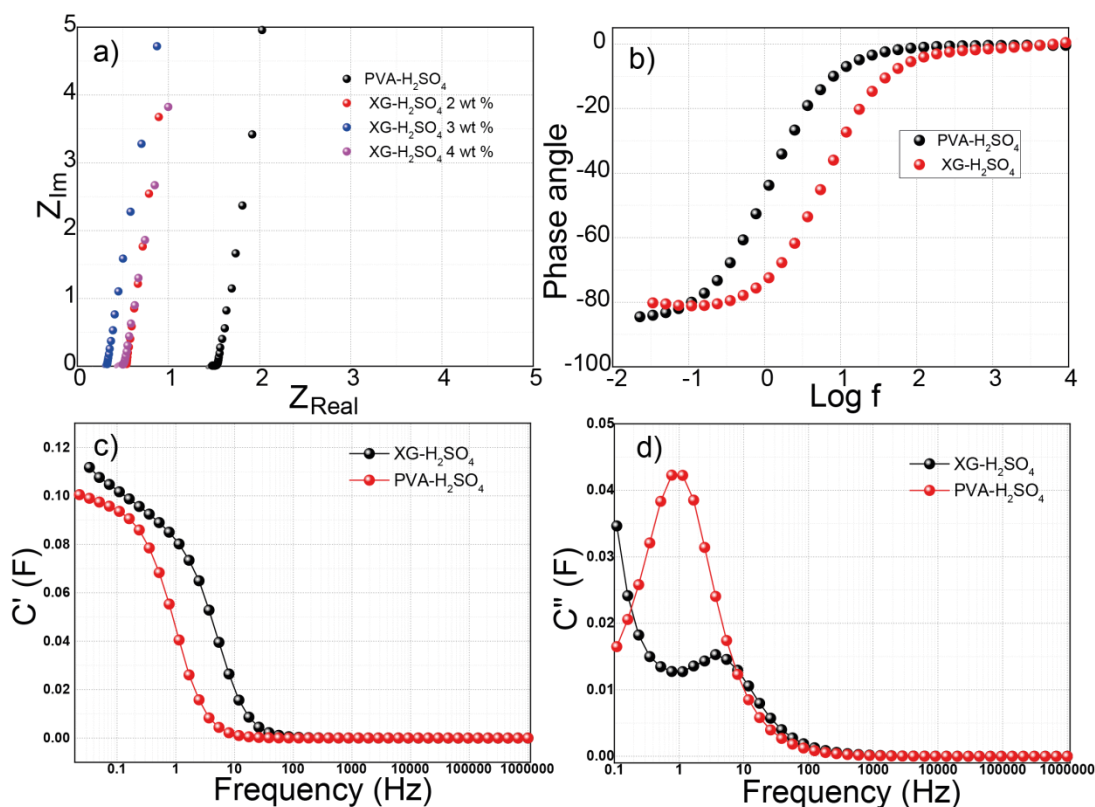


Figure 12. EIS analysis of the gel electrolyte: a) Nyquist plots of the different gel electrolytes, b) Bode plots, c) plots representing the behaviour of the real component of the capacitance with frequency of XG- H_2SO_4 and PVA- H_2SO_4 , d) shows the conduct of the imaginary component of capacitance with frequency.

3.5.1.2 Cyclic Voltammetry

Cyclic voltammograms of the device fabricated with different CNT-PEDOT composites recorded at a scan rate of 10 mV s^{-1} and their comparison with CNTs are given in [Figure 13a](#). Capacitive performance of the CNT film and CNT-PEDOT composites is compared by fabricating solid supercapacitor prototype using 3 wt. % XG- H_2SO_4 as an electrolyte. The area under the CV increases from CNT towards 1:1, 1:2 CNT-PEDOT and then decreases for the 1:4 composite., all the CVs show behaviour typical of a symmetric supercapacitor. CV features of CNT are predominated by EDLC whereas the CV of CNT-PEDOT shows pseudocapacitive behaviour evident from the redox peaks. The area under the CV curve corresponds to the amount of charge stored at the electrode-electrolyte interface; largest area under the curve is observed for CNT-PEDOT 1:2 composite showing its high charge storage capacity compared to the CNT film. The increased charge storage is caused by the high electrochemical surface area of thin PEDOT layer formed on the CNT surface. CVs recorded at increasing scan rates are given in [Figure 13b](#); at higher scan rates, the CV profile retains its

rectangular behaviour even at a scan rate as high as 1000 mV s^{-1} . This analysis implies high rate performance and power capability of the composite which is also evident from the plot of scan rate vs. capacitance shown in Figure 13c. The composite retains 70% of the capacitance; this retention is better than many PEDOT composites reported in the literature.

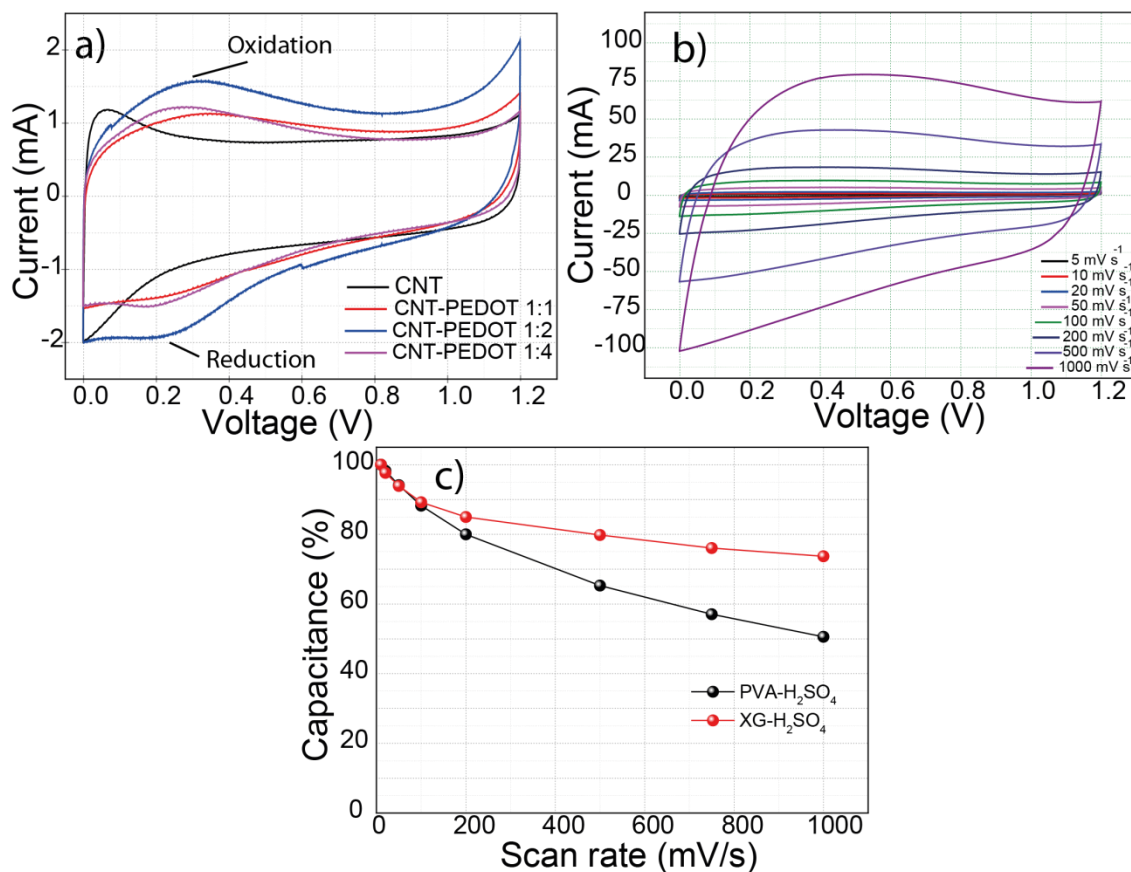


Figure 13. a) CV profiles of the CNT-PEDOT and CNT based solid supercapacitor, b) CVs recorded at increasing scan rates for the CNT-PEDOT solid supercapacitor, c) capacitance retention of the devices fabricated from the CNT-PEDOT composite using PVA-H₂SO₄ and XG-H₂SO₄ as the gel electrolyte.

3.5.1.3 Electrochemical Impedance Spectroscopy

The Nyquist plots recorded for the CNT film and CNT-PEDOT 1:2 solid supercapacitors are given in Figure 14. The ESR obtained for CNT is 0.96Ω while that obtained for the CNT-PEDOT composite is 0.31Ω . The low ESR of the composite compared to CNT results from improved conductivity and facile movement of the electrolyte ions to the electrode surface. Also, frequency behaviour of the composite is better compared to CNT as is evident in the Figure 14. Superior frequency behaviour of CNT-PEDOT shows that motion of electrolyte ions to the electrode is more facile compared to CNTs. Low ESR and better frequency

behaviour of the composite is advantageous for high power capability and rate behaviour. Moreover, Knee frequency (the frequency at which behaviour becomes predominantly capacitive) measured for the composite is very high at 183 Hz which is better than the EDLC supercapacitors.

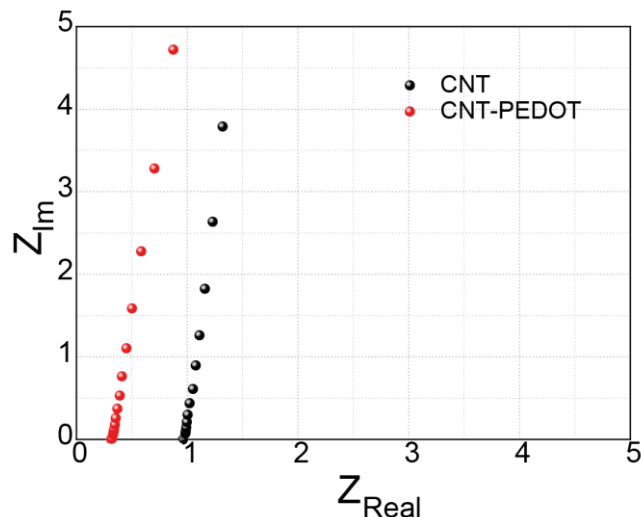


Figure 14. Nyquist plots comparing the impedance of the devices fabricated from CNT and CNT-PEDOT.

3.5.1.4 Galvanostatic Charge-Discharge

To estimate the capacitance, galvanostatic charge-discharge (GCD) was carried out; the corresponding GCD curves measured at a current density of 0.25 mA cm^{-2} are given in [Figure 15](#). In the curve, the charging time for the composite is high due to the high capacitance. The GCD profiles are typical of the symmetrical supercapacitor. CNT exhibits only double layer capacitance and the capacitance measured for CNT from [Figure 15](#) is 200 mF cm^{-2} . The substantially good capacitance of CNTs can be attributed to the application of XG- H_2SO_4 gel electrolyte which due to its shear thinning properties can infiltrate deeper and impregnate more surfaces compared to other gel electrolytes. However, the capacitance increases when the PEDOT is coated on the CNTs. The capacitance measured for the 1:1 composite is 278 mF cm^{-2} . An enhancement in capacitance is observed for the 1:2 composite which increases to 336 mF cm^{-2} , this increased capacitance can be due to increased PEDOT coverage. However, the capacitance decreases for the 1:4 composite to 268 mF cm^{-2} which can be understood by considering the formation thick PEDOT layer over the CNTs; hence, it is possible that inner PEDOT surface is not accessible to ions leading to reduced specific capacitance.

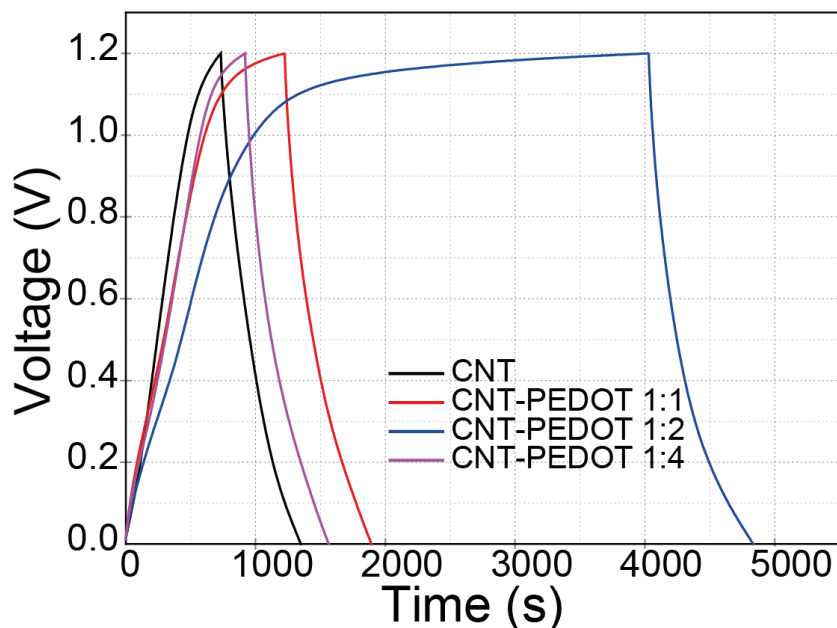


Figure 15. GCD curves of CNT and CNT-PEDOT.

The volumetric capacitance of the device (with a thickness of 0.02 cm and volume 0.0156 cm^3) is measured to be 8.5 F cm^{-3} . Moreover, the device showed high power density of 74 W cm^{-3} at an energy density of 1.7 mWh cm^{-3} ; such impressive performance regarding power density is made possible by the seamless structurally aligned PEDOT on CNTs that result in very low ESR.

3.5.1.5 Durability Test

Cyclic performance of the device fabricated from CNT-PEDOT 1:2 composite in which XG- H_2SO_4 is used as a gel electrolyte was carried out at a current density of 4 mA cm^{-2} . The corresponding plot is given in Figure 16. As shown in the figure, after 11000 cycles, the device retains 60 % of the initial capacitance with almost 100 % efficiency. The reduction in capacitance can be ascribed to the loss of water from the electrolyte caused by the heat generation during the charge-discharge process. Better heat dissipation can help increase the capacitance retention during long cycling.

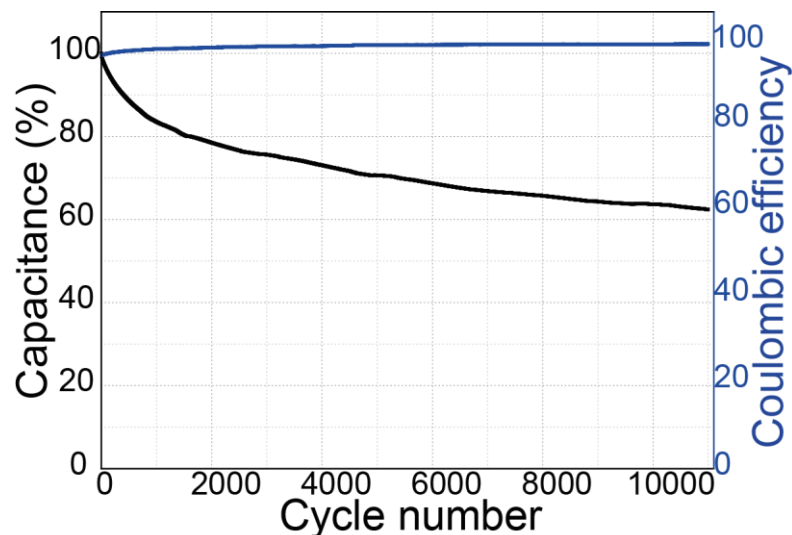


Figure 16. Durability test of CNT-PEDOT 1:2 device carried out at a current density of 4 mA cm^{-2} .

3.6 Conclusion

In this chapter, a hydrothermal method is proposed for the synthesis of ultrathin PEDOT on the surface of CNTs. In this method, surface functional groups incorporated through acid functionalization causes the oxidation of EDOT monomer which subsequently forms PEDOT on the surface of CNTs in a seamless aligned manner which has remained elusive. Formation of PEDOT is confirmed through running control experiments, IR spectroscopy, XRD, and XPS. Also, a new shear thinning gel electrolyte, Xanthan gum- H_2SO_4 (XG- H_2SO_4) is prepared which could be impregnated to a hydrophobic surface like CNT-PEDOT composite prepared here. The performance of the XG- H_2SO_4 electrolyte is compared with widely used PVA- H_2SO_4 gel electrolyte and the former has emerged as a clear winner. Application of this novel shear thinning gel electrolyte in the device fabricated with CNT-PEDOT 1:2 composite results in very low ESR of 0.31Ω in a solid supercapacitor prototype. The device could show high volumetric power density of 74 W cm^{-3} with an energy density of 1.7 mWh cm^{-3} .

3.7 References

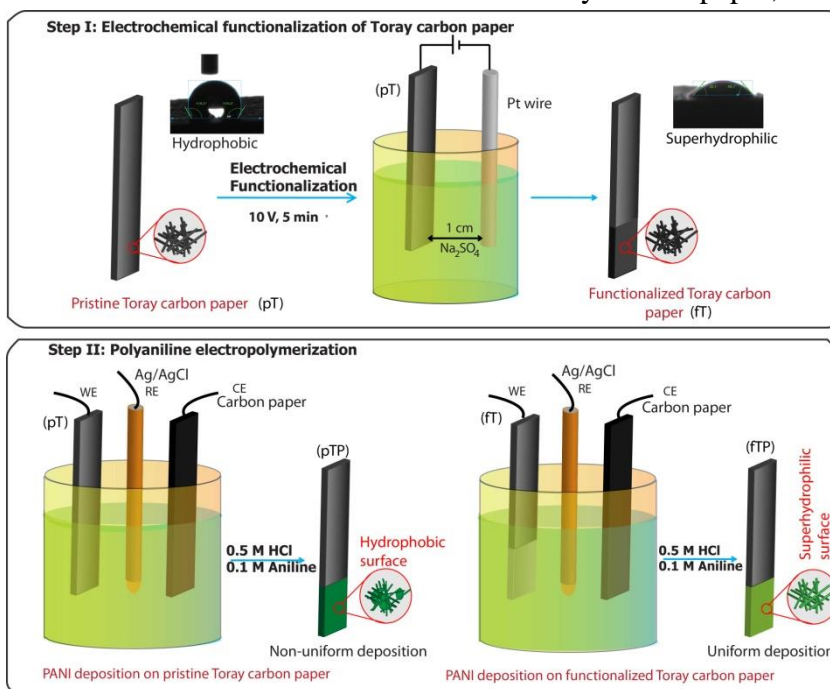
1. K. Lota, V. Khomenko and E. Frackowiak, *Journal of Physics and Chemistry of Solids*, 2004, **65**, 295-301.
2. D. S. Ginley and C. Bright, *MRS Bulletin*, 2011, **25**, 15-18.
3. G. D. a. M. Leclerc, *Macromolecules*, 1991, **24**, 455-459.
4. A. M. Bryan, L. M. Santino, Y. Lu, S. Acharya and J. M. D'Arcy, *Chemistry of Materials*, 2016, **28**, 5989-5998.
5. P.-W. Sze, K.-W. Lee, P.-C. Huang, D.-W. Chou, B.-S. Kao and C.-J. Huang, *Energies*, 2017, **10**, 716.
6. L. Ran, C. Seung Il and L. Sang Bok, *Nanotechnology*, 2008, **19**, 215710.
7. X. Zhang, J.-S. Lee, G. S. Lee, D.-K. Cha, M. J. Kim, D. J. Yang and S. K. Manohar, *Macromolecules*, 2006, **39**, 470-472.

8. B. Anothumakkool, R. Soni, S. N. Bhange and S. Kurungot, *Energy & Environmental Science*, 2015, **8**, 1339-1347.
9. M. Mumtaz, A. d. Cuendias, J. L. Putaux, E. Cloutet and H. Cramail, *Macromolecular Rapid Communications*, 2006, **27**, 1446-1453.
10. J. M. D'Arcy, M. F. El-Kady, P. P. Khine, L. Zhang, S. H. Lee, N. R. Davis, D. S. Liu, M. T. Yeung, S. Y. Kim, C. L. Turner, A. T. Lech, P. T. Hammond and R. B. Kaner, *ACS Nano*, 2014, **8**, 1500-1510.
11. O. P. a. V. Sergeev, *Scientific Journal of Riga Technical University Material Science and Applied Chemistry*, 2010, **21**, 51-54.
12. A. Cao, C. Xu, J. Liang, D. Wu and B. Wei, *Chemical Physics Letters*, 2001, **344**, 13-17.
13. T. Y. Kim, C. M. Park, J. E. Kim and K. S. Suh, *Synthetic Metals*, 2005, **149**, 169-174.
14. T. Y. Kim, J. E. Kim and K. S. Suh, *Polymer International*, 2006, **55**, 80-86.
15. S. J. Park, K. Yoo, J.-Y. Kim, J. Y. Kim, D.-K. Lee, B. Kim, H. Kim, J. H. Kim, J. Cho and M. J. Ko, *ACS Nano*, 2013, **7**, 4050-4056.
16. P. L. Taberna, P. Simon and J. F. Fauvarque, *Journal of The Electrochemical Society*, 2003, **150**, A292.

Chapter-4

Enhancing the Electrochemical Surface Area through Induction of Superhydrophilicity and Structural Alignment in Polyaniline to Achieve High Capacitance

Polyaniline (PANI) as a pseudocapacitive material has a very high theoretical capacitance of 2000 F g^{-1} . However, its practical capacitance has been limited by low electrochemical surface area (ESA) and unfavourable wettability toward aqueous electrolytes. This work deals with a strategy wherein the high ESA of PANI has been achieved by the induction of superhydrophilicity together with the alignment of PANI exclusively on the surface of carbon fibers as a thin layer to form a hybrid assembly. Superhydrophilicity is induced by electrochemical functionalization of the Toray carbon paper, which further induces



superhydrophilicity to the electrodeposited PANI layer on the paper, thereby ensuring a high electrode–electrolyte interface. The Toray paper is electrochemically functionalized by the anodization method, which generates a highly active electrochemical surface as well as greater wettability (superhydrophilic) of the carbon fibers. Because of the strong interaction of anilinium chloride with the hydrophilic carbon surface,

PANI is polymerized exclusively over the surface of the fibers without any appreciable aggregation or agglomeration of the polymer. The PANI-Toray paper assembly in the solid-state prototype supercapacitor could provide a high gravimetric capacitance of 1335 F g^{-1} as well as a high areal capacitance of 1.3 F cm^{-2} at a current density of 10 A g^{-1} .

Content of this chapter is published in the following article:

ACS Appl. Mater. Interfaces, 2018, 10, 676–686.

<https://pubs.acs.org/doi/10.1021/acsami.7b15534>

Reproduced by permission of ACS Applied Materials & Interfaces.

4.1 Introduction

Polyaniline (PANI), a conducting polymer, has many advantageous properties when used as a capacitive material. High capacitance (2000 F g^{-1}),¹ ease of synthesis, low cost, good electronic conductivity,² and environmental benignity make it a suitable material for supercapacitors. However, low practical capacitance, poor rate capability,^{3, 4} and high equivalent series resistance⁵ are some pertaining issues, which hinder its application in commercial supercapacitors. PANI falls under the category of pseudocapacitors where the redox transition between the different reduced and oxidized states of the material results in charge storage.¹ Basically, PANI has three distinct oxidation states; the completely reduced state or leucoemeraldine, the half-oxidized form or emeraldine, and the fully oxidized form or pernigraniline.¹ The transition among these redox states results in charge storage, and thus, a highly active electrochemical surface and facile movement of electrolyte ions are necessary for high rate capability in PANI. For the supercapacitor utilizing aqueous electrolytes as in the case of PANI, the wettability of the surface plays a highly important role in the device performance, as favourable wettability (exhibited by hydrophilic or superhydrophilic surfaces) ensures a high electrode-electrolyte interface. There are a number of strategies to increase the ESA of the material. Some of which include the creation of defects in the material,⁶ incorporating hydrophilic functional groups on the surface,⁷ or morphology manipulation. The wettability of the conducting polymers has been manipulated by the incorporation of polymers such as dextran in poly(3-hexylthiophene),⁸ by modifying the surface morphology,⁹ or by the anion exchange in the polymer backbone.¹⁰ However, all these methods result in the decrement in the conductivity of the active material, which further reduces the rate performance of the supercapacitor. Therefore, an appropriate strategy is needed, which increases the wettability and ESA of the capacitive material without affecting its conductivity. From the above discussion, it is clear that favourable surface wettability, which ultimately leads to high ESA, is a prerequisite for achieving high capacitance and rate performance. At the same time, it is utmost important to achieve high electronic conductivity in the system for allowing it to achieve high power density. In this chapter, a strategy is demonstrated in which the wettability of PANI is modified by polymerizing it on the superhydrophilic conducting surface to accomplish a high ESA without affecting its electronic conductivity and other physical properties. At the same time, a few nanometers thin PANI film is achieved, which reduces the amount of inactive PANI that is unavoidable in thicker PANI coatings.

4.2 Experimental Section

4.2.1 Materials

Sodium sulphate, hydrochloric acid, and sulphuric acid were procured from Thomas-Baker. Polyvinyl alcohol (PVA) and aniline were purchased from Sigma-Aldrich.

4.2.2 Electrochemical Functionalization of Toray Carbon Paper

Firstly, a Toray paper with dimensions of 5 cm in length and 1 cm in breadth was cut. Only 1 cm² area was exposed to the electrolyte while rest is covered with Scotch tape. 0.1 M aq. Na₂SO₄ was used as the electrolyte. For functionalization, the Toray paper was made as the anode while a Pt wire was used as a cathode. The two were placed in a conventional two-electrode electrochemical cell. The distance between the electrodes was maintained at 1 cm. Subsequently, a constant potential of 10 V was applied for 5 min. using a potentiostat. This functionalized Toray paper is called as fT; the changes on the surface accrued after functionalization is given in [Figure 1](#).



Figure 1. Digital photographs of a) pristine Toray carbon paper (pT); b) functionalized Toray carbon paper (fT). After functionalization, the surface of the Toray paper turns dark which can be seen in the above images.

4.2.3 Electrodeposition of Polyaniline

PANI was electropolymerized through a galvanostatic and a potentiostatic method. For electropolymerization, 0.1 M aniline was used as a monomer while 0.5 M HCl, H₂SO₄, camphorsulphonic acid, and phytic acid were tested as the supporting electrolyte. In the case of HCl, Ag/AgCl was used as a reference electrode; for sulphuric acid and camphor sulphonic acid, Hg/HgSO₄ was employed as the reference electrode. A Pt quasi-reference electrode was

used in the case of phytic acid. In the galvanostatic mode, current densities of 2, 5 and 8 mA cm⁻² were employed while the potentiostatic polymerization was carried out at 800 mV. After polymerization, the electrodes were dried under an IR lamp which was subsequently washed with water and dried again. The amount of PANI deposited was maintained by controlling charge which was calculated using Faraday's law. PANI deposited on pT and fT is termed as pTP and fTP, respectively. The digital pictures of pTP and fTP are given in [Figure 2](#).

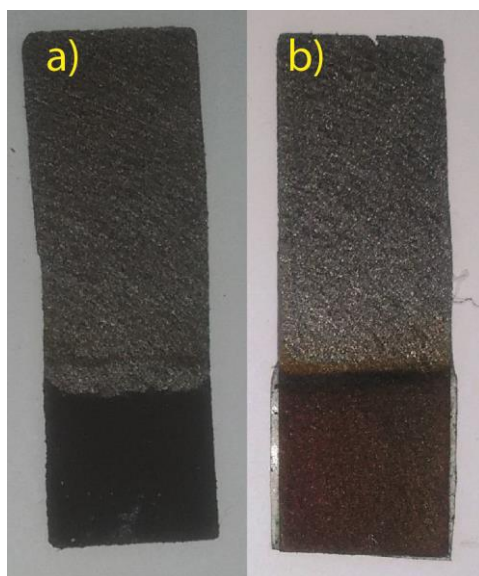


Figure 2. a) The PANI polymerized on the pristine Toray paper (pTP); PANI forms a thick coating on the upper surface and b) the digital image of the PANI polymerized over the functionalized Toray paper (fTP). This image shows a marked difference from the image a); thick PANI layer cannot be seen for fTP unlike pTP.

4.2.4. Determination of Electrochemical Active Surface Area (ESA)

4.2.4.1 ESA Determination of pT and fT

Randles-Sevcik Method: Electrochemical active surface area of pT and fT was determined by Randles-Sevcik¹¹ equation, $I_p = (2.69 \times 10^5) n^{3/2} A D_0 C v^{1/2}$ where I_p is the peak current (A), n is the number of the electrons involved in the redox reaction, A is the area of the electrochemical active surface (cm²), D_0 is the diffusion coefficient (cm² s⁻¹); $D_0 = 6.30 \times 10^{-6}$ cm² s⁻¹, v is the scan rate (V s⁻¹) and $C = 10$ mM (Fe^{2+/3+}).

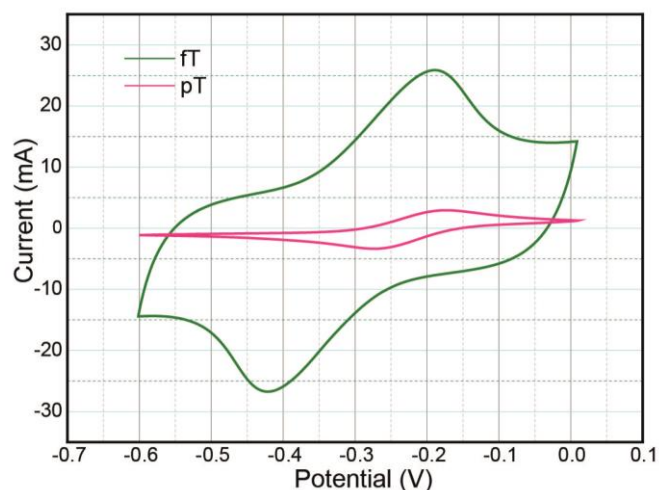


Figure 3. Cyclic voltammograms of pT and fT recorded at a scan rate of 50 mV s^{-1} in the $\text{Fe}^{2+}/\text{Fe}^{3+}$ couple for the electrochemical surface area measurement.

In a typical experiment, CVs at a scan rate of 50 mV s^{-1} were recorded in 1 M KCl containing $10 \text{ mM Fe}(\text{CN})_6^{3-}$ as the electrolyte in a three-electrode cell where fT and pT were made as the working electrode, a grafoil carbon sheet as a counter electrode, and the Pt wire as a quasi-reference electrode. From the CV, the oxidation peak currents were measured and fit into the Randles-Sevcik equation. The corresponding CVs are given in Figure 3. The ESA measure for pT is 1.77 cm^2 which increased to 15.71 cm^2 for fT.

4.2.4.2 Double Layer Capacitance (C_{dl}) Determination of pTP and fTP

For calculating the double layer capacitance, CVs were recorded in the potential range where the double layer behaviour is predominant. The CVs were recorded at increasing scan rates.¹¹ The peak current in the voltammograms was plotted against the potential scan rate. The slope of the curve obtained gives the double layer capacitance, $i_c = vC_{dl}$. The corresponding plots are given in Figure 4. The slope of the curve gives the double layer capacitance that is formed on the electrode-electrolyte interface. This double layer capacitance can be approximated with the electrochemically active surface area of the electrode. C_{dl} was measured for the two electrodes by scanning them to the potential range of -0.45 to -0.35 V for pTP and -0.40 to 0.30 V for fTP, based on how the double-layer charging takes place. The C_{dl} measured for pTP is 123 mF cm^{-2} , whereas that for fTP is 295 mF cm^{-2} , which authenticates the availability of 2.4 times higher ESA for fTP compared to pTP.

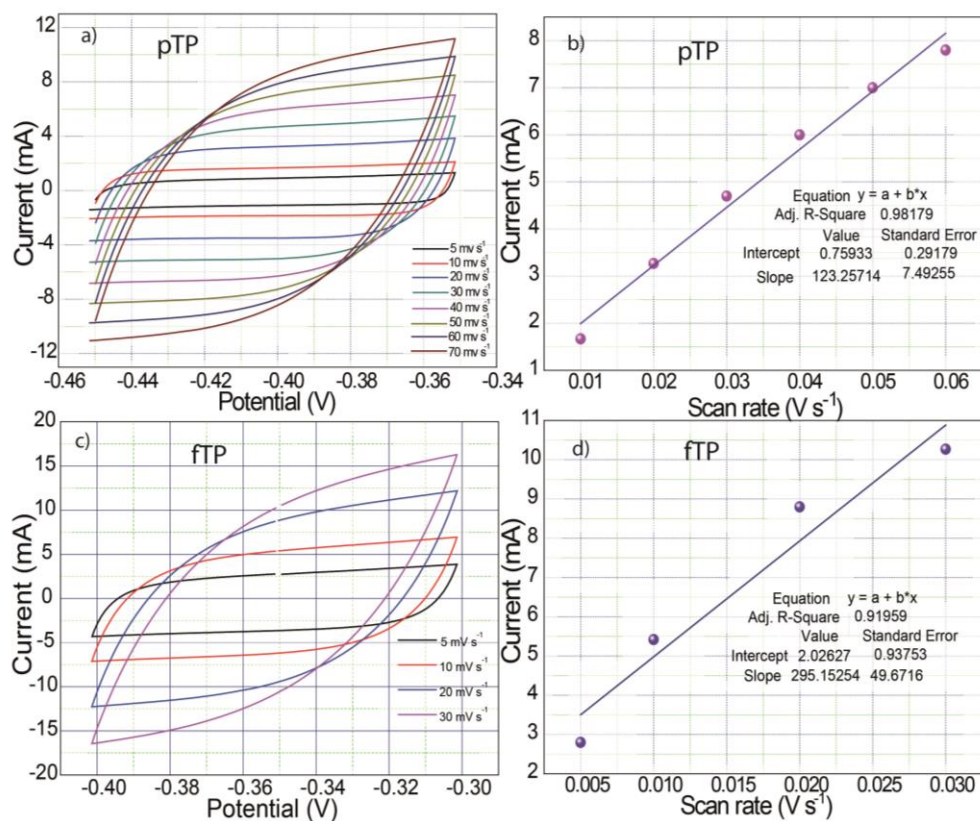


Figure 4. Double layer capacitance determination of pTP and fTP. a) CVs of pTP recorded at the scan rates of 5, 10, 20, 30, 40, 50, 60, and 70 mV s⁻¹ in the double layer region; b) charging currents measured at 0.40 V from Figure 4a are plotted against the respective scan rates; c) and d) show the CVs at the scan rates of 5, 10, 20, and 30 mV s⁻¹ and the charging current (recorded at -0.35 V) vs. scan rate, respectively.

4.2.5. Fabrication of Solid Supercapacitor Prototype

A thin layer of PVA-H₂SO₄ gel electrolyte was applied to an active area of 1 cm² of the working electrodes. The electrodes were kept under ambient condition for 6 h to allow excess water to evaporate. Subsequently, the working electrodes were sandwiched with a Celgard membrane as a separator which was pre-treated with PVA-H₂SO₄ gel electrolyte.

4.2.6 Characterization

Contact angle measurement was performed on KRÜS drop shape analyzer. SEM analysis was carried out on a Quanta and Nova SEM 450 instrument. XRD analysis was performed in RigakuSmartLab diffractometer with Cu K α radiation ($\lambda=1.5406 \text{ \AA}$) at a scan rate of 2° min⁻¹. XPS spectra were recorded on VGMicrotechmultilab ESCA 3000 spectrometer. BET surface area and pore size distribution were determined using ultra-pure N₂ on Qunatachrome Quadrasorb automatic volumetric instrument. A Bio-logic SP-300 PG Stat was employed for

all the measurements including the galvanostatic charge/discharge measurements. Electrochemical data were processed with EC-Lab software V10.44. Sheet resistance was calculated with a four-probe conductivity meter having a probe spacing of 0.2 mm.

4.3 Result and Discussion

4.3.1 Characterization of Functional Groups Incorporated after Anodization of Toray Carbon Paper

4.3.1.1 IR spectroscopy

Application of the potential results in the incorporation of $-\text{COOH}$ functional groups on the carbon fibers, which is ascertained through the IR spectrum of fT (Figure 5). The spectrum shows the stretching frequency corresponding to the carboxylic ($-\text{C}=\text{O}$) group at 1730 cm^{-1} , which is absent in the pristine Toray paper.

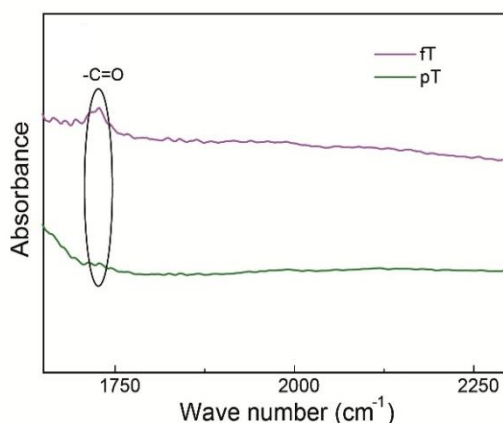


Figure 5. Infrared (IR) spectra of the pristine Toray carbon paper (pT) and functionalized paper (fT)

4.3.1.2 XPS Spectroscopy

The quantification of oxygen has been carried out with the help of XPS (Figure 6). The percentage of oxygen in pT is determined to be 5.36%, which after functionalization, increases to 18.45%. These results are further supported by the elemental analysis (C, O analysis). The oxygen content in pT is calculated to be 3.53%, which increases to 20.23% in the case of fT. This corresponds to an enhancement in the oxygen concentration by 16.7% after anodization, which is in close agreement with the X-ray photoelectron spectroscopy (XPS) data.

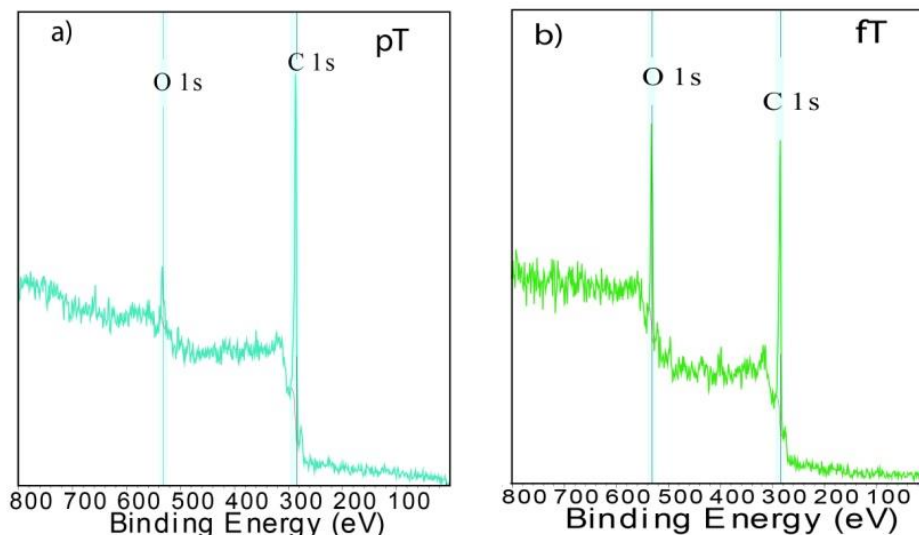


Figure 6. a) XPS survey spectrum of pT; b) survey spectrum of fT. The survey spectrum of fT shows high intensity for O 1s compared to pT. Further, the area under the O 1s peak is higher in the case of fT than pT which infers to the high concentration of the oxygen functional groups for fT.

4.3.2 Contact Angle Measurement and Wettability Analysis

4.3.2.1 Pristine Toray Carbon Paper and Functionalized Toray Carbon Paper

Electrochemical functionalization drastically changes the surface composition of the carbon fibers, and hence, it is expected to affect the wettability of the polymerization solution toward the carbon fibers. The changes in wettability were analyzed through contact angle measurements. The water contact angle measured for pT is 119° , which indicates an unfavourable surface for wetting (Figure 7a). On the other hand, fT becomes highly hydrophilic (superhydrophilic) with improved wettability. However, the water contact angle in the case of fT could not be measured because of instantaneous absorption of the water droplet by the paper. Subsequently, the PVA- H_2SO_4 gel (which has been used as the electrolyte for the supercapacitor fabrication) was used in place of water, and the contact angle so measured was found to be 48° (Figure 7c); the image in the inset of Figure 7c shows 0° contact angle for the fT–water interface. The PVA- H_2SO_4 gel electrolyte is completely absorbed in the case of fT, unlike pT where the electrolyte remained unabsorbed even after a long time.

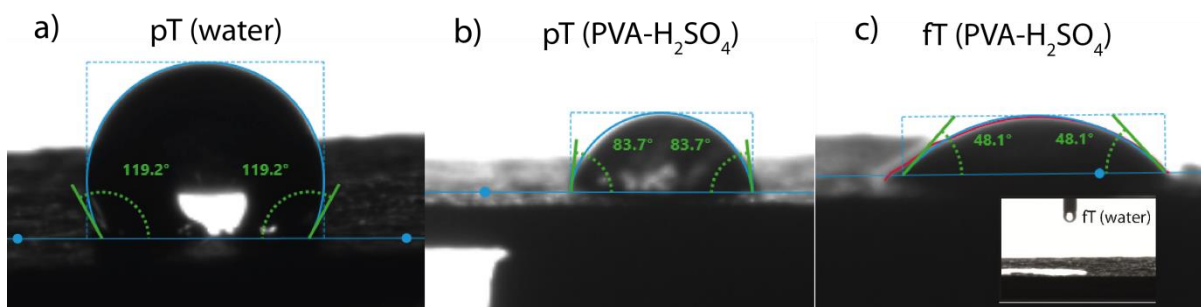


Figure 7. a), b) Represent the contact angle measurement of pT carried out with water and poly(vinyl alcohol) (PVA)-H₂SO₄ gel, respectively; c) contact angle measurement of fT with the PVA-H₂SO₄ gel electrolyte.

4.3.2.2 pTP and fTP

One important outcome of the electrochemical functionalization is that, it not only increases the wettability of the Toray paper but also enhances the hydrophilicity of fTP as a whole. This has been confirmed by the contact angle data shown in [Figure 8](#). PVA-H₂SO₄ contact angle measured for pTP is 62.0°, whereas, for fTP, the value decreases to 28.8°. In fTP, the gel electrolyte undergoes complete absorption, and the surface becomes superhydrophilic. Images representing the contact angle measurements depicting water wettability at higher deposition times of 26 and 34 min are given in [Figure 9](#). At higher deposition times, the PANI coating on the carbon fiber surface will be thicker, and this will cover the entire fiber surface by decreasing the possibility of exposing the fT surface.

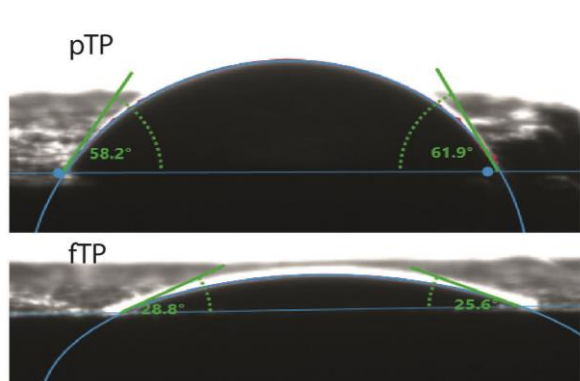
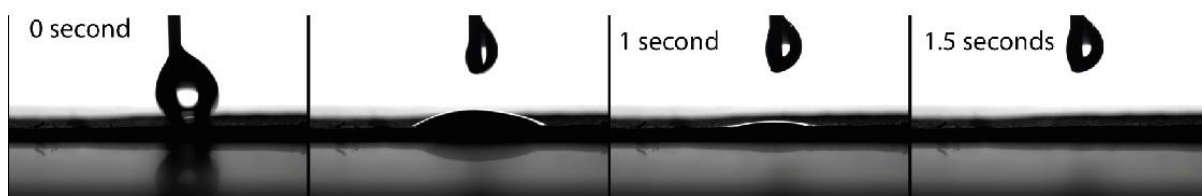


Figure 8. Wettability of pTP and fTP through PVA-H₂SO₄ contact angle measurement.

Contact angle measurements show immediate absorption of water within 1.5 s even in the electrode with higher deposition time. The contact angle measured here is 0° for all samples. The contact angle measurement at higher PANI loading confirms that the change in wettability is not because of the exposed functional groups in case the carbon fibers are not covered completely by PANI, but due to the interaction of the underlying modified carbon

surface and PANI. Development of a positive charge on polymer chains caused by the electron charge density transfer from nitrogen of the polymer to oxygen present in the carbon paper (as observed from the XPS analysis) is expected to be responsible for the enhancement in the hydrophilicity of PANI. The interfacial tension between PANI and the aqueous electrolyte decreases because of the strong interaction of the oxygen atoms of water molecules with the positive charge density of the polymer chain. Because of the superhydrophilic nature of the surface, water fails to form a drop on the surface, and hence, its contact angle could not be measured.

a) Deposition time- 26 minutes



b) Deposition time- 34 minutes

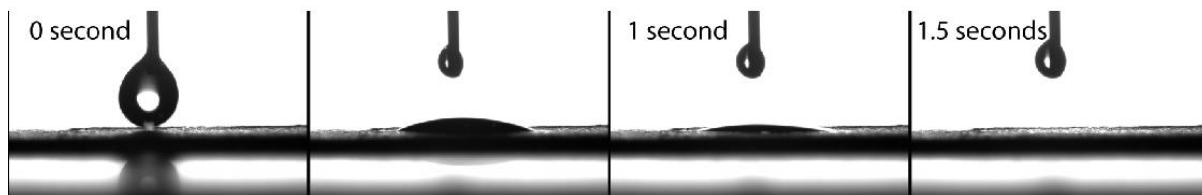


Figure 9. a) and b) represent the images recorded during the contact angle measurement for FTP when the deposition time for PANI was 26 minutes and 34 minutes, respectively.

4.3.3 Electron Microscopy Analysis

Changes, if any, in the morphology were investigated with the help of SEM on pT (Figure 10a) and fT (Figure 10b). Long tubes with smooth surfaces forming the entangled network can be seen in Figure 10a for pT. Further, the same characters can be observed for fT in Figure 10b without any structural changes. Hence, electrochemical functionalization keeps the morphology intact, which is necessary for being used as a template for deposition of the PANI layer. A thick PANI coating is evidently visible in the case of pT. However, the nature of PANI coating is apparently different in the case of fT, where the polymer deposition is well-extended deep inside the carbon fibers of the Toray paper by avoiding the thick patches, as observed in the case of pT. Polymerization at a constant current (current density of 2 mA cm^{-2}) results in a uniform coating of PANI over the tubes (Figure 10c) compared to a case when the polymerization was carried out at a constant potential of 800 mV, which resulted in the

formation of large aggregates of the polymer on the surface (Figure 10e). Further, in the high-resolution SEM image shown in Figure 10d (constant current), a porous polymer structure is visible. Figure 10f shows the carbon fibers with relatively less polymer coverage, as most of the PANI forms large aggregates, which are concentrated at a few places. This change in the polymer alignment can be ascribed to the low rate of polymerization in the galvanostatic method (polymerization time of 17 min 24 s) compared to the potentiostatic method (polymerization time of 408 s). Slow polymerization is essential for achieving a uniform coating. This is because, when the process is slow, the system gets ample time for the monomer to diffuse from the bulk for maintaining a constant concentration in the diffusion layer and also over the carbon fibers, leading to a condition that is favourable for attaining a uniform polymer coating. Considering the above, the constant current method was selected as the polymerization technique in this study.

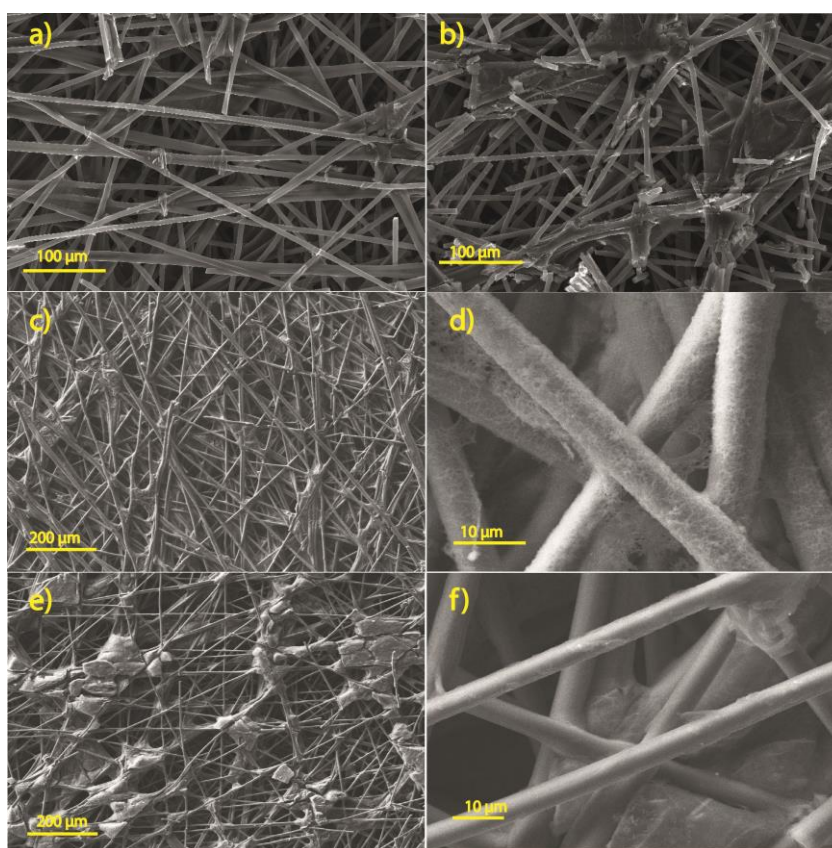


Figure 10. Scanning electron microscopy (SEM) analysis: a) field emission SEM (FESEM) image of pT; b) FESEM image of the Toray paper after functionalization (fT); c) low-magnification SEM image of PANI polymerized over fT (fT-PANI, designated as fTP) where polymerization is carried out at a constant current of 2 mA cm^{-2} ; d) high-resolution FESEM image of fTP where the PANI polymerization is performed by the constant current method (2 mA cm^{-2}); e) SEM image of fTP where

PANI is polymerized at a constant potential of 800 mV; f) FESEM image of PANI (constant potential method).

The effect of functionalization on the growth of PANI over the fibers was studied by the SEM analysis of pTP and fTP. SEM images of pTP are shown in [Figure 10a, b](#). As is evident from the images, PANI forms a thick coating on the surface of the carbon fibers. Moreover, the open spaces are blocked, which will further reduce the ESA of the polymer and will hinder the electrolyte infiltration. Also, the polymer coating is non-uniform with several cracks, which would cause high resistance due to the higher density of grain boundaries. On the other hand, in the case of fTP, the polymerization essentially takes place on the surface of the fibers, as shown in [Figure 10c, d](#).

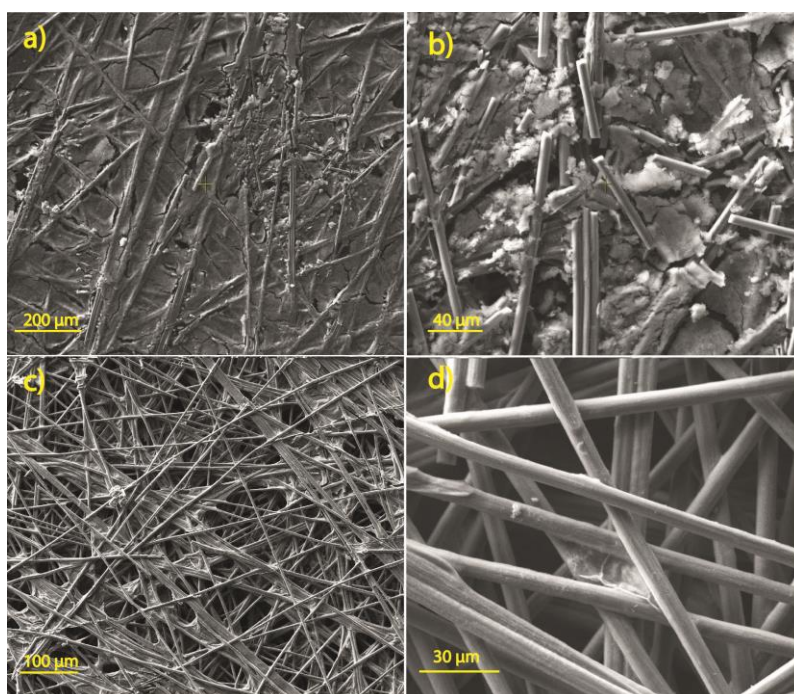


Figure 11. SEM image of PANI polymerized over pT (pT-PANI, designated as pTP) and fTP where the polymerization is carried out at the constant current mode: a), b) represent the images of pTP at low and high magnification, respectively; c), d) depict the morphology of fTP at low and high magnification, respectively.

To support the SEM results, the thickness measurement of the PANI layer on the surface in fTP and pTP was carried out by the TEM analysis; the corresponding TEM images are given in [Figure 12](#). The thickness measured for fT measured from a single fiber is 315 nm ([Figure 12a](#)), whereas the thickness measured for fTP is 322 nm ([Figure 12b](#)), which suggests the formation of a 7 nm-thick PANI layer on the surface of the fiber in fTP. Similarly, the

thickness of pTP obtained from TEM (Figure 12c) is 622 nm, which gives the approximate thickness of the PANI layer to be 307 nm. Thus, a very thick PANI deposition is obtained for the unfunctionalized Toray surface, which further limits its electrochemically active surface area, whereas a thin PANI layer (just 7 nm) achieved in fTP ensures a low amount of inactive PANI. The alignment of PANI exclusively over the fibers is caused by the superhydrophilicity of the fibers, which increases the impregnation by the monomer not only on the surface but also in the inner spaces. This arrangement leaves the pores and vacant spaces intact, thus facilitating an unrestricted movement of the electrolyte ions.

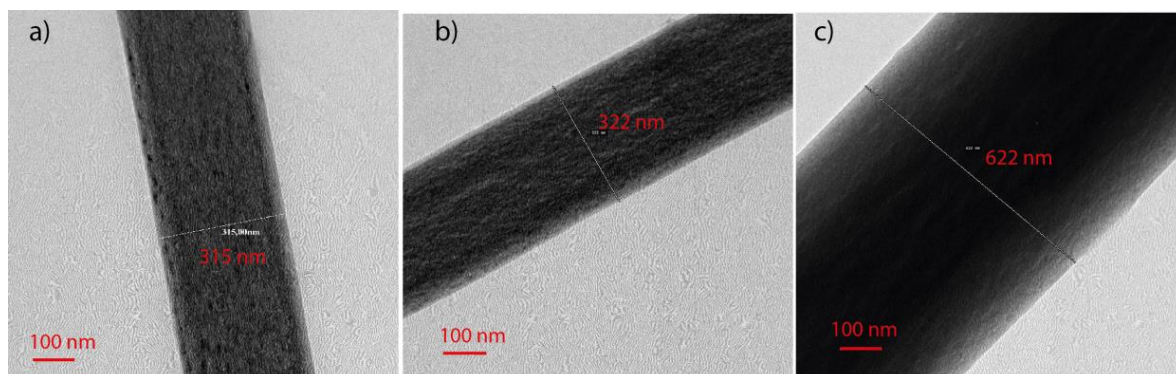


Figure 12. TEM analysis. a) TEM image of fT; b) TEM of fTP; TEM image of pTP.

4.3.4 Brunauer-Emmett-Teller (BET) Analysis

Brunauer-Emmett-Teller (BET) analysis of fT, fTP, and pTP was also carried out to understand the surface properties; the adsorption isotherm and pore size distribution profiles of the three samples are given in Figure 13. The adsorption isotherms of all samples (Figure 13a) show type VI behaviour, which is common for nonporous solids with a uniform surface.¹² The adsorption isotherm of fT in the relative pressure range of 0.1-0.3 shows very less gas adsorption, inferring its low surface area and nonporous nature. Moreover, it does not show any prominent pore structure, which is clear from the pore size distribution profile presented in Figure 13b. The low surface area can be understood from the fact that it is a network of solid carbon fibers, which entangle together to form a solid network; the only surface available for gas adsorption is the outer surface of the carbon fibers. The multipoint BET surface area of fT is very low at $55 \text{ m}^2 \text{ g}^{-1}$, which again indicates its nonporous nature. Adsorption isotherms recorded for pTP and fTP also show features similar to fT. In the case of pTP, a small anomaly, that is, a sudden increase in the gas adsorption or a crossover is observed near the saturation point. This anomaly seems to have been caused by instrument error or disturbance, as desorption points have shifted right of the adsorption points, and it

cannot be due to the material characteristic. However, the surface area obtained for fTP is $50 \text{ m}^2 \text{ g}^{-1}$, which is twice the surface area obtained for pTP. This change in the surface area of pTP and fTP can be explained by the uniform PANI growth on the carbon fibers on fTP, unlike the agglomerated growth of PANI on pTP, which reduces the available gas adsorption surface, as has been seen in the SEM images. However, after PANI deposition, some porosity is developed, although to a lesser extent. Both fT and fTP show the pore distribution (Figure 13b) predominantly in the range of 3.45 nm, indicating the development of mesoporosity, whereas this is absent in pTP. All these results corroborate well with the SEM images. The half-pore width in fTP (1.58 nm) is higher than that in pTP (1.38 nm). Also, fTP shows pore distribution in the range of 7.76 nm, which is absent in the case of pTP because of clogging of the pores in this range.

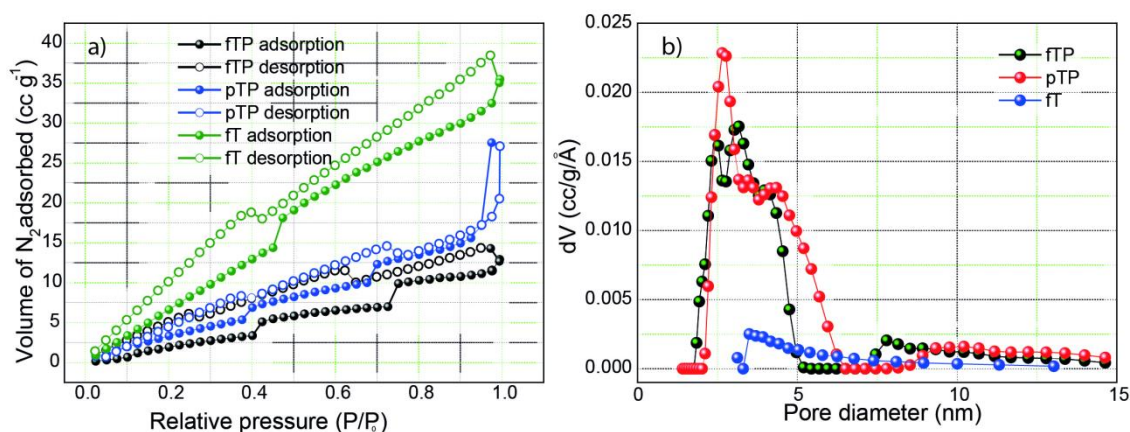


Figure 13. BET analysis: a) adsorption isotherms of fTP, pTP, and fT; b) the pore size distribution of fTP, pTP and fT.

4.3.5 X-ray Photoelectron Spectroscopy

XPS analysis was carried out to get an insight into the electronic properties and the extent of doping in pTP and fTP. The survey spectra of pTP and fTP presented in Figure 14a, b show all characteristic peaks of PANI and carbon. The binding energy of N 1s in fTP is 399.21 eV, whereas that in pTP is 399.01, indicating a shift of 0.20 eV. Similarly, the O 1s binding energy in fTP is 531.81 eV, whereas that in pTP is 532.01 eV, corresponding to a 0.20 eV decrease in the case of the former. The above results infer the transfer of electron density from nitrogen to oxygen in fTP, confirming the interaction between the carbon surface and aniline, which is essential for attaining a uniform coating. The N 1s core level spectra of the two samples are deconvoluted and fitted into the amine ($-\text{NH}-$), protonated amine ($-\text{NH}^{2+}$), imine ($=\text{N}-$), and protonated imine ($=\text{NH}^{+-}$) regions¹³ arising due to different chemical

environments (Figure 14c, d). The oxidation of the polymer chain results in the generation of positive charges, which are balanced by the anion incorporation in the polymer backbone. The extent of oxidation or reduction of the polymer is expressed as doping level and is usually measured by the proportion of the dopant ions or molecules incorporated per monomer unit. Increased doping level creates more mobile charges, hence leading to increased conductivity.¹⁴ The level of doping was determined from the area ratio of the protonated components of the N 1s core level spectra to the total area of the N 1s core level spectra.¹⁵ The maximum doping level achievable in emeraldine form of PANI is 0.5.¹⁶ The doping level determined from the deconvoluted N 1s spectra of fTP is 0.47, whereas that calculated for pTP is 0.41. The higher doping level achieved in the case of fTP can be attributed to the easy diffusion of the electrolyte ions through the PANI thin layers in addition to the higher positive charge density on nitrogen, as discussed above.

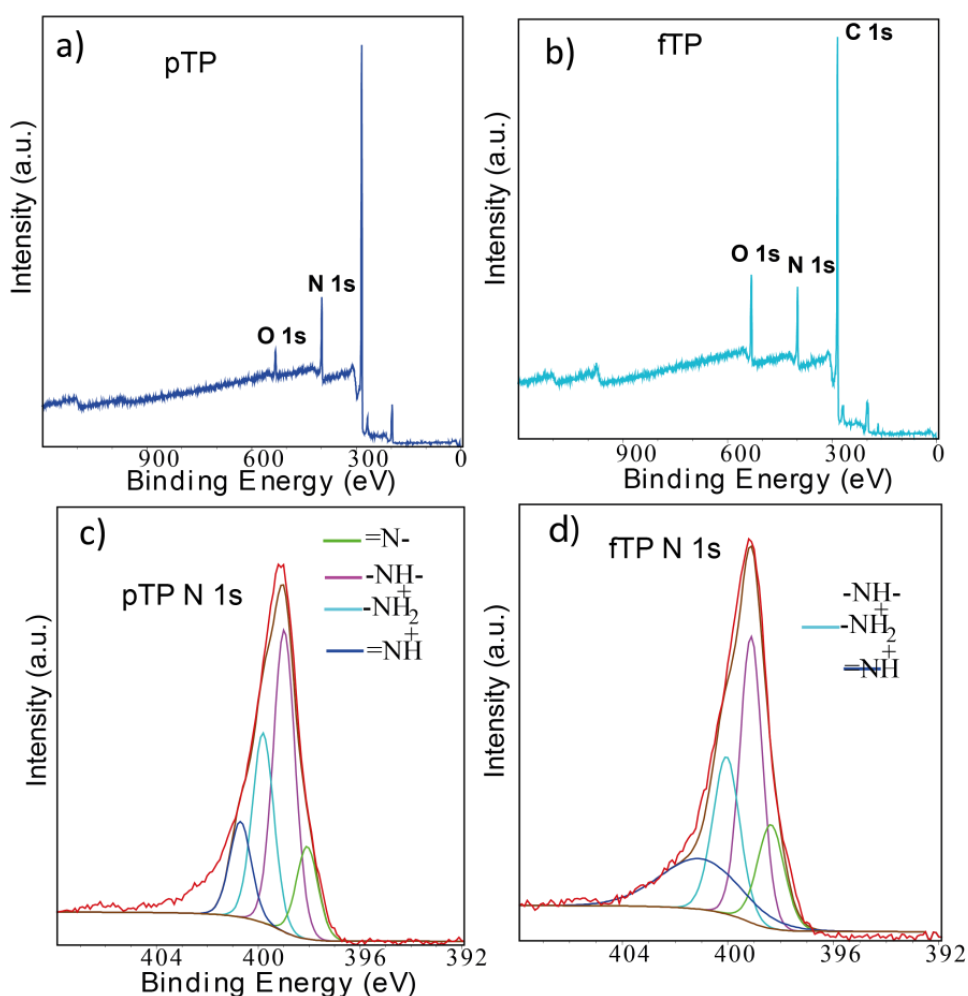


Figure 14. a) X-ray diffraction (XRD) patterns of pT, pTP, and fTP; b) the magnified portion of the XRD profiles presented in a) clearly reveals the changes in the nature of the XRD patterns in each

case; c), d) depict the XPS survey spectra of pTP and fTP, respectively; e), f) represent the deconvoluted N 1s XPS spectra of pTP and fTP, respectively.

4.3.6 Electrochemical Characterization

After a thorough physical characterization of pTP and fTP, electrochemical testing was carried out for correlating the physical properties with electrochemical performance; all liquid state electrochemical measurements were carried out in 0.5 M H₂SO₄ while solid supercapacitor prototype devices were fabricated with PVA-H₂SO₄ gel electrolyte.

4.3.6.1 Electrodeposition of Polyaniline

Although various methods can be employed for electrochemical polymerization, galvanostatic and potentiostatic methods were tested in this study because of their simplicity and better control of deposition parameters. To determine the deposition potential, a CV was recorded at a scan rate of 10 mV s⁻¹ in the polymerization solution; the corresponding plot is given in [Figure 15](#). The onset of electrodeposition determined from [Figure 15a](#) is 0.710 V vs. Ag/AgCl. Taking into account the potential losses due to internal resistance and so forth, a potential greater than 0.710 is required for the electrodeposition.¹⁷ For the above reasons, a potential of 0.80 V was employed for polymerization of PANI through the potentiostatic method. For polymerization at a constant current, a current density of 2 mA cm⁻² was chosen, as lesser current density was not able to generate sufficient deposition potential at the electrode. The corresponding chronopotentiograms are given in [Figure 15b](#).

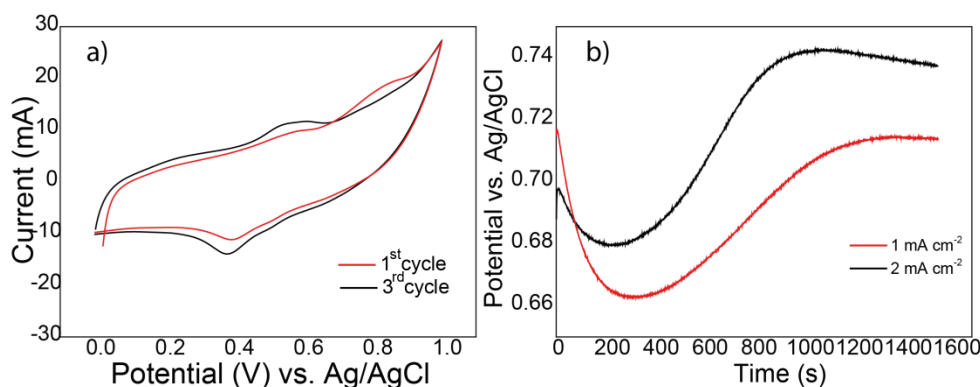


Figure 15. a) Cyclic voltammogram recorded for PANI deposition to determine deposition potential; b) chronopotentiogram measured depicting the variation of potential with time at different deposition currents.

When polymerization was performed at a constant potential of 800 mV, the time taken for the polymerization was 408 s, whereas, when the same amount of charge was passed at a current

density of 2 mA cm^{-2} , the polymerization time was 17 min 24 s. As already discussed in a previous section, a longer polymerization time allows for slow and uniform growth of the polymer, providing sufficient time for the monomer to penetrate inside. CVs recorded for the electrodes prepared by the two methods are shown in Figure 16a. As can be seen from the figure, polymerization at a constant current sweeps an area higher than that attained through the constant potential case, attributable to the increased PANI utilization in the former case. The polymerization was also carried out at the current densities of 2, 5, and 8 mA cm^{-2} in which the amount of charge passed was kept constant in each case to get the same polymer loading. The corresponding CV profiles are presented in Figure 16b. The one corresponding to the PANI deposition at a current density of 2 mA cm^{-2} shows the highest capacitance value, exhibiting broad capacitive peaks responsible for the leucoemeraldine, emeraldine, and pernigraniline transitions. However, the capacitance is found to be reduced when the deposition was carried out at higher current densities. This decrease is attributed to the formation of thicker PANI coatings on the surface of the Toray paper, which limits the active polymer surface.

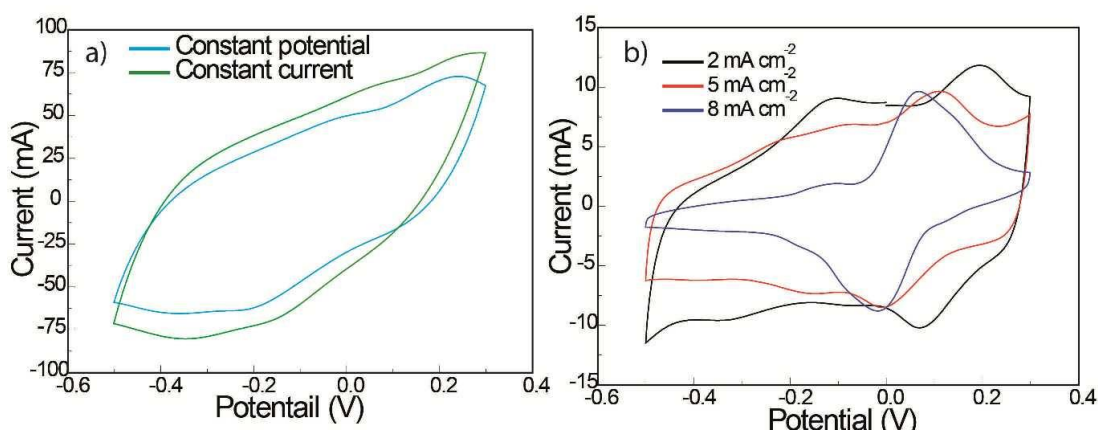


Figure 16. a) Comparative cyclic voltammograms (CVs) recorded at a voltage scan rate of 50 mV s^{-1} for the PANI polymerized on fT by the constant potential and constant current methods; b) the CVs recorded at a scan rate of 5 mV s^{-1} when PANI was polymerized over fT at a constant current with different current densities.

4.3.6.2 Cyclic Voltammetry

Figure 17a shows the CVs of the pTP- and fTP-based solid supercapacitors recorded at 20 mV s^{-1} . The area enclosed by the CV of the fTP device is much larger compared to that enclosed by the pTP device. This observation can be explained by the highly active surface of fTP and efficient infiltration and impregnation by the electrolyte. Moreover, the CVs recorded

at increasing scan rates from 5 to 200 mV s^{-1} (Figure 17b) become progressively more symmetrical and rectangular, which indicates the facile and unrestricted movement of the electrolyte ions and also the high rate capability of the device.

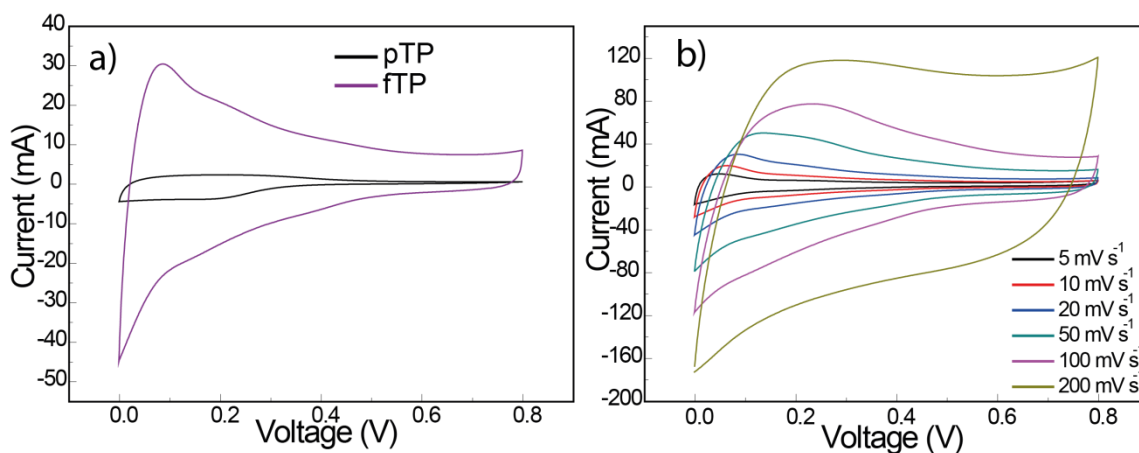


Figure 17. a) CVs recorded for the pTP- and fTP-based solid devices at a scan rate of 20 mV s^{-1} ; b) CVs of the fTP device recorded at increasing scan rates.

4.3.6.3 Electrochemical Impedance Spectroscopy

EIS analysis was also performed to study the ESR, its frequency response, and the movement of electrolyte ions in the polymer network. Figure 18a represents the Nyquist plots acquired on the fTP and pTP devices. The ESR measured for the fTP system is only 0.3Ω , whereas that for the pTP device is 3.3Ω . As has been discussed in the previous section, functionalization decreases the conductivity of the Toray paper. However, after PANI deposition, the sheet resistance of fTP becomes $226 \text{ m}\Omega \square^{-1}$, which is lower than that of pTP ($271 \text{ m}\Omega \square^{-1}$). In fTP, PANI is well-aligned over the carbon fibers, which results in lesser a density of the grain boundaries, unlike pTP where PANI is essentially concentrated on the upper surface of the Toray paper, forming aggregates, which impede its conductivity. Figure 18b gives the variation of the real component (C') of capacitance with the frequency for the fTP device; C' represents the capacitance attained by the supercapacitor. As can be inferred from the curve, the capacitance of fTP is less dependent on the frequency, which is attributed to the high pore accessibility and efficient electrode-electrolyte interface. On the other hand, Figure 18c, which depicts the capacitance variation of pTP, shows the available capacitance to be highly dependent on the frequency. The restricted ion movement and inefficient interface formation lead to such a behaviour.¹⁸ Moreover, the fTP device has a better frequency response, as the maximum capacitance is achieved at a higher frequency (4.8 mHz) compared to the pTP system (2.1 mHz), which attains the maximum capacitance at a very low-

frequency value (measured from Figure 18b, c). Also, the knee-frequency¹⁹ (the frequency at which the behaviour becomes predominantly capacitive, measured from the Nyquist plot) of the fTP system is 3.7 Hz, which is 1.6 times higher compared to the knee-frequency of the device made from pTP (2.4 Hz). Also, the RC time constant of the supercapacitor represents the figure of merit, which gives information about the power capability of the supercapacitor. The time constant of the fTP supercapacitor is measured as 200 ms, whereas that for the pTP device is measured as 300 ms. Hence, an fTP supercapacitor can be charged to 63.2% of its capacitance in just 200 ms giving the device its ultrahigh power capability.²⁰

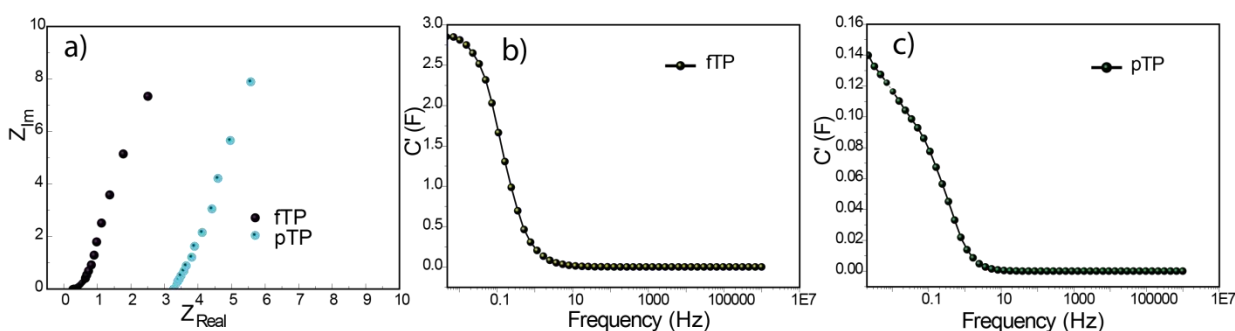


Figure 18. a) Nyquist plots depicting the difference in the ESR of the fTP- and pTP-based devices; b), c) frequency dependence of capacitance for fTP and pTP, respectively.

4.3.6.4 Galvanostatic Charge-Discharge

To assess the practicability of fTP as a high-rate supercapacitor, the charge-discharge experiment of the fTP device was performed in the galvanostatic mode at current densities as high as 10, 20, 30, 40, and 50 A g⁻¹. Figure 19a depicts the charge-discharge curves of the devices fabricated with fT, pTP, and fTP at a current density of 10 A g⁻¹. In the figure, it is evident that the largest area is enclosed by the charge-discharge curve of the fTP device compared to the fT and pTP devices. The capacitance measured at 10 A g⁻¹ for the fTP device is 1335 F g⁻¹, whereas that exhibited by the pTP system at the same current density is only 182 F g⁻¹. Such a large difference between the two can be accounted by the large ESA and porosity available in fTP, which are absent in pTP. The capacitance calculated, taking into account the weight of the current collector, is 84 F g⁻¹. However, the output capacitance of the fTP electrode as high as 1.3 F is exhibited by the 1 cm² electrode surface with just 1 mg of the active material. Areal capacitance based on the geometric area of the electrode is 1.3 F cm⁻²; the areal capacitance measured considering the BET surface area of fTP is also very high at 2.42 mF cm⁻². Furthermore, the volumetric capacitance measured for the device is 9.4 F cm⁻³ at a high current density of 138 mA cm⁻³. At a high current density of 50 A g⁻¹, the

capacitance measured in the fTP device is as high as 1217 F g^{-1} . This means when the current density is increased to 50 A g^{-1} , the device could still deliver 90% of the initial capacitance (Figure 19b). This high rate capability is the result of low mass transfer resistance affected by the adequate porosity that the uniform coating of PANI over the carbon fibers provides in fTP, unlike that in pTP.

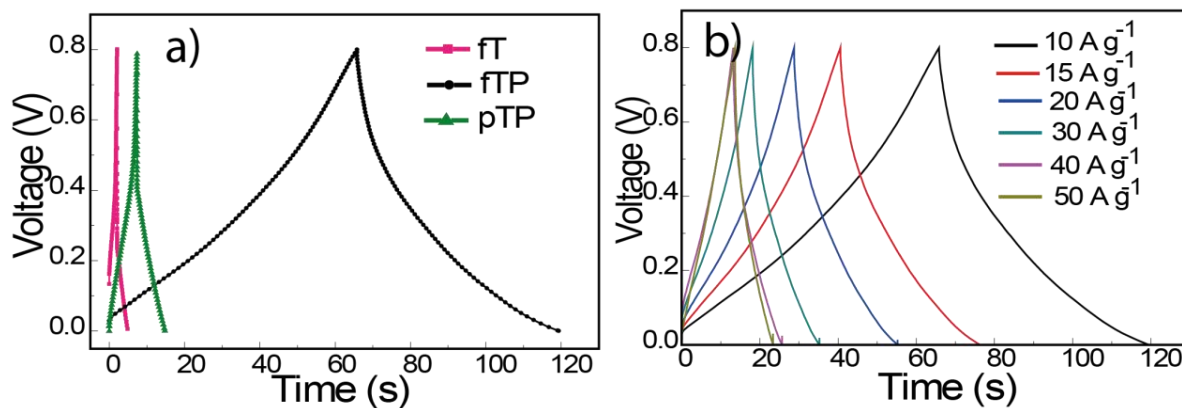


Figure 19. a) Charge–discharge curves for the solid-state devices fabricated from fT, fTP, and pTP at a current density of 10 A g^{-1} ; b) charge–discharge curves for the fTP device recorded at increasing current densities where the curves show a triangular waveform with a negligible potential drop.

4.3.6.5 Rate Capability and Cycling Stability

The high power capability of the device can also be ascertained from Figure 20a, which shows the variation of the discharge current with the scan rate. The current increases linearly with the increase in the scan rate, implying the low resistance and high rate capability of the device. Figure 20b represents the discharge current versus the scan rate plot, and it validates the high rate capability of the solid device. Furthermore, the IR drop of 40 mV is rather low at the current density of 50 A g^{-1} , and the IR drop at 10 A g^{-1} is only 8 mV, as can be observed from Figure 20c. The above results show that along with a high power density, high energy density can also be obtained at a high discharge rate. Stability has always been an issue when PANI is used as a capacitive material because of disintegration and pulverization of the polymer caused by the insertion and expulsion of the ions in the polymer structure.^{21, 22} To prevent the disintegration of PANI, it is necessary to provide ways for the easy movement of ions inside the polymer. The fTP contains adequate porosity and open spaces to not cause stress in the polymer during the insertion-expulsion process. To validate the aforementioned argument, the durability test was performed on the solid-state device for 10,000 cycles at a current density of 50 A g^{-1} , the results of which are shown in Figure 20d. Even at a high

discharge current density of 50 A g^{-1} , 85% of the capacitance could be retained by the device after 10,000 cycles. Moreover, the efficiency of the device is also high, delivering energy with a measured efficiency of 92% after 10,000 cycles. This performance can be credited to the thin uniform coating of PANI achieved in this work and also to the superhydrophilicity of fTP, which helps to form an efficient electrode-electrolyte interface that provides for the facile insertion and expulsion of electrolyte ions, causing less stress on the polymer backbone. This contributes to the high stability. The fTP device could deliver a high energy density of 30 Wh kg^{-1} at a power density of 2 kW kg^{-1} . This energy density is comparable to the energy density of the lead-acid batteries ($30\text{-}60 \text{ Wh kg}^{-1}$ and Panasonic LCR1233P). However, pTP could deliver an energy density of only 4.16 Wh kg^{-1} at a power density of 2 kW kg^{-1} .

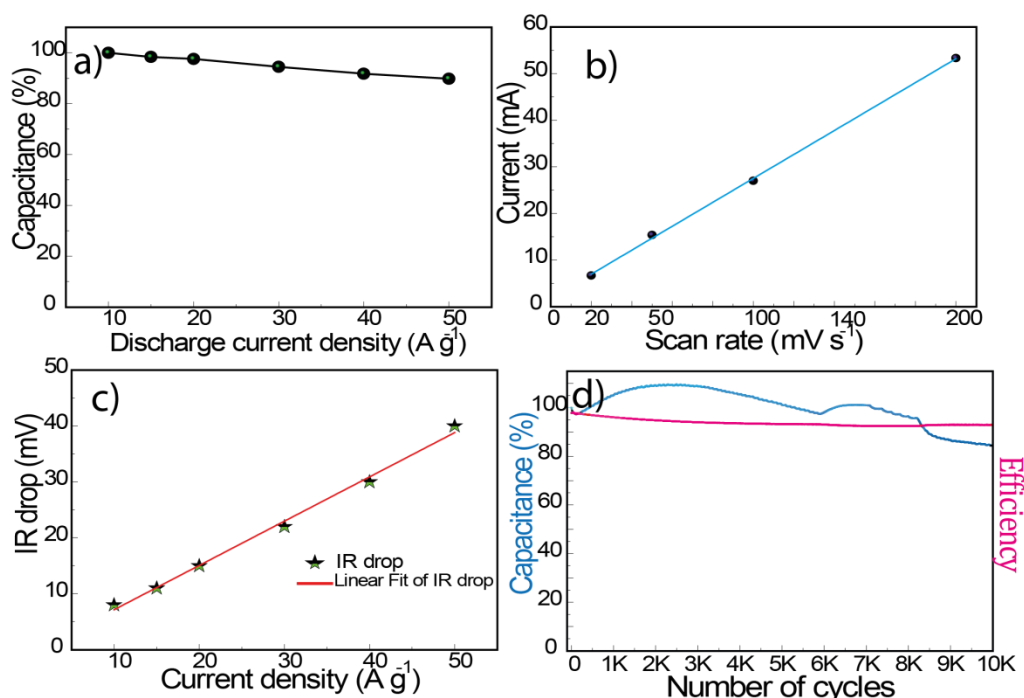


Figure 20. a) the capacitance retention of the fTP-based solid-state device measured at high discharge currents; b) the change in the current with the scan rate for the fTP-based solid-state device; c) potential drop as a function of the increasing current densities for the fTP device; d) durability test carried out for the fTP-based solid device at a current density of 50 A g^{-1} for 10,000 cycles.

4.4 Conclusion

In summary, the current work highlights a novel approach of manipulating the wettability of PANI to make it superhydrophilic toward addressing the low practical capacitance and reduced performance of PANI in a solid supercapacitor. The strategy demonstrated transforms a hydrophobic surface to a superhydrophilic surface, which is used to realize the near

theoretical capacitance and high rate capability in a PANI-based supercapacitor. Here, the electrochemical functionalization has been successfully employed to enhance the ESA of the conducting substrate, which further leads to increased ESA of PANI. All these corroborate to achieve a capacitance of 1700 F g^{-1} in the single cell and a specific capacitance of 1335 F g^{-1} and an areal capacitance of 1.3 F cm^{-2} in the solid-state device at a current density of 10 A g^{-1} . We have achieved an ultralow ESR value of 0.3Ω , which is invoked by the low sheet resistance ($226 \text{ m}\Omega \square^{-1}$) and free electrolyte ion movement. Moreover, the device shows stable performance up to 10,000 cycles with retention of 85 per cent at a current density of 50 A g^{-1} . Moreover, the demonstrated method can be successfully applied to other systems, such as PEDOT, polypyrrole, and metal oxides such as MnO_2 and so forth, to enhance the electrochemically active surface area and performance.

4.5 References

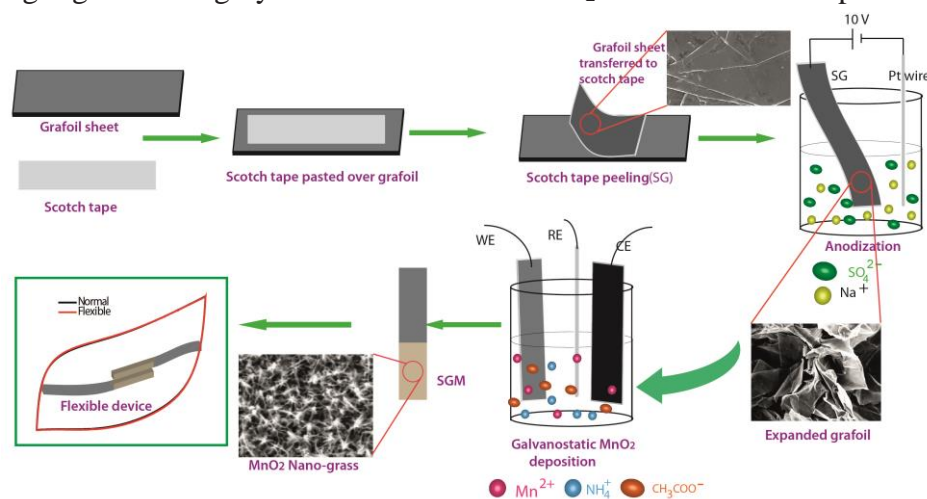
1. H. Li, J. Wang, Q. Chu, Z. Wang, F. Zhang and S. Wang, *Journal of Power Sources*, 2009, **190**, 578-586.
2. I. Y. Choi, J. Lee, H. Ahn, J. Lee, H. C. Choi and M. J. Park, *Angewandte Chemie International Edition*, 2015, **54**, 10497-10501.
3. L. Pan, G. Yu, D. Zhai, H. R. Lee, W. Zhao, N. Liu, H. Wang, B. C.-K. Tee, Y. Shi, Y. Cui and Z. Bao, *Proceedings of the National Academy of Sciences*, 2012, **109**, 9287-9292.
4. G. Yu, L. Hu, N. Liu, H. Wang, M. Vosgueritchian, Y. Yang, Y. Cui and Z. Bao, *Nano Letters*, 2011, **11**, 4438-4442.
5. T. Liu, L. Finn, M. Yu, H. Wang, T. Zhai, X. Lu, Y. Tong and Y. Li, *Nano Letters*, 2014, **14**, 2522-2527.
6. Y. Zhu, S. Murali, M. D. Stoller, K. J. Ganesh, W. Cai, P. J. Ferreira, A. Pirkle, R. M. Wallace, K. A. Cychoz, M. Thommes, D. Su, E. A. Stach and R. S. Ruoff, *Science*, 2011, **332**, 1537-1541.
7. W. Gu, N. Peters and G. Yushin, *Carbon*, 2013, **53**, 292-301.
8. Q. Dong, Y. Zhou, J. Pei, Z. Liu, Y. Li, S. Yao, J. Zhang and W. Tian, *Organic Electronics*, 2010, **11**, 1327-1331.
9. X. C. Chen, G.; Ma, Y.; Li, X.; Jiang, L.; Wang, F., *J. Nanosci. Nanotechnol.*, 2006, **6**, 783-786.
10. M. Döbbelin, R. Tena-Zaera, R. Marcilla, J. Iturri, S. Moya, J. A. Pomposo and D. Mecerreyes, *Advanced Functional Materials*, 2009, **19**, 3326-3333.
11. M. Jahan, Q. Bao and K. P. Loh, *Journal of the American Chemical Society*, 2012, **134**, 6707-6713.
12. J. A. Rouquerol, D.; Fairbridge, C. W.; Everett, D. M.; J. H. P. Haynes, N.; Ramsay, J. D. F.; Sing, K. S. W.; Unger, and K. K., *Pure Appl. Chem.*, 1994, **66**, 1739-1758.
13. S. Mondal, U. Rana and S. Malik, *Chemical Communications*, 2015, 51, 12365-12368.
14. A. G. MacDiarmid, R. J. Mammone, R. B. Kaner, S. J. Porter, R. Pethig, A. J. Heeger and D. R. Rosseinsky, *Philosophical Transactions of the Royal Society A: Mathematical, Physical and Engineering Sciences*, 1985, **314**, 3-15.
15. M. M. Mahat, D. Mawad, G. W. Nelson, S. Fearn, R. G. Palgrave, D. J. Payne and M. M. Stevens, *Journal of Materials Chemistry C*, 2015, **3**, 7180-7186.
16. S. Quillard, G. Louarn, S. Lefrant and A. G. Macdiarmid, *Physical Review B*, 1994, **50**, 12496-12508.
17. Y. Mohd, R. Ibrahim and M. F. Zainal, 2012 IEEE Symposium on Humanities, Science and Engineering Research, 2012.

18. P. L. Taberna, P. Simon and J. F. Fauvarque, *Journal of The Electrochemical Society*, 2003, **150**, A292.
19. R. Soni, B. Anothumakkool and S. Kurungot, *ChemElectroChem*, 2016, **3**, 1329-1336.
20. A. C. Yu, V.; Zhang, J., *Electrochemical Supercapacitors for Energy Storage and Delivery*, 2013, CRC Press, 2013; **Vol. 1**, p 18.
21. Y.-Y. Horng, Y.-C. Lu, Y.-K. Hsu, C.-C. Chen, L.-C. Chen and K.-H. Chen, *Journal of Power Sources*, 2010, **195**, 4418-4422.
22. C. Meng, C. Liu, L. Chen, C. Hu and S. Fan, *Nano Letters*, 2010, **10**, 4025-4031.

Chapter-5

Organization of MnO₂ into Grass-like Nanofibril Structure on Electrochemically Modified Carbon Sheets for Flexible Supercapacitor

Manganese oxide (MnO₂) has been intensively studied for its charge storage properties. It is well established that thin films of MnO₂ are electrochemically more active than the thicker MnO₂ films due to the low conductivity of the thick films and high diffusion coefficient of the cations. Also, development of flexible supercapacitors is limited by the availability of flexible and durable conducting substrates; a conducting and cheap substrate for the active material deposition is essential for achieving breakthrough progress in this direction. This chapter highlights how highly thin nanofibers of MnO₂ could be electrodeposited on electrochemically



modified carbon sheets. Also, a highly flexible, conducting, and cheap substrate is prepared by simple stick and peel-off method involving Scotch

tape and Grafoil. The Grafoil–Scotch tape derived flexible substrate exhibits a sheet resistance of $7 \Omega \square^{-1}$ along with a high degree of flexibility and durability. Moreover, its properties are further enhanced by the anodization in order to increase the hydrophilicity and surface area. The substrate is highly thin with a thickness of just $74 \mu\text{m}$. The nanofibrous MnO₂ assembly possesses ample porosity allowing for the deeper penetration and facile movement of electrolyte ions. The fibrous nature of MnO₂ results in high electrochemically active surface area, which eventually leads to high specific capacitance. The fabricated device exhibits high capacitance retention under bent (99%) and twisted (98%) conditions along with a low ESR of 7Ω .

Content of this chapter is published in the following article:

Nanoscale, 2017, **9**, 3593-3600.

(<http://pubs.rsc.org/en/content/articlelanding/2017/nr/c7nr00281e#!divAbstract>)

Reproduced by permission of Royal Society of Chemistry

5.1 Introduction

Among the capacitive materials, metal oxides are highly promising owing to their very high theoretical capacitance, unlike the electrochemical double layer capacitors (EDLCs). Among them, MnO_2 (manganese dioxide) as a pseudocapacitive material is very promising due to its high theoretical capacitance (1232 F g^{-1}),¹ environmental benignity, high abundance and low cost. However, low conductivity¹ (10^{-5} – $10^{-6} \text{ S cm}^{-1}$) and less material utilization in thick films are the major challenges here, whereas thin films of MnO_2 , even though they show high specific capacitance,² are prone to stability issues. Moreover, to use MnO_2 in the flexible devices, the interaction between the substrate should be highly intimate to establish easy charge transfer between MnO_2 and the substrate, thereby enabling efficient current collection. Low conductivity along with poor interaction with the solid substrate and less electrolyte penetration lead to high equivalent series resistance (ESR) in the solid-state devices. This adversely affects the rate capability of the devices.

Flexible electronics is the next revolution in the realm of consumer electronics; flexibility makes the electronic gadgets more attractive in terms of design, durability and space occupancy, along with cost benefits at a commercial scale production rate. Considering these huge future prospects of flexible electronics, there has been a growing thrust towards developing flexible energy storage systems, which are an integral part of the future power electronics. Supercapacitors³ are highly beguiling energy storage devices owing to attributes like high power density, fast charge-discharge characteristics, durability, and long cycle life. To be used as a power source in flexible electronics, a supercapacitor has to be solid and flexible.⁴ The general approach used towards the fabrication of a flexible supercapacitor is to deposit the active materials, like various carbon morphologies, on a flexible substrate, like polyethylene terephthalate⁵ (PET), or polydimethylsulphoxide⁶ (PDMS). Although highly durable, they suffer from limited flexibility and non-conductive nature, which enforce metal coating like gold for current collection with a further increment in cost and complexities in the manufacturing.⁷ In addition, papers made from graphene, CNTs etc. have been used as conducting flexible substrates.⁸ However, conducting papers made out of carbon materials have constrained flexibility.

In this context, we have come up with a practical solution to overcome the above discussed issues by developing a highly flexible, conducting and cheap Grafoil-based substrate by a Scotch tape peel-off method. The prepared substrate is then taken for electrodeposition of thin films of MnO_2 by the galvanostatic method. The novel and unique grass-like morphology of the electrodeposited MnO_2 with porous structure assists in easy electrolyte penetration and

low ESR. The flexible solid supercapacitor fabricated by the above strategy shows high capacitance and durability along with excellent resilience to various stress-strain conditions.

5.2 Experimental Section

5.2.1 Material

Grafoil was purchased from Global Nanotech; manganese acetate ($\text{Mn}(\text{CH}_3\text{COO})_2$), ammonium acetate ($\text{CH}_3\text{COONH}_4$) and polyvinyl alcohol (PVA) were supplied by Sigma-Aldrich; lithium chloride (LiCl) was provided by Rankem Chemicals.

5.2.2 Preparation of SG (Grafoil-scotch Tape Flexible Substrate)

For preparing the flexible substrate, a piece of Scotch tape was placed on the Grafoil sheet and was then pressed to make uniform adhesion. Subsequently, the Scotch tape was peeled off from Grafoil; during this process, a thin layer of Grafoil gets transferred onto the Scotch tape. The obtained Grafoil-Scotch tape substrate is termed as SG.

5.2.3 Electrochemical Anodization.

For anodizing SG, a 10 V potential was applied to the SG in 0.1 M sodium sulphate (Na_2SO_4) solution for 10 sec with a platinum (Pt) wire as an auxiliary electrode. At the applied potential, the edges of the Grafoil are oxidized, thereby resulting in the expansion. Sulphate ions then penetrate into the inner layers of Grafoil; movement of the ions (SO_4^{2-}) inside the graphite layers is facilitated by the expansion caused by the oxidation of the edges. Reduction of the intercalated sulphate ions produces SO_2 gas, which escapes violently from the inner sheets leading to the exfoliation and layer expansion, creating defects and roughness over the surface.

5.2.4 Electrodeposition of MnO_2 Nano-grass

A conventional three-electrode cell was used for the synthesis of MnO_2 nano-grass in which the exfoliated Grafoil was employed as the working electrode whereas Pt wire and carbon paper were used as the quasi-reference and the auxiliary electrodes, respectively. The deposition solution was made up of a mixture of 0.1 M manganese acetate ($\text{Mn}(\text{CH}_3\text{COO})_2$) and 0.1 M ammonium acetate ($\text{CH}_3\text{COONH}_4$), where the later was serving as the supporting electrolyte. A constant current (anodic deposition) of 4 mA cm^{-2} was applied to the working electrode for the time periods of 28, 56, 111, and 166 s; the corresponding electrodes are termed as SGM-28, SGM-56, SGM-111, and SGM-166, respectively. During

electrodeposition, Mn^{2+} ions are oxidized to the Mn^{4+} oxidation state at the working electrode (anode), which is subsequently deposited as MnO_2 over the working electrode surface.

5.2.4 Solid-State Flexible Device Fabrication

Solid-state devices were fabricated by applying a thin layer of 20 wt. % PVA–LiCl gel electrolyte on the active area of 1 cm^2 . The electrodes were then kept under ambient conditions for 12 h at room temperature to allow for the impregnation of the electrolyte and evaporation of excess water. A polycarbonate film (Celgard) was used as a separator. After applying the electrolyte to the separator, it was placed between two SGM electrodes and pressed together to obtain the solid supercapacitor device.

5.2.5 Characterization

A Zeiss Ultra Plus scanning electron microscope was used to analyze the morphology of the electrodeposited MnO_2 . TEM analysis was carried out with a Tecnai-T20 at an accelerating voltage of 200 kV. Thickness measurements were performed on a Mitutoyo micrometer. XRD spectra were recorded with a Rigaku SmartLab diffractometer with $\text{Cu K}\alpha$ radiation ($\lambda = 1.5406 \text{ \AA}$) at a scan rate of 2° min^{-1} . For Raman analysis, a LabRAM spectrometer (HJY, France) was used. XPS spectra were recorded on a VGMicrotechmultilab ESCA 3000 spectrometer. BET surface area and the pore size distribution were measured using ultra-pure N_2 on a Quantachrome Quadrasorbe automatic volumetric instrument. A Bio-Logic SP-300 PG Stat was employed for carrying out the electrochemical analyses, including cyclic voltammetry, impedance measurements, and galvanostatic charge/discharge measurements. Electrochemical data were analyzed using EC-Lab software V10.19. Sheet resistance was calculated with a four-probe conductivity meter with probe spacing of 0.2 mm, and the conductivity changes under flexible conditions were measured by I–V polarization through linear sweep voltammetry.

5.3 Result and Discussion

5.3.1 Properties of SG

5.3.1.1 Thickness Measurement

The conducting substrate is derived by sticking the Scotch tape onto the Grafoil surface and then peeling it off. A thin film of the Grafoil is transferred to the tape owing to strong adhesion between the Grafoil and the Scotch tape. The obtained substrate has a thickness of $74 \mu\text{m}$, as measured through a micrometer, with a $60 \mu\text{m}$ contribution from the Scotch tape and merely $14 \mu\text{m}$ from the transferred Grafoil. The overall thickness of this unit is relatively

thin compared to the other flexible substrates like PET⁹ and polyimide,¹⁰ reported in the literature.

5.3.1.2 Electron Microscopy Analysis

Image ‘a’ in Figure 1 shows the changes in the surface accrued after the anodization; the anodized surface becomes darker compared to the non-anodized one. The FESEM images presented in Figure 1b and c show a highly smooth and flat surface obtained for the Grafoil–Scotch tape substrate (SG). Furthermore, the images at the bottom demonstrate the highly thin and flexible nature of the substrate. Moreover, the flat nature of SG can also be ascertained from the cross-section SEM image provided in Figure 1d. However, for the supercapacitor applications, porous and rough surfaces with high hydrophilicity are ideal. Hence, for creating porosity and enhancing the hydrophilicity, electrochemical anodization was adopted by keeping SG as the anode in the process. A high potential of 10 V¹¹ was applied over the surface area of 1 cm² of SG in 0.1 M sodium sulphate solution. Application of the potential results in the reduction of water, producing OH[−] ion, which is a strong nucleophile. It attacks the edge sites and grain boundaries of the Grafoil; the subsequent oxidation of the Grafoil results in depolarization and expansion of the graphite layers, which facilitates the intercalation of the sulphate ions (SO₄^{2−}) into the expanded sheets. Owing to the low reduction potential of the SO₄^{2−} ions (+0.20 V),¹¹ they get easily reduced to SO₂ gas and violently escape the sheets. This result in expansion of the graphite layers, leading to the separation of the individual sheets with the creation of porosity and roughness, as shown in the FESEM images presented in Figure 1e and f. In addition, the cross-section SEM image given in Figure 1g corroborates with the images presented in Figure 1e and f. The TEM image (Figure 2) of the anodized SG displays a thin graphene sheet-like structure.

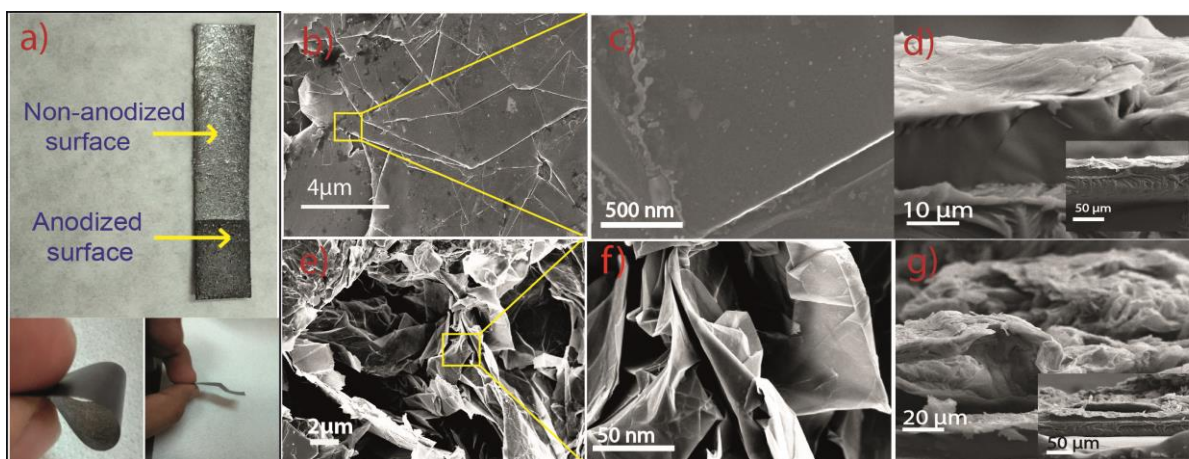


Figure 1. a) Image of the substrate obtained by the Grafoil-Scotch tape peel off method and its subsequent anodization; b) FESEM image of SG before exfoliation, where the surface appeared to be relatively smooth and flat with no apparent porosity; c) high magnification image of the SG before exfoliation; d) cross-section SEM image of the SG prior to the anodization process; e) FESEM image of SG after the electrochemical anodization, where the graphite sheets are appearing well-separated with adequate porosity; f) high magnification FESEM image of the image e); g) cross-section image of the exfoliated SG.

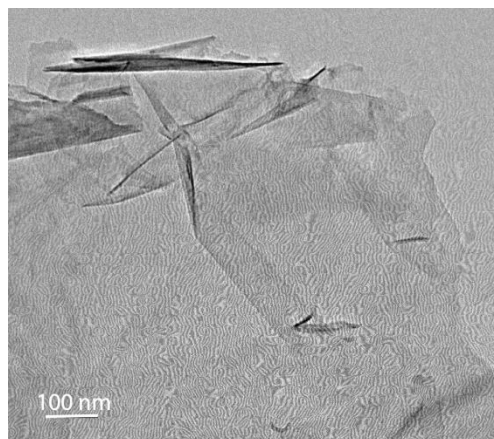


Figure 2. TEM image of the exfoliated SG showing the features very similar to the few layered graphene sheets

5.3.1.3 Raman Analysis

Creation of the defects is also confirmed by the Raman analysis, which is shown in [Figure 3a](#) and [b](#). The ratio of the d-band (the defective carbon) to the g-band (the graphitic carbon) (*i.e.* the I_d/I_g ratio) after the anodization is found to be increased from 0.1 to 0.85 owing to the combined effects of the layer separation, defects, and functionalities.

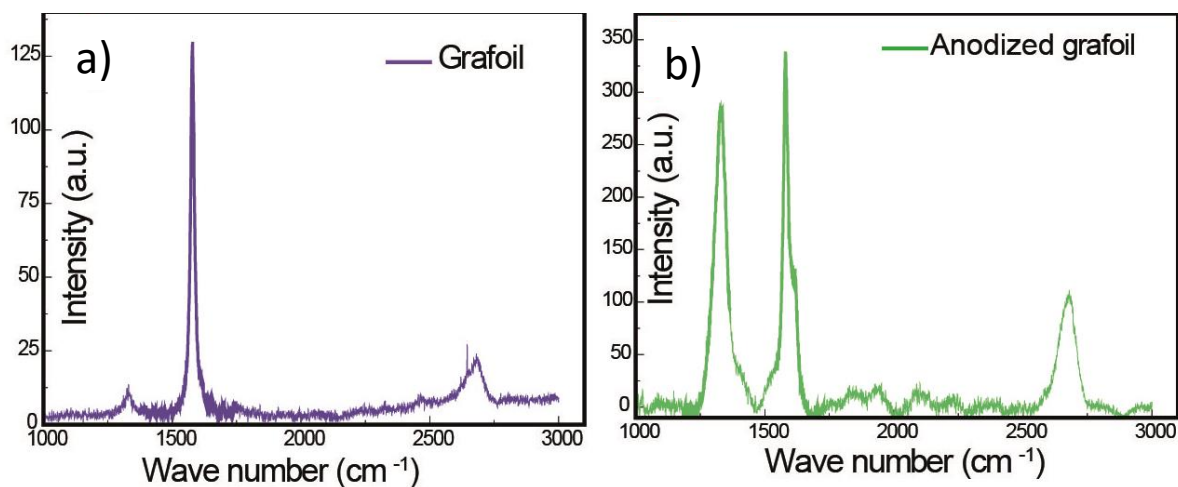


Figure 3. Raman spectra of the Grafoil recorded before and after the anodization process.

5.3.1.4 X-ray Diffraction

In the XRD pattern presented in Figure 4 of the anodized Grafoil, the peak at the 2θ of 26° has split into two peaks, which is attributed to the Na^+ intercalation.¹²

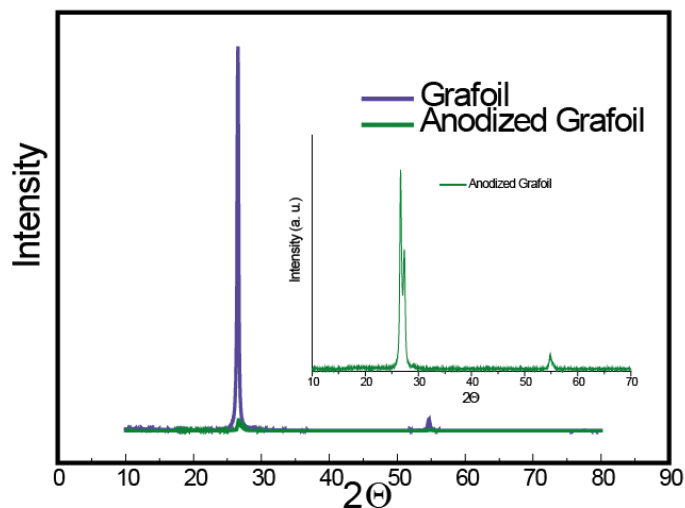


Figure 4. Comparative XRD spectra of the Grafoil and the anodized Grafoil.

5.3.1.5 Conductivity Measurement

After the anodization, the electrical conductivity was found to be decreased from 100 S cm^{-1} to 20 S cm^{-1} owing to the presence of defects, separation of the carbon sheets and enhancement in the porosity.

5.3.1.6 Cyclic Voltammetry Study of Anodized SG

Surface area enhancement upon anodization can also be ascertained from the cyclic voltammograms (CVs) given in Figure 5, which show an increase in the area under the curve with the increase in the anodization time.

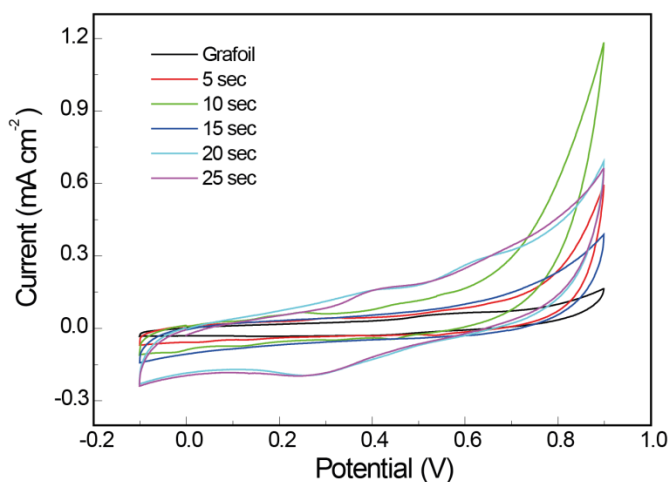


Figure 5. Cyclic voltammograms recorded at a scan rate of 5 mV s^{-1} depicting the changes in the Grafoil double-layer structure with the anodization time.

5.3.1.7 Flexibility Test

The effect of mechanical stress on the conductivity of SG was further analyzed by performing linear sweep voltammetry in the potential range of -1.0 to 1.0 V , as shown in the linear sweep voltammograms (LSVs) presented in [Figure 6a](#) and [b](#). SG is highly durable and resilient to the stress, as indicated by the completely superimposable LSV curves under the bending and twisting conditions.

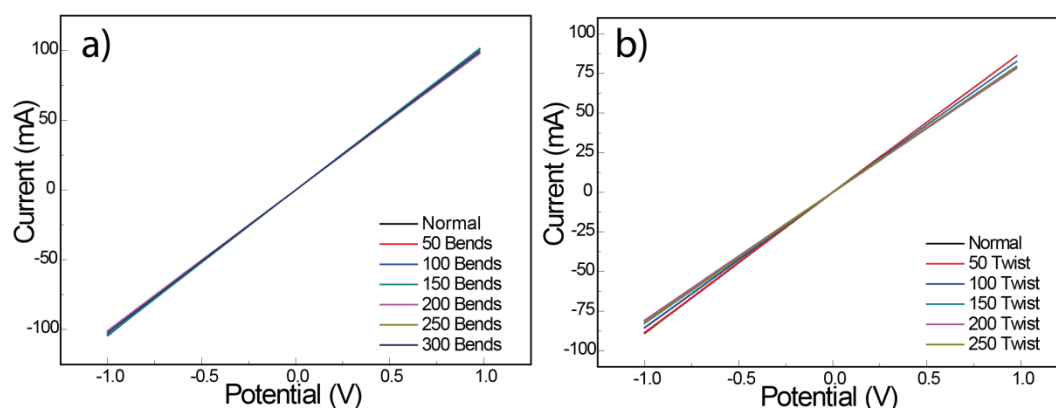


Figure 6. a) the LSV profiles of SG under the bending stress, which do not show any appreciable change in the I-V profile even after the 300 bending cycles; b) the twisting ability of SG, which shows good resilience to the twisting strain as revealed from the well-nigh overlapped I-V curves.

5.3.2 Physical Characterization of MnO_2

5.3.2.1 Electronic Microscopy Analysis

The effect of the current density on the morphology of MnO_2 was also examined through SEM images to analyze the CV behaviour; the corresponding SEM images are shown in [Figure 7](#). It can be seen that the deposition of MnO_2 at a current density of 2 mA cm^{-2} results in highly porous thin-walled partly interconnected fibrous MnO_2 within a porous thin vertical wall-type structure ([Figure 7a](#)) whereas deposition at 4 mA cm^{-2} ([Figure 7b](#)) leads to the formation of a highly inter-connected, porous, and fibrous grass-like morphology and the profusely inter-connected fibers along with porosity can help in achieving high capacitance.

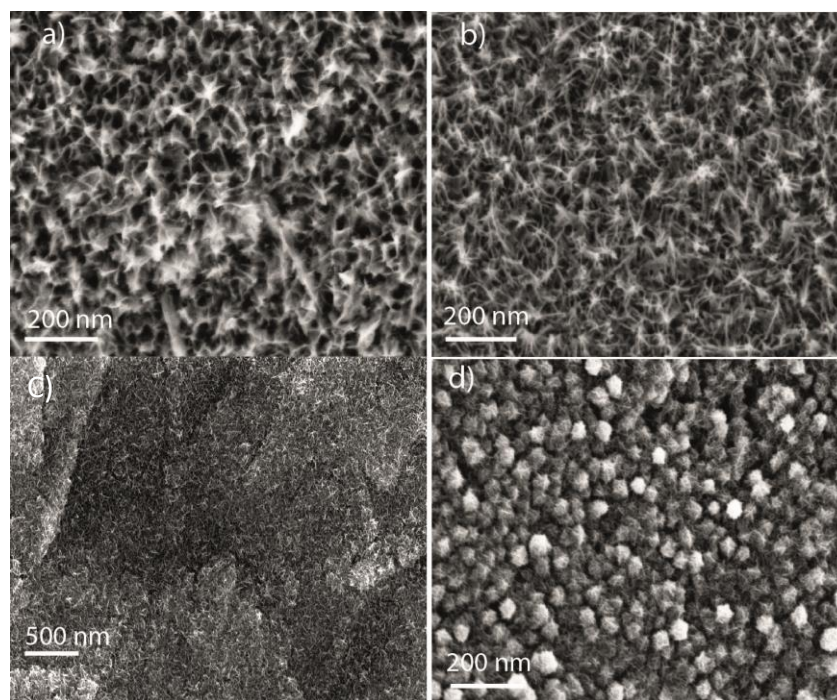


Figure 7. The effect of current density on the capacitance was studied by analyzing the changes in morphology occurring on applying different deposition current densities. a) FESEM image of SGM where the deposition current density was 2 mA cm^{-2} ; b) FESEM image of SGM with a deposition current density of 4 mA cm^{-2} ; c) FESEM image of the MnO_2 deposited at a current density of 6 mA cm^{-2} ; d) FESEM image of SGM at a high current density of 8 mA cm^{-2} .

With further increase in the current density to 6 mA cm^{-2} , MnO_2 is deposited as a thick sheet-like structure and the open spaces can be seen disappearing compared to the deposition carried out at low current densities (Figure 7c). At a current density as high as 8 mA cm^{-2} , the MnO_2 fibrous structure coalesces into a spherical structure, exhibiting reduced porosity and densely packed spheres, as shown in Figure 7d. Thus, morphology-wise, the fibrous grass-like porous growth pattern of MnO_2 deposited at 4 mA cm^{-2} appears to be the right candidate that can exhibit high capacitance compared to the rest of the samples.

Electrodeposition was carried out through anodic method at different time scales of 28, 56, 111 and 166 s at a current density of 4 mA cm^{-2} to an active area of 1 cm^2 , which resulted in the loading of MnO_2 in each case as 0.05, 0.10, 0.20 and 0.30 mg, respectively. The corresponding samples are designated as SGM-28, SGM-56, SGM-111 and SGM-166, respectively, where the number represents the time for which the current is passed. The SEM images presented in Figure 8a and b depict the morphology of the surface before and after the MnO_2 deposition, which reveal that the exfoliated nature of the graphite sheets remains intact even after the MnO_2 deposition. With the increase in the deposition time, although the grass-

like morphology can be seen, the MnO₂ film becomes denser and more compact with less porosity compared to SGM-28. The changes occurring in the MnO₂ thickness and its morphology with respect to the deposition time are shown in Figure 8c-f. The FESEM images shown in Figure 9a and b for SGM-28 reveal a grass-like morphology with interconnected fibrous MnO₂ structures. Pores can be clearly seen in these FESEM images.

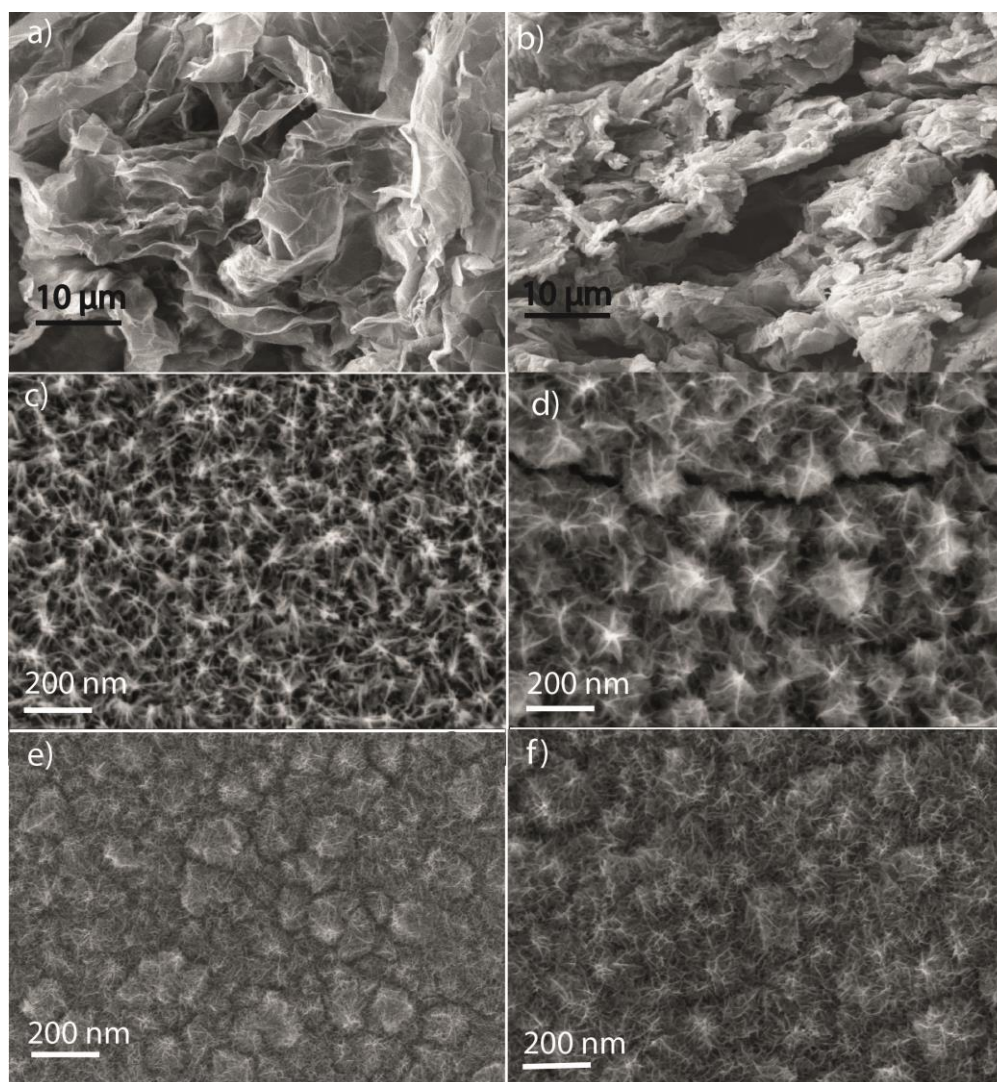


Figure 8. SEM images of: a) the anodized SG; b) low magnification image of SGM-28. FESEM images of MnO₂ deposited at different time intervals at a current density of 4 mA cm⁻²: c) SGM-28; d) SGM-56; e) SGM-111; f) SGM-166.

The TEM image of SGM-28 presented in Figure 9c shows the similar grass-like morphology of MnO₂ with the interconnected fibrous structure and pores covering the entire surface of the substrate. The SEM and TEM images are taken for the same sample and, therefore, they are expected to represent the same structural features of the deposited MnO₂. However, subtle

changes observed in the nature of the morphologies in both the images are owing to the difference in the level of magnifications and also to the fundamental difference in the working of SEM (where the secondary electrons are used for imaging) and TEM (where the transmitted electrons are employed for the image formation). In addition, the expanded graphite sheet as a substrate is playing a crucial role in nucleating this growth pattern of MnO_2 , implying strong adherence of MnO_2 with the underlying graphite sheet. This can be clearly evident from the SEM image in Figure 9d of the MnO_2 deposited over the non-anodized SG. The image shows thick sheets with abundant cracks and coarser particles compared to SGM-28, which shows very distinct grass-like morphology.

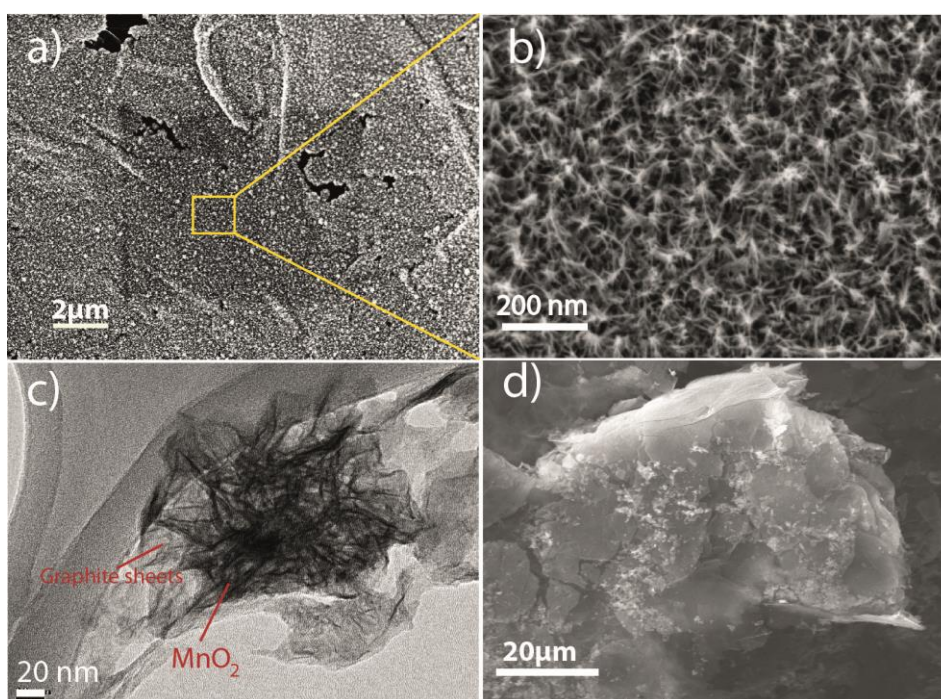


Figure 9. a) FESEM image of SGM-28 where the SG surface is uniformly covered by a thin film of MnO_2 ; b) magnified view of the part of SGM-28 encircled in a), which shows a highly interconnected fibrous grass-like morphology of MnO_2 with well dispersed pores; c) representative TEM image of SGM-28, authenticating the interconnected fibrous nature of the grass-like growth pattern of MnO_2 , where the graphite and MnO_2 layers are marked for clarity; d) SEM image of the MnO_2 layer electrodeposited on the pristine non-anodized Grafoil.

5.3.2.2 BET Analysis

To analyze the change in the pore size and surface area with respect to the electrodeposition conditions, BET analysis (Figure 10) was carried out on all the SGM samples without scratching out the MnO_2 -Grafoil layer from the Scotch tape. Scratching out of the MnO_2 -

Grafoil is avoided in order to prevent any mechanical alteration of the active layer, which might result in some possible changes in the surface area and pore size values. It is observed that with an increase in the deposition time, the surface area of the samples decreases in the order of 114, 105, 100 and 60 $\text{m}^2 \text{g}^{-1}$ for SGM-28, SGM-56, SGM-111, and SGM-166, respectively. A similar trend is observed for the pore size distribution, where the prominent region of the pore size is found to be reduced to 1.30 nm for SGM-166 compared to 1.58 nm for SGM-28. Corresponding to this, the average pore volume is also found to be shifted from 0.111 cc g^{-1} for SGM-28 to 0.053 cc g^{-1} for SGM-166, indicating progressive blocking of the pores when more MnO_2 gets deposited at longer depositing times.

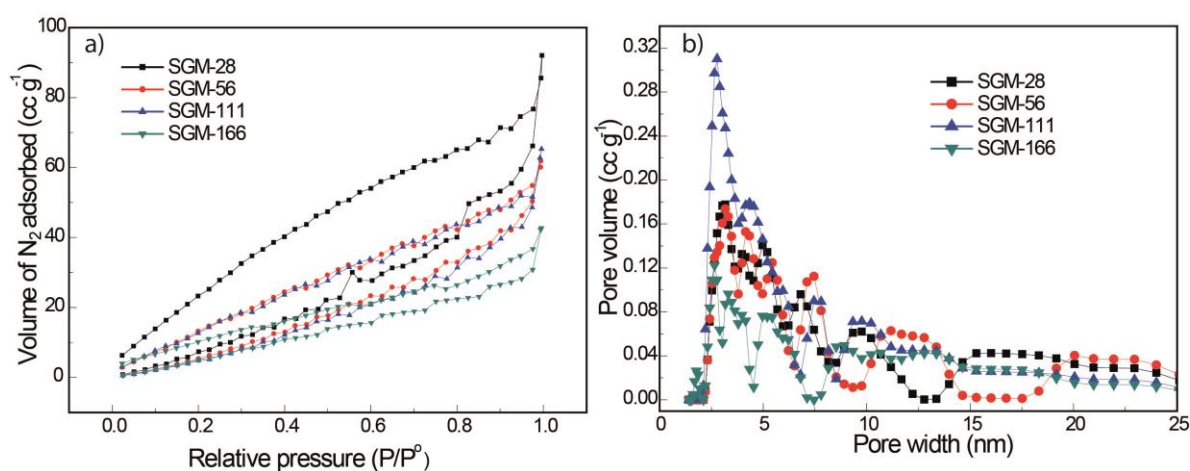


Figure 10. a) N_2 adsorption isotherms of the SGM samples corresponding to the various electrodeposition periods; b) the pore size distribution profiles of the SGM samples prepared at various electrodeposition periods.

5.3.2.3 X-ray Diffraction

The amorphous nature of MnO_2 is further confirmed by the XRD of SGM-28 (Figure 11), which does not show any characteristic peaks of the MnO_2 phase.

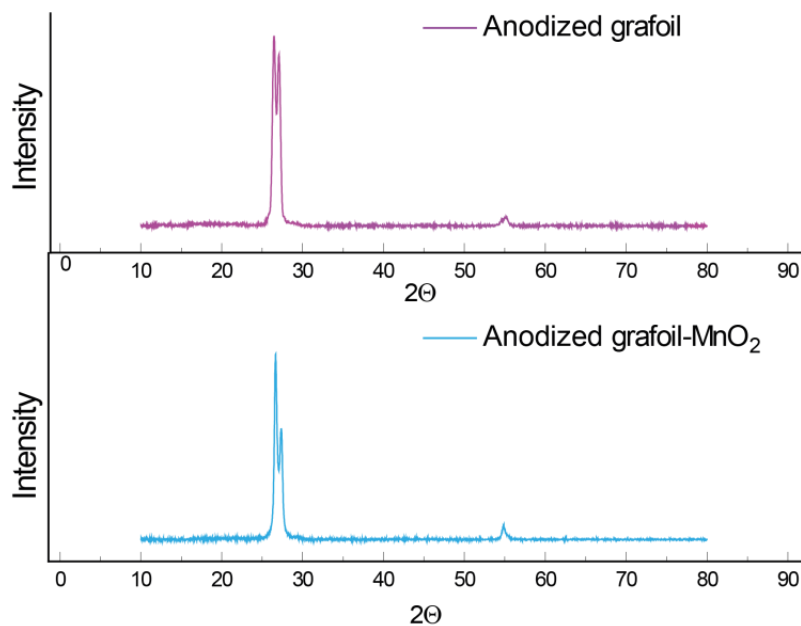


Figure 11. The XRD patterns of the anodized Grafoil and SGM-28.

5.3.2.4 X-ray Photoelectron Spectroscopy

XPS analysis of SGM-28 was also carried out to confirm the deposition and oxidation state of MnO_2 . The XPS survey spectrum is shown in Figure 12a. The carbon peaks appear at a binding energy of 286.4 eV, whereas, the characteristic Mn peaks can be seen at 642.0 (Mn 2P) and 654.5 eV (Mn $2P_{1/2}$), which are similar to the values reported in the literature for the corresponding states. Moreover, the binding energies of Mn $2P_{1/2}$ and Mn $2P_{3/2}$ confirm the +4 oxidation state of Mn.¹³

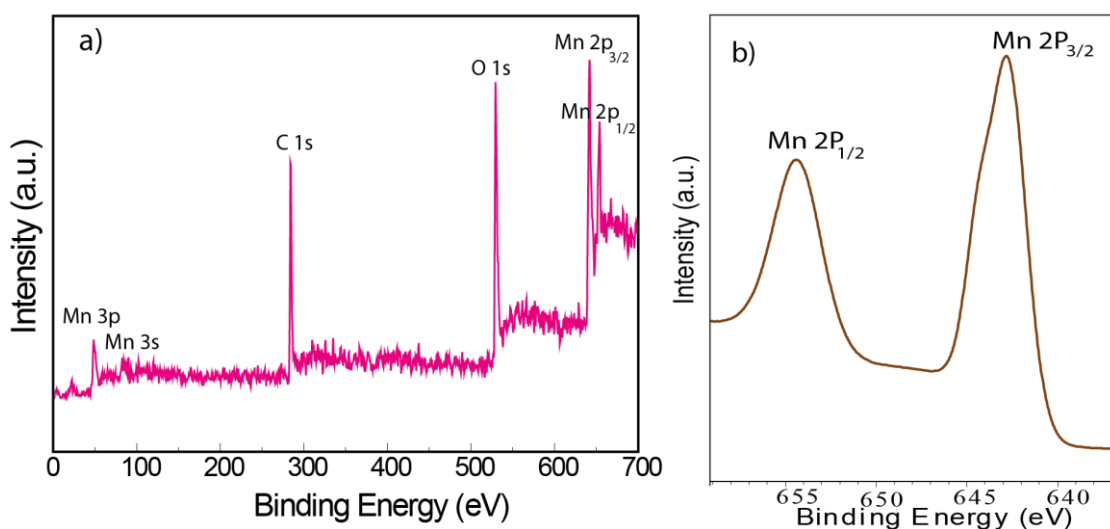


Figure 12. XPS analysis of the samples: a) survey XPS of SGM-28 showing the characteristic peaks of the MnO_2 along with the peak for the carbon originating from the Grafoil; b) Mn 2p XPS, where the binding energy of the peaks corresponding to Mn 2p_{3/2} and Mn 2p_{1/2} appear at 642.0 and 654.5 eV, respectively.

5.3.3 Electrochemical Characterization

Electrochemical characterization was carried out on a solid-state device fabricated using PVA-LiCl gel electrolyte,¹⁴ by scanning at a potential window of 0.80 V.

5.3.3.1 Cyclic Voltammetry

Cyclic voltammograms of the devices fabricated using SGM-28, SGM-56, SGM-111 and SGM-166 as the electrodes are shown in Figure 13a. The area under the SGM-28 based device is far greater than that of the other devices. The decrease in specific capacitance with the increase in the deposition time, or in other words, with the thickness of the active layer, is similar to the previously reported MnO_2 based devices,¹⁵ It is well established that only a fraction of a thick film² of the MnO_2 is involved in the redox reaction, leaving the bulk of the material un-utilized due to limited electrolyte infiltration resulting in low specific capacitance with an increase in the film thickness. In SGM-28, the MnO_2 layer is comparatively thinner than the other devices; the material utilization by the electrolyte is thus higher in SGM-28 compared to the ones deposited at the higher time scales.

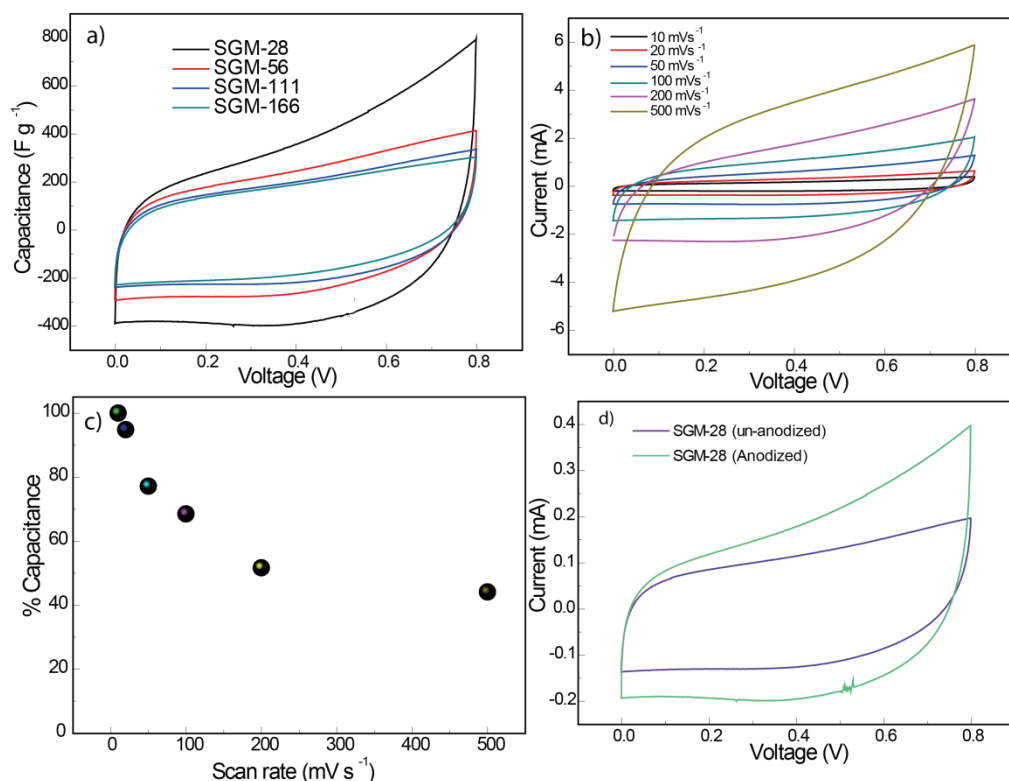


Figure 13. Electrochemical analysis of the different SGM devices: a) CV profiles of the various SGM devices recorded at a scan rate of 10 mV s^{-1} ; b) represents the CV profiles recorded at the scan rates of 10, 20, 50, 100, 200 and 500 mV s^{-1} ; c) a plot depicting the change in capacitance retention with increasing scan rates. d) CV profiles of SGM-28 recorded at 5 mV s^{-1} for the non-anodized and anodized SG depicting the increase in the capacitance for the anodized SG.

Figure 13b shows the CV profiles of the SGM-28-based device recorded at different scan rates. Even at a high scan rate of 500 mV s^{-1} , the device exhibits high rate capability, as is shown by the rectangular nature of the CV profile. Moreover, a significant amount of capacitance, 44% of the initial capacitance, is retained at 500 mV s^{-1} (Figure 13c). The beneficial effect of the anodization of the Grafoil on capacitance can be observed from the CV of the MnO_2 deposited SGM before and after the anodization process, shown in Figure 13d. The device fabricated from the anodized Grafoil as the substrate (SGM-28) exhibits 1.7 times higher capacitance compared to its non-anodized Grafoil counterpart. As discussed in the previous section, the anodization causes ripping of the graphite layers into separated porous sheets, which provide a high surface area for the MnO_2 deposition, while in the non-anodized Grafoil the same amount of MnO_2 is concentrated on less area, resulting in a thick MnO_2 film.

5.3.3.2 Electrochemical Impedance Spectroscopy

One of the major drawbacks of MnO_2 is its low conductivity, which is reflected in the equivalent series resistance (ESR). High ESR adversely affects the power rate and energy density of the supercapacitor. Importantly, in the context of the solid supercapacitors, the low sheet resistance is essential for good power rate. The sheet resistance measured for the SGM-28 electrode is $7.50 \Omega \square^{-1}$, calculated through the four-probe method. This value, compared to the pristine Grafoil, is high owing to the generation of defects and porosity. Electrochemical impedance spectroscopy (EIS) was performed to assess the internal electronics and structural characteristics of the electrode. The Nyquist plot in Figure 14 compares the impedance of the devices with various deposition times; ESR is lowest for the SGM-28 case but increases subsequently with the deposition time. The porous nature of the nano-grass MnO_2 helps in easy mass transfer inside the fibrous network, which is reflected in the low equivalent series resistance value of 7Ω for SGM-28. This value is quite less for the MnO_2 -based solid device compared to many of the literature reports.¹⁶ The Nyquist spectrum in the inset of Figure 14 does not show any appreciable semi-circle or charge transfer resistance, implying the fast redox kinetics in the MnO_2 phase. For the higher deposition times, the thickness of the MnO_2 film increases and accordingly results in dense and less porous films. The decline in the

porosity impedes the mass transfer to the interior of the active material, leading to the high ESR for high mass loading cases. The ESR measured here is better than the cases where the conducting polymer wrapping is used to facilitate charge transfer.¹⁷

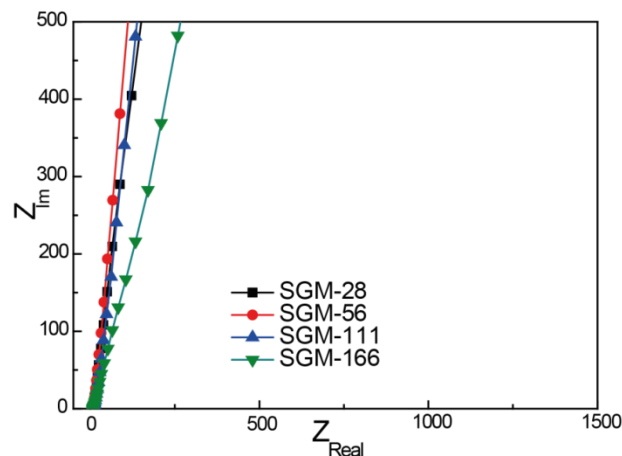


Figure 14. Nyquist plots obtained for the devices at different MnO_2 deposition times.

5.3.3.3 Galvanostatic Charge-Discharge

The performance of the symmetrical supercapacitor is evaluated by the GCD method. [Figure 15a](#) shows the charge-discharge curves for the devices based on the electrodes fabricated at different deposition times recorded at a current density of 0.5 A g^{-1} . These curves are typical for the MnO_2 symmetrical supercapacitor. With the increase in the MnO_2 loading, the area under the curve is decreasing continuously, which again suggests the limited capacitance value offered by the thick MnO_2 films. The electrode capacitance measured at 0.5 A g^{-1} for the SGM-28 system is 776 F g^{-1} , which decreases subsequently to 446, 402 and 332 F g^{-1} for the SGM-56-, SGM-111- and SGM-166-based systems, respectively. The areal and volumetric capacitances are the two important governing parameters from the practical point of view. The system based on SGM-28 along with its high specific capacitance exhibits an areal capacitance of 39 mF cm^{-2} and a volumetric capacitance of 2 F cm^{-3} . The volumetric capacitance measured here is better compared to that of the $\text{ZnO@MnO}_2\text{-RGO}$ and ZnO@C@MnO_2 supercapacitors¹⁸ reported in the literature. [Figure 15b](#) shows the discharge curves at current densities of 0.5, 1.0, 2.0, 3.0 and 4 A g^{-1} , where the curves are symmetrical and linear in nature, indicating good capacitive behaviour. Volumetric energy density measured for the SGM-28 device at a power density of 1.0 W cm^{-3} is 0.17 mWh cm^{-3} , which is many times higher compared to the carbon- MnO_2 ¹⁹ and ZnO-MnO_2 core-shell structures.¹⁸

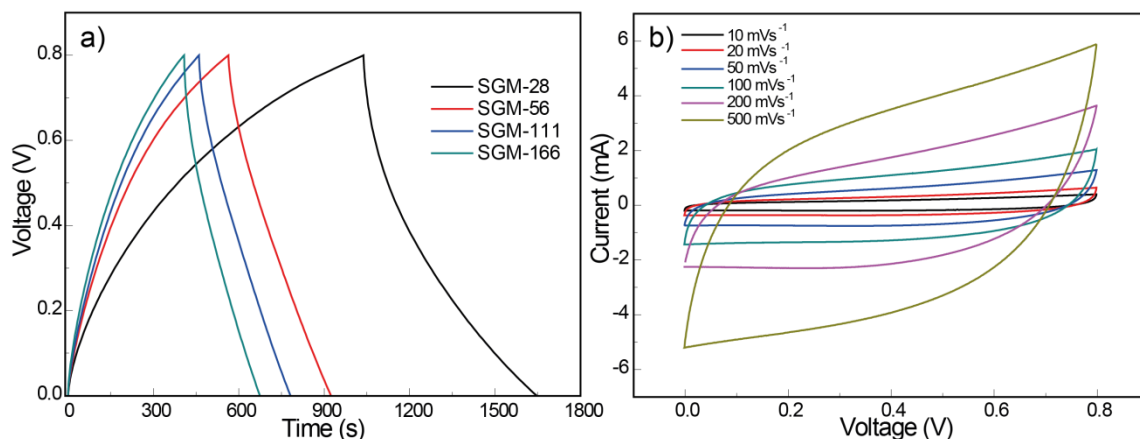


Figure 15. a) Charge-discharge (CD) curves recorded at a current density of 0.5 A g^{-1} ; b) CD curves recorded at different current densities for the SGM-28 device.

5.3.3.4 Durability Test

A durability test was performed under a constant current of 4.0 A g^{-1} at an operating voltage window of 0.8 V . [Figure 16a](#) displays cycling of the SGM-28 system carried out for 20,000 cycles where 91% of the initial capacitance is found to be retained after the Galvanostatic cycling. This excellent durability of the SGM-28 based device can be attributed to the close integration between the MnO_2 -nanograss and neutral PVA-LiCl gel electrolyte. This combination prevents the dissolution of MnO_2 owing to the limited amount of water present in the system, while mechanically stabilizing the electrode by preserving its structure.²⁰ FESEM images of the surface of SGM-28 taken subsequent to the cycling for 20,000 cycles are shown in [Figure 17](#). It can be seen that the PVA-LiCl gel uniformly covers the MnO_2 surface and the nano-grass morphology remains intact after the cycling. This morphology preservation during the charge-discharge cycling results in high durability (strong adherence of MnO_2 on the substrate). To validate the flexibility aspects of the device, the cycling was also carried out under bending and twisting conditions, as shown in [Figure 16b](#). In the bending condition, it retains 99% of its initial capacitance and the value remains constant without any fading. Similarly, in the twisting conditions, 98% of the initial capacitance is preserved with no apparent loss. This excellent flexibility is ascribed to the strong integration of the substrate and MnO_2 packed together by the gel electrolyte.

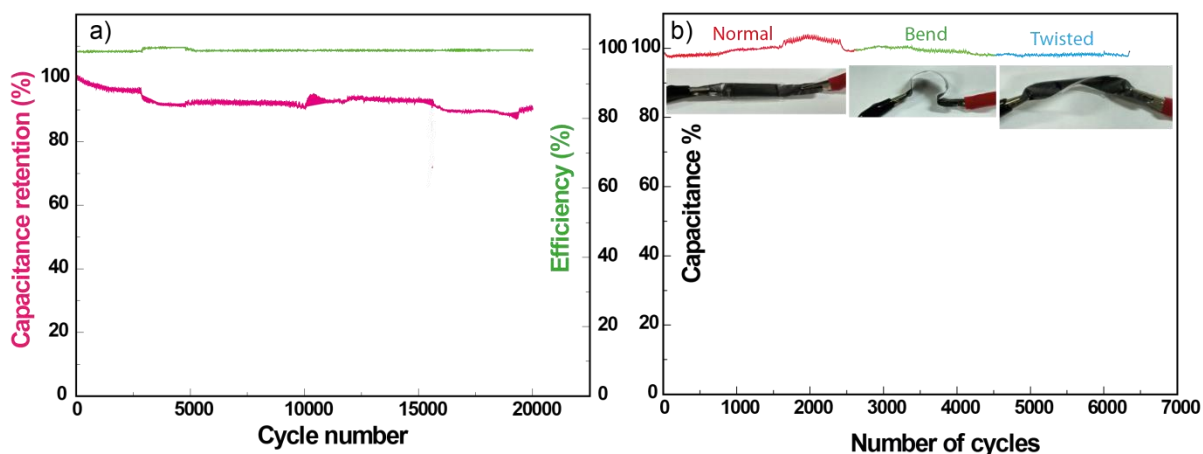


Figure 16. a) Representation of the cycling and coulombic efficiency for the SGM-28-based system subjected to 20,000 Galvanostatic cycles at a current density of 4 A g^{-1} ; b) representation of the cycling stability under the bending and twisting conditions of the device.

5.4 Conclusion

In summary, the current work showcases the preparation of a novel, flexible, highly conducting and low-cost substrate derived from Grafoil by Scotch tape method and its application for the electrodeposition of MnO_2 nano-grass for devising high performance solid-state supercapacitors. The device delivered a high power density of 1 W cm^{-3} and durability with 91% retention after 20,000 cycles. The as-formed Grafoil layer-adhered Scotch tape substrate is non-porous and flat, which is further modified through electrochemical anodization for increasing the surface area, porosity and hydrophilicity while maintaining a sufficient conductivity of 20 S cm^{-1} . The nano-grass morphology of MnO_2 is adequately porous, which allows the facile movement of the electrolyte ions, resulting in low ESR of 7Ω and high rate capability. A thin film of MnO_2 deposited over SGM exhibits a high specific capacitance of 776 F g^{-1} at 0.5 A g^{-1} current density along with high volumetric capacitance of 2.0 F cm^{-3} . The demonstrated flexible substrate is very cheap and highly flexible with excellent mechanical durability, which holds great promise for fabrication of flexible supercapacitors and other flexible energy storage devices.

5.5 References

1. L. Li, Z. A. Hu, N. An, Y. Y. Yang, Z. M. Li and H. Y. Wu, *The Journal of Physical Chemistry C*, 2014, **118**, 22865-22872.
2. M. Toupin, T. Brousse and D. Bélanger, *Chemistry of Materials*, 2004, **16**, 3184-3190.
3. P. Simon, Y. Gogotsi and B. Dunn, *Science*, 2014, **343**, 1210-1211.
4. C. Meng, C. Liu, L. Chen, C. Hu and S. Fan, *Nano Letters*, 2010, **10**, 4025-4031.
5. K. Zhang, H. Hu, W. Yao and C. Ye, *Journal of Materials Chemistry A*, 2015, **3**, 617-623.

6. X. Li, G. Wang, X. Wang, X. Li and J. Ji, *Journal of Materials Chemistry A*, 2013, **1**, 10103-10106.
7. Z. S. Wu, Z. Liu, K. Parvez, X. Feng and K. Müllen, *Advanced Materials*, 2015, **27**, 3669-3675.
8. R. Soni, B. Anothumakkool and S. Kurungot, *ChemElectroChem*, 2016, **3**, 1329-1336.
9. L. Peng, X. Peng, B. Liu, C. Wu, Y. Xie and G. Yu, *Nano Letters*, 2013, **13**, 2151-2157.
10. M. Acerce, D. Voiry and M. Chhowalla, *Nature Nanotechnology*, 2015, **10**, 313.
11. K. Parvez, Z.-S. Wu, R. Li, X. Liu, R. Graf, X. Feng and K. Müllen, *Journal of the American Chemical Society*, 2014, **136**, 6083-6091.
12. H. Kim, J. Hong, G. Yoon, H. Kim, K.-Y. Park, M.-S. Park, W.-S. Yoon and K. Kang, *Energy & Environmental Science*, 2015, **8**, 2963-2969.
13. G.-R. Li, Z.-P. Feng, Y.-N. Ou, D. Wu, R. Fu and Y.-X. Tong, *Langmuir*, 2010, **26**, 2209-2213.
14. X. Lu, M. Yu, G. Wang, T. Zhai, S. Xie, Y. Ling, Y. Tong and Y. Li, *Advanced Materials*, 2013, **25**, 267-272.
15. L. Y. a. H. S. Chuanyun Wan, *Int. J. Electrochem. Sci.*, 2014, **9**, 4024 - 4038.
16. G. Yu, L. Hu, M. Vosgueritchian, H. Wang, X. Xie, J. R. McDonough, X. Cui, Y. Cui and Z. Bao, *Nano Letters*, 2011, **11**, 2905-2911.
17. G. Yu, L. Hu, N. Liu, H. Wang, M. Vosgueritchian, Y. Yang, Y. Cui and Z. Bao, *Nano Letters*, 2011, **11**, 4438-4442.
18. P. Yang, X. Xiao, Y. Li, Y. Ding, P. Qiang, X. Tan, W. Mai, Z. Lin, W. Wu, T. Li, H. Jin, P. Liu, J. Zhou, C. P. Wong and Z. L. Wang, *ACS Nano*, 2013, **7**, 2617-2626.
19. X. Xiao, T. Li, P. Yang, Y. Gao, H. Jin, W. Ni, W. Zhan, X. Zhang, Y. Cao, J. Zhong, L. Gong, W.-C. Yen, W. Mai, J. Chen, K. Huo, Y.-L. Chueh, Z. L. Wang and J. Zhou, *ACS Nano*, 2012, **6**, 9200-9206.
20. G. Wang, X. Lu, Y. Ling, T. Zhai, H. Wang, Y. Tong and Y. Li, *ACS Nano*, 2012, **6**, 10296-10302.

Chapter-6

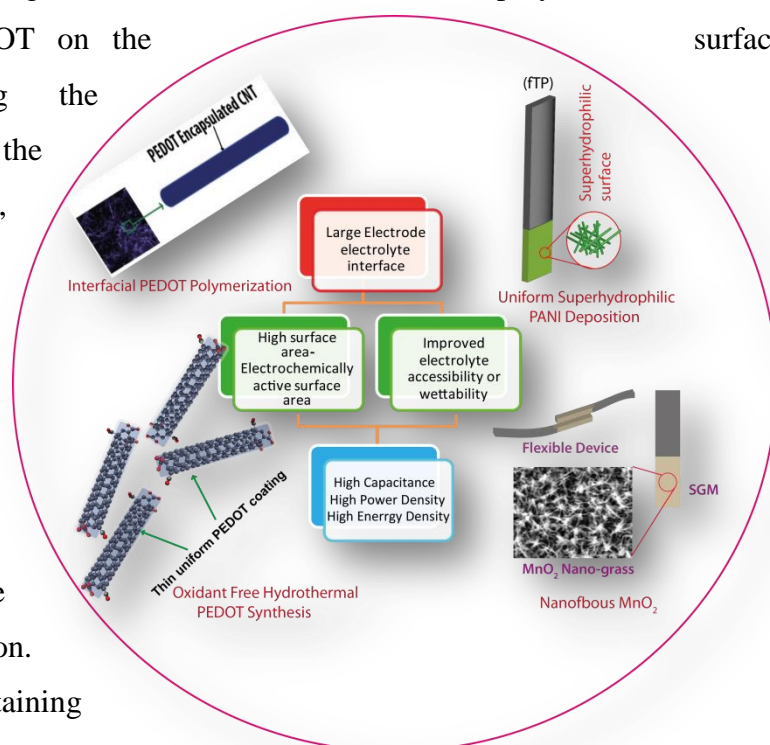
Summary

This chapter sums-up the main achievements and outcomes of the four working chapters compiled in this treatise. The primary target of the work presented here is to develop strategies and synthesis protocol to realize the full potential of pseudocapacitive materials in the solid and flexible supercapacitors in a cost-effective manner. To actualize this, a strategy of structural alignment or structurally directed growth of pseudocapacitive materials on the surface of carbon morphologies which act as scaffolds and current collectors is tested successfully. This dissertation begins with induction of interfacial polymerization which confines the growth of PEDOT on the surface

of CNTs. By restricting the polymerization at the aqueous/organic interface, PEDOT grows to form a continuous, coherent coating on the CNTs. In the next strategy, the PEDOT layer formed on the CNTs in the previous chapter was further thinned down by removing the oxidizing agent for polymerization.

In this chapter, the oxygen-containing functional groups on the surface of CNTs

were exploited for the EDOT polymerization in a hydrothermal reaction. This strategy allows formation of ultrathin PEDOT coating on CNTs and improves electrolyte ion movement at the interface. In the third chapter, effect of structural alignment and the manipulation of wettability of the scaffold on the capacitive properties of PANI are analyzed. It was found that, favourable wettability of the scaffold plays a profound role in engineering the properties of the active material along with other parameters to obtain high-performance in solid supercapacitors. In the last working chapter, this systematic plan was applied to manganese oxide, a pseudocapacitive material. Also, a highly flexible, cost-effective, and conducting scaffold is introduced, and modification of surface properties of



scaffold on the properties of MnO_2 is tested. Lastly, this chapter concluded with the discussion of future scope, prospects, and importance of this thesis in the development of solid supercapacitors.

6.1 1D alignment of PEDOT on CNTs through interfacial polymerization towards High Conductivity and Low Equivalent Series Resistance

To achieve optimum performance in the solid supercapacitors and to compete with the aqueous counterparts, it is necessary to achieve high areal and volumetric capacitances together with low ESR. PEDOT is an interesting pseudocapacitive material that has high conductivity and high stability. However, grain boundary concentration and its less impregnation by electrolyte in solid devices have so far impeded its widespread application in solid supercapacitors. In this chapter (chapter-2), to address these issues, a coherent uniform layer of PEDOT was synthesized by restricting the growth of PEDOT on the surface of CNTs in surface confined interface of aqueous/organic medium containing the oxidizing agent and monomer, respectively. Interfacial polymerization ensured the surface-aligned growth of PEDOT along the surface of the CNTs in the buckypaper (BP). The hydrophilic interaction between the carboxyl groups on the surface of CNTs and the oxidizing agent, iron perchlorate, helped the system to establish a uniform and aggregate-free growth pattern of PEDOT. This controlled growth of the polymer phase and effective intercalation of the gel electrolyte helped to realize a flexible electrode with low sheet resistance and charge-transfer resistance. Careful optimization of the composition of PEDOT in the paper provided an electrode with an ultralow sheet resistance of $3.4 \Omega \square^{-1}$ and an ESR of 0.95Ω ; these are among the lowest values of ESR achieved for the PEDOT-based solid supercapacitors. Highly flexible and conducting free-standing electrodes are prepared by simple dispersion and filtration method. A thin and flexible solid-state supercapacitor was developed by using a hybrid electrode derived from MWCNT-based BP and PEDOT and creating an electrode/electrolyte interface by infiltration of the PVA-LiCl gel electrolyte. The device has a thickness of 210 μm , and it is also very lightweight which has the advantage of occupying less space. It has prospective applications in electric vehicles and flexible electronics where the weight of the components affects the efficiency of cars and gadgets. The solid prototype device is highly flexible with good retention of the capacitive characteristics in the bent and normal states. The device delivered a volumetric capacitance of 18 F cm^{-3} and an areal capacitance of 354 mF cm^{-2} , which are the highest in its class. This laboratory scale process

demonstrated in this chapter can be easily scaled to industrial level as BP is commercially available and PEDOT coating can be conveniently applied by roll-coating method demonstrated here, to prepare large-area PEDOT-modified BP in a short span of time.

6.2 Oxidant Free Hydrothermal Synthesis of Ultrathin PEDOT over CNTs and Introduction of Xanthan Gum-based Shear Thinning Gel electrolyte

The previous chapter (Chapter-2) explained how interface confined polymerization can result into undifferentiated PEDOT coating on the CNT surface. The present chapter (Chapter-3) deals with a strategy wherein the PEDOT coating is further thinned down by relinquishing the use of an oxidizing agent. Instead, oxygen-containing surface functional groups incorporated through acid functionalization cause the oxidation of EDOT monomer which subsequently forms PEDOT on the surface of CNTs in a seamless aligned manner which has remained elusive. This arrangement provides high ESA and unrestricted movement of ions in the solid supercapacitor prototype. Formation of PEDOT is confirmed through running control experiments, IR spectroscopy, XRD, and XPS. Effect of the amount of PEDOT in the composite was also tested, and it was found that the 1:2 CNT:EDOT weight ratio was optimum to obtain the maximum performance. The capacitance measured for the 1:2 composite is the highest at 336 mF cm^{-2} whereas the 1:1 and 1:4 composites show 278 and 268 mF cm^{-2} , respectively, in solid-state supercapacitor device. The high capacitance is attributed to the thin coherent PEDOT coating that possesses high ESA and low density of the grain boundaries. Also, a new shear thinning gel electrolyte, Xanthan gum- H_2SO_4 (XG- H_2SO_4), was introduced in this work as a replacement for the conventional PVA-based electrolyte as it failed to infiltrate deeper into the composite electrode. XG- H_2SO_4 gel due to its shear-thinning properties can impregnate with the CNT-PEDOT composite. The performance of the XG- H_2SO_4 electrolyte is compared with the widely used PVA- H_2SO_4 gel electrolyte and the former has emerged as a clear winner with an ESR of 0.31Ω and 70 % capacitance retention at a scan rate of 1000 V s^{-1} ; the corresponding values for PVA- H_2SO_4 gel electrolyte are 1.43Ω and 50 %, respectively. Moreover, the devices prepared with XG- H_2SO_4 show better frequency behaviour than its counterpart. The areal capacitance is as high as 336 mF cm^{-2} and the volumetric capacitance of the device is 8.5 F cm^{-3} . The real accomplishment of this work lies in the maximum power density which is 74 W cm^{-3} and is the highest among the PEDOT-based solid supercapacitors. Moreover, the volumetric energy density obtained for the device is 1.7 mWh cm^{-3} , which is also the highest in its class. The

method developed here is also highly scalable. Large quantities of the composite can be prepared through the hydrothermal method. Standalone flexible electrode developed here does not require current collector which makes it cost-effective, and the process also reduces dead volume, further adding to the efficiency of the process. This electrode also has prospective applications in flexible electronics and electric vehicles where high power and high energy density are necessary. The novel shear-thinning gel induced in this chapter can be used in other supercapacitor electrodes as well.

6.3 Enhancing the Electrochemical Surface Area through Induction of Superhydrophilicity and Structural Alignment in Polyaniline to Achieve High Capacitance

Polyaniline has high theoretical capacitance; however, practical realization of this has long eluded the researchers due to low ESA of PANI. Also, achieving high rate capability and power density in PANI is a pre-requisite for its application in commercial devices. The reasons identified for the low rate capability are the high resistance of PANI films and slow ion movement of the electrolyte. To achieve high capacitance and power capability in PANI, structural alignment in conjunction with wettability manipulation are introduced and these results are summarized in Chapter-4. This chapter highlights a novel approach of manipulating the wettability of PANI to make it superhydrophilic toward addressing the low practical capacitance and reduced performance of PANI in a solid supercapacitor. The strategy demonstrated transforms a hydrophobic surface to a superhydrophilic surface, which is used to realize the near theoretical capacitance and high rate capability in a PANI-based supercapacitor. Carbon fiber paper is used as a scaffold for PANI deposition. It is electrochemically functionalized to transform its surface into a superhydrophilic surface. This superhydrophilic surface possesses high ESA of 15.71 cm^2 per geometric surface area compared to 1.77 cm^2 for pT. PANI polymerized on this superhydrophilic surface also shows superhydrophilic behaviour due to electronic interactions of the underlying scaffold and PANI. The electrochemical functionalization employed to enhance the ESA of the conducting substrate further leads to increased ESA of PANI. Moreover, improved wettability assists in better impregnation of the gel electrolyte which ultimately results in a large electrode-electrolyte interface. All these corroborate to achieve a capacitance of 1700 F g^{-1} in the single cell and a specific capacitance of 1335 F g^{-1} and an areal capacitance of 1.3 F cm^{-2} in the solid-state device at a current density of 10 A g^{-1} . An ultralow ESR value of 0.3Ω , which is invoked by the low sheet resistance ($226 \text{ m}\Omega \square^{-1}$) and free electrolyte ion movement, causes

high rate capability with 90 % retention of the initial capacitance at a current density of 50 A g⁻¹. An energy density of 30 Wh kg⁻¹ obtained for the device is comparable to a lead-acid battery and Panasonic LC-R1233P cell. Moreover, the device shows stable performance up to 10,000 cycles with retention of 85 per cent at a current density of 50 A g⁻¹. Also, the demonstrated method can be successfully applied to other systems, such as PEDOT, polypyrrole, and metal oxides such as MnO₂ and so forth, to enhance the electrochemically active surface area and performance.

6.4 Organization of MnO₂ into Grass-like Nanofibril Structure on Electrochemically Modified Carbon Sheets

In MnO₂, thin films show high capacitance whereas relatively thicker films exhibit low capacitance. The inferior performance of the thick MnO₂ films is caused by the low diffusion coefficient of H⁺ ion and alkali metal ions which are not able to diffuse inside the oxide crystals. Thus, only the surface of MnO₂ participates in the charge-storage. In Chapter-5, thin MnO₂ films are grown on an electrochemically modified substrate. A cost-effective highly flexible and conducting substrate is prepared by a stick and simple peel-off method using grafoil and scotch-tape. The surface of the scaffold is anodized to exfoliate the carbon sheets to produce *in-situ* formed graphene like-sheets. The as-formed Grafoil layer-adhered Scotch tape substrate is non-porous and flat, which is further modified through electrochemical anodization for increasing the surface area, porosity and hydrophilicity while maintaining a sufficient conductivity of 20 S cm⁻¹. MnO₂ is electrodeposited in the electrochemically modified surface through a constant current method and this forms ultrathin nanofibers which are arranged in a grass-like fashion. The effect of MnO₂ thickness on capacitance and morphology evolution with electrodeposition time is studied in detail. MnO₂ deposited for longer times shows low capacitance as the fibers become thicker. Also, the effect of deposition current density is also studied in which 4 mA cm⁻² current density was found to be appropriate to get maximum performance from MnO₂. A thin film of MnO₂ deposited over scotch-tape derived substrate (SGM) exhibits a high specific capacitance of 776 F g⁻¹ at a current density of 0.5 A g⁻¹ along with high volumetric capacitance of 2.0 F cm⁻³. The device delivered a high power density of 1 W cm⁻³ and durability with 91% retention after 20,000 cycles. The nano-grass morphology of MnO₂ is adequately porous, which allows the easy movement of the electrolyte ions, resulting in low ESR of 7 Ω and high rate capability. The demonstrated flexible substrate is cost-effective and highly flexible with excellent mechanical

durability and conductivity, which holds great promise for fabrication of flexible supercapacitors and other flexible energy storage devices.

6.5 Future Scope and Prospects

The ideas and strategies demonstrated in this dissertation have far-reaching utility in charge-storage and other electrochemical fields. The performance of any electrochemical system largely depends on the efficiency of the electrode-electrolyte interface, ion accessibility to the interface, the resistance of the system, etc. In this work, a holistic approach is taken where strategies are designed not just to address one issue but a wholesome of problems afflicting pseudocapacitive charge storage. The approach to increasing the performance of PEDOT, PANI and MnO_2 through the directed growth of thin films and fibers can be efficiently applied to all other pseudocapacitive materials like polypyrrole, polythiophene, iron oxides, vanadium oxides, etc. Shear thinning gel electrolyte introduced in the third chapter shows high infiltration and high rate capability compared to the conventional gel electrolytes. The concept of shear thinning electrolytes has application in solid supercapacitor devices where the conventional gel electrolytes show inferior performance regarding high ESR and low rate capability due to reduced infiltration. These gel electrolytes also have promising applications in other flexible and solid device like dye-sensitized solar cells and batteries. Flexible substrate derived from scotch-tape that is introduced in Chapter 5, has the good prospect of replacing other scaffolds used for active material deposition in supercapacitors. It can replace carbon cloths, gold coated PET and other expensive materials.

Electrocatalysis is another field which can capitalize on the ideas and concepts demonstrated in this work. In electrocatalysis, the number of active sites and conductivity play primary role in dictating its efficiency towards a particular electrochemical reaction. Conducting polymers like PEDOT, PANI and metal oxides like MnO_2 , NiO, RuO_2 , etc. are used for various electrocatalytic reactions like oxygen reduction, oxygen evolution, methanol oxidation, and many other reactions. The oxides are semiconducting; they are mixed with carbon materials like CNTs, CNF, graphene, carbon black, etc. to improve charge conduction and mass transfer. Therefore, the strategies dictated in this treatise can be suitably applied to the synthesis of composite materials for electrocatalysis. The materials derived from the concept developed here are expected to possess a large number of active sites with better current collection, charge transfer and mass-transfer.

List of Publications

Journal Articles

1. M. Ghosh, V. Vijayakumar, **R. Soni**, S. Kurungot, Rationally designed self-standing V₂O₅ electrode for high voltage non-aqueous all-solid-state symmetric (2.0 V) and asymmetric (2.8 V) supercapacitors, *Nanoscale*, **2018**, 10, 8741–8751
2. S. Sharma, **R. Soni**, K. Sreekumar, S. K. Asha, Naphthalenediimide Copolymers by Direct Arylation Polycondensation as Highly Stable Supercapacitor Electrode Materials, *Macromolecules*, **2018**, 51 (3), 954–965.
3. **R. Soni**, V. Kashyap, D. Nagaraju, S. Kurungot, Realizing High Capacitance and Rate Capability in Polyaniline by Enhancing the Electrochemical Surface Area through Induction of Superhydrophilicity, *ACS Applied Materials & Interfaces* **2018** 10 (1), 676-686.
4. S. K. Singh, V. Kashyap, N. Manna, S. N. Bhange, **R. Soni**, R. Boukherroub, S. Szunerits, Efficient and Durable Oxygen Reduction Electrocatalyst Based on CoMn Alloy Oxide Nanoparticles Supported Over N-Doped Porous Graphene, *ACS Catalysis*, **2017**, 7 (10), 6700-6710.
5. **R. Soni**, A. Raveendran, S. Kurungot, Grafoil–Scotch Tape-Derived Highly Conducting Flexible Substrate and its Application as a Supercapacitor Electrode, *Nanoscale*, **2017**, 9 (10), 3593-3600.
6. **R. Soni**, B. Anothumakkool, K. Sreekumar, 1D Alignment of PEDOT in a Bucky paper for High-Performance Solid Supercapacitors *ChemElectroChem*, **2016**, 3, 1329 – 1336.
7. B. Anothumakkool, I. Agrawal, S. N. Bhange, **R. Soni**, O. Game, S. B. Ogale, K. Sreekumar, Pt- and TCO-Free Flexible Cathode for DSSC from Highly Conducting and Flexible PEDOT Paper Prepared via in situ Interfacial Polymerization, *ACS Applied Materials & Interfaces*, **2016**, 8 (1), 553-562.
8. B. Anothumakkool, **R. Soni**, S. N. Bhange, S. Kurungot, Novel Scalable Synthesis of Highly Conducting and Robust PEDOT Paper for a High Performance Flexible Solid Supercapacitor, *Energy Environ. Sci.*, **2015**, 8 (4), 1339-1347.
9. **R. Soni**, V. Vijayakumar, S. Kurungot, Synthesis of Carbon Nanosheets and Nitrogen-doped Carbon Nanosheets from Perylene Derivatives for Application in Electrochemical Capacitors, **Communicated**.

10. **R. Soni**, S.N. Bhange, E. Athira, R. Chetry and K. Sreekumar, Oxidant-free Hydrothermal Synthesis of PEDOT-CNT Composite for High-performance Supercapacitors, Under preparation.
11. **R. Soni**, S. N. Bhange and K. Sreekumar, Pt-Free Electrocatalyst Derived from Waste Leather for Alkaline Exchange Membrane Fuel Cells and Zinc-Air Batteries, Under preparation.
12. **R. Soni** and K. Sreekumar, Fe₂P₄O₁₂ as a Highly Stable Electrode Material for Electrochemical Capacitors, Under preparation.
13. **R. Soni**, M. Ghosh and K. Sreekumar, V₂O₅ as an Electrode Material for High Power Density Lithium Ion Capacitors, Under preparation.
14. S.K. Sharma, **R. Soni**, K. Sreekumar and S.K. Asha, Naphthalene Diimide and Perylene Diimide Based Alternate and Random Copolymers for Supercapacitor Electrode Materials, Under Preparation.

Patents Filed

1. Roby Soni, Bihag Anothumakkool and Dr. Sreekumar Kurungot, A PEDOT Coated Flexible CNT Framework (Buckupaper) by Interfacial Polymerization for a Thin Flexible Solid Supercapacitor, Invention Disclosure Number: **2016-INV-0024**
2. Dr. Asha Syamakumari, Sandeep Kumar Sharma, Roby Soni and Dr. Sreekumar Kurungot, Naphthalenediimide Copolymers by Direct Arylation Polycondensation as Highly Stable Supercapacitor Electrode Materials. Invention Disclosure Number: **2017-INV-0082**

Erratum

